Recognition and Suppression of Interference Between SPAD-Based Direct Time-of-Flight Systems

Von der Fakultät für Ingenieurwissenschaften,
Abteilung Elektrotechnik und Informationstechnik
der Universität Duisburg-Essen

zur Erlangung des akademischen Grades

Doktor der Ingenieurwissenschaften

genehmigte Dissertation

von
Sara Grollius
aus
Hachenburg

Datum der Einreichung: 29.08.2022

Gutachter: Prof. Dr. Anton Grabmaier
Gutachter: Prof. Dr. Thomas Kaiser

Tag der mündlichen Prüfung: 28.04.2023

Abstract

3D imaging of the environment is required for many applications such as autonomous driving. One method for distance determination recently attracting attention is light detection and ranging (LiDAR). A LiDAR system measures the time that is required by emitted light to travel to an object and back to the detector. This time-of-flight (TOF) is equivalent to the object distance using the speed of light. Imagining a world full of LiDAR systems, there might be many light signals emitted from different systems so that each system might observe multiple signals at once. In the worst case, the interference between multiple LiDAR systems can lead to wrong distance measurements resulting in traffic accidents which makes prevention of mutual LiDAR interference necessary.

In this work, the interference between direct time-of-flight (dTOF) LiDAR systems based on single-photon avalanche diodes (SPADs) is analyzed. At first, the spatial and temporal conditions are investigated, under which interference occurs at all. It is shown that the probability of occurrence is not negligible. For the analysis of occurring interference in LiDAR measurements, a test system is developed, which can be placed in front of a LiDAR system to produce adjustable interference signals. The impacts of interference on the LiDAR measurement and the resulting distance determination are evaluated. For LiDAR systems operating slightly asynchronously, the interfering signal might not disturb the distance determination. For synchronous systems, the interfering signal might even suppress the detection of the self-emitted light so that the distance determination becomes impossible. To avoid wrong distance measurements, methods for the recognition and suppression of interference are developed so that the reliability of LiDAR systems can be increased and the safety of applications like autonomous driving can be guaranteed.

Zusammenfassung

Die 3D-Bilderfassung der Umgebung ist für viele Anwendungen wie das autonome Fahren erforderlich. Eine Methode zur Entfernungsbestimmung, die in letzter Zeit viel Aufmerksamkeit erregt hat, ist *light detection and ranging* (LiDAR). Ein LiDAR-System misst die Zeit, die das ausgesendete Licht benötigt, um zu einem Objekt und zurück zum Detektor zu gelangen. Diese Signallaufzeit ist äquivalent zur Objektdistanz unter Verwendung der Lichtgeschwindigkeit. Stellt man sich eine Welt voller LiDAR-Systeme vor, könnte es viele Lichtsignale geben, die von verschiedenen Systemen ausgesendet werden, sodass jedes System mehrere Signale gleichzeitig beobachten könnte. Im schlimmsten Fall können die Störungen zwischen mehreren LiDAR-Systemen zu falschen Distanzmessungen und damit Verkehrsunfällen führen, weshalb eine Abwehr gegenseitiger LiDAR-Störungen erforderlich ist.

In dieser Arbeit wird die Störung zwischen *direct time-of-flight* (dTOF) LiDAR-Systemen basierend auf *single-photon avalanche diodes* (SPADs) analysiert. Zunächst werden die räumlichen und zeitlichen Bedingungen untersucht, unter denen Störungen überhaupt auftreten. Es wird gezeigt, dass die Auftretenswahrscheinlichkeit nicht vernachlässigbar ist. Zur Analyse auftretender Störungen in LiDAR-Messungen wird ein Testsystem entwickelt, das vor ein LiDAR-System gestellt werden kann, um einstellbare Störsignale zu erzeugen. Die Auswirkungen der Störungen auf die LiDAR-Messung und die daraus resultierende Distanzbestimmung werden bewertet. Bei LiDAR-Systemen, die leicht asynchron laufen, beeinflusst das Störsignal die Distanzbestimmung nicht zwangsläufig. Bei synchronen Systemen hingegen kann das Störsignal sogar die Detektion des selbst emittierten Lichts unterdrücken, sodass eine Distanzbestimmung unmöglich wird. Um falsche Distanzmessungen zu vermeiden, werden Methoden zur Erkennung und Unterdrückung von Störungen entwickelt, sodass die Zuverlässigkeit von LiDAR-Systemen erhöht und die Sicherheit von Anwendungen wie dem autonomen Fahren gewährleistet werden kann.

Contents

Glossaries

Abbreviations

ADAS	advanced driver assistance systems
AMCW	amplitude-modulated continuous-wave
APD	avalanche photodiode
CDMA	code-division multiple access
CoC	circle of confusion
CW	continuous-wave
DCR	dark count rate
DOF	depth of field
dTOF	direct time-of-flight
DUT	device-under-test
EOL	end-of-line
FDMA	frequency-division multiple access
FFT	fast Fourier transform
FMCW	frequency-modulated continuous-wave
FMEDA	failure modes effects and diagnostic analysis
FOI	field-of-illumination
FOV	field-of-view
FPGA	field programmable gate array
Fraunhofer IMS	Fraunhofer Institute for Microelectronic Circuits and Systems IMS
FTA	fault tree analysis
FWHM	full width at half maximum
HiL	hardware-in-the-loop
iTOF	indirect time-of-flight

LiDAR	light detection and ranging
LTS	LiDAR target simulator
MEMS	micro-electro-mechanical system
MiL	model-in-the-loop
ND	neutral density
OPA	optical phased array
OTA	over-the-air
PD	photodiode
PDE	photon detection efficiency
PDF	probability density function
PDP	photon detection probability
PiL	processor-in-the-loop
PMT	photomultiplier tube
PPM	pulse-position modulation
PRF	pulse repetition frequency
radar	radio detection and ranging
RMS	root mean square
SDMA	space-division multiple access
SiL	software-in-the-loop
SLAM	simultaneous localization and mapping
SNR	signal-to-noise ratio
SPAD	single-photon avalanche diode
TCSPC	time-correlated single photon counting
TDMA	time-division multiple access
TOF	time-of-flight
WDMA	wavelength-division multiple access

Symbols

Symbol	Unit	Description
$A_{\mathrm{LTS,px}}$	m^2	LTS pixel area
A_{px}	m^2	LiDAR pixel area
A_{src}	m^2	LTS source area
D	mm	LiDAR aperture diameter
T_{ND}	%	neutral density (ND) filter transmission
Φ_{L}	W	optical laser peak power
Φ_{src}	°	optical power of LTS source
η_{FF}	%	fill factor
η_{PDP}	%	photon detection probability (PDP)
λ	nm	laser wavelength
ρ	%	target reflectance
$\theta_{\mathrm{FOV,H}}$	°	horizontal FOV
$\theta_{\mathrm{FOV,V}}$	°	vertical FOV
$\theta_{\mathrm{L,H}}$	°	horizontal FOI
$\theta_{\mathrm{L,V}}$	°	vertical FOI
θ_{px}	°	LiDAR pixel FOV
$a_{\mathrm{LTS,px}}$	m	LTS pixel size
a_{px}	m	LiDAR pixel size
d_{ext}	m	extinction distance
d_{max}	m	range of LiDAR system (maximum target distance)
d	m	target distance
f_{p}	Hz	pulse repetition frequency (PRF)
f	mm	focal length
k_{SN}	−	signal-to-noise ratio (SNR)
n_{meas}	−	number of measurements per histogram
r_{B}	Hz	background-generated event rate
r_{DCR}	Hz	dark count rate (DCR)
r_{L}	Hz	laser-generated event rate
s	m	LTS screen distance
t_{TOF}	m	time-of-flight (TOF)

Symbol	Unit	Description
t_{bin}	ps	bin width
t_{d}	ns	dead time
t_{hist}	µs	histogram length
t_{p}	s	laser pulse width

Physical Constants

Symbol	Unit	Value	Description
c	m/s	299 792 458	speed of light
h	$\mathrm{m^2kg/s}$	$6.626\,070\,15 \cdot 10^{-34}$	Planck constant

Chapter 1

Introduction

3D imaging of the environment is important for many applications like autonomous driving. For the measurement of distances, a method with increasing interest from industry and science is light detection and ranging (LiDAR). To determine a target distance, a LiDAR system emits light that is reflected by the target back to the system, where the reflected light is detected. The LiDAR system measures the time-of-flight (TOF) of this light, which can be transformed into the target distance using the speed of light. With the increasing use of LiDAR systems, the probability for multiple LiDAR systems at the same place increases, which can lead to LiDAR interference between these systems. Every LiDAR system emits light that can potentially be detected by other LiDAR systems as well and disturb the LiDAR measurement. In the worst case, interference can produce wrong distance measurements leading to possibly dangerous consequences especially with regards to autonomous driving.

This work focuses on direct time-of-flight (dTOF) LiDAR systems based on single-photon avalanche diodes (SPADs) as photodetectors. The aim of this work is to evaluate the conditions for the occurrence of LiDAR interference, investigate the impact and provide solutions for critical interference scenarios. To increase the reliability of LiDAR systems, methods for the recognition and suppression of interference in LiDAR measurements are provided. These topics are structured as follows.

Chapter two establishes the theoretical background. First, the working principle of LiDAR systems is introduced. For the analysis of LiDAR measurements, the expected photon detection rates obtained by the LiDAR detector from a specific target reflection are determined. With these rates, the LiDAR measurements con-

sisting of histograms are modeled and simulated. At the end, example applications are presented with regards to their interference probability.

Chapter three analyzes when interference occurs at all. For this purpose, the general definition of LiDAR interference is provided, where the conditions for interference with different levels of severity are presented. As one aspect for the occurrence of interference, the influence of the spatial arrangement of LiDAR systems is investigated. As a second aspect, it is discussed, how often interference occurs between multiple LiDAR systems in the same place.

In **chapter four**, a test system is developed, which can be placed in front of a LiDAR system to test it under laboratory conditions. For such a test system, the requirements are discussed. The adjustment of various testing scenarios with selectable target distance and target reflectance is described. In this work, a demonstrator is constructed and characterized, which can emulate LiDAR measurements affected by interference for the subsequent investigations.

Chapter five illustrates the impacts of interference on the measured LiDAR histograms. The resulting influence on the determination of the target distance is derived. The most dangerous case of unrecognizable interference is analyzed, where the interference signal suppresses the signal corresponding to the real target so that a wrong target distance might be determined.

In **chapter six**, a method for interference suppression is presented, which is suitable for the SPAD-based dTOF LiDAR systems considered in this work. For the proposed suppression method, an algorithm for the recognition of multiple interference signals is developed. The presented methods for recognition and suppression of interference are evaluated by simulated and measured LiDAR data.

Chapter seven provides the conclusion of the results and an outlook of this work.

Chapter 2

Light Detection and Ranging

In this chapter, the working principle and structure of LiDAR systems are introduced. For the analysis of LiDAR measurements, the expected photon detection rates from background and laser light at the LiDAR detector are derived for specific target properties. To determine the distance of a target, an example data processing is shown using the modeled photon detection rates and simulated LiDAR measurements in form of histograms.

2.1 Working Principle of LiDAR Systems

LiDAR is a method for distance determination by emitting light, which is reflected by a target back to the LiDAR system. There are different LiDAR methods to determine the target distances. In the following, the most common methods are described with focus on single-photon detectors because they are used in this work. As system components, possible photodetectors are presented and light source properties are discussed. Finally, the LiDAR system *Owl* from Fraunhofer Institute for Microelectronic Circuits and Systems IMS (Fraunhofer IMS) is presented, which is used for the LiDAR measurements in this work.

2.1.1 Overview of LiDAR Methods

There are different LiDAR methods to determine the target distance represented in Figure 2.1. TOF LiDAR methods operate in the time domain, whereas frequency-modulated continuous-wave (FMCW) LiDAR is based on the light frequency as reciprocal of the wavelength. TOF LiDAR can be divided again into dTOF LiDAR,

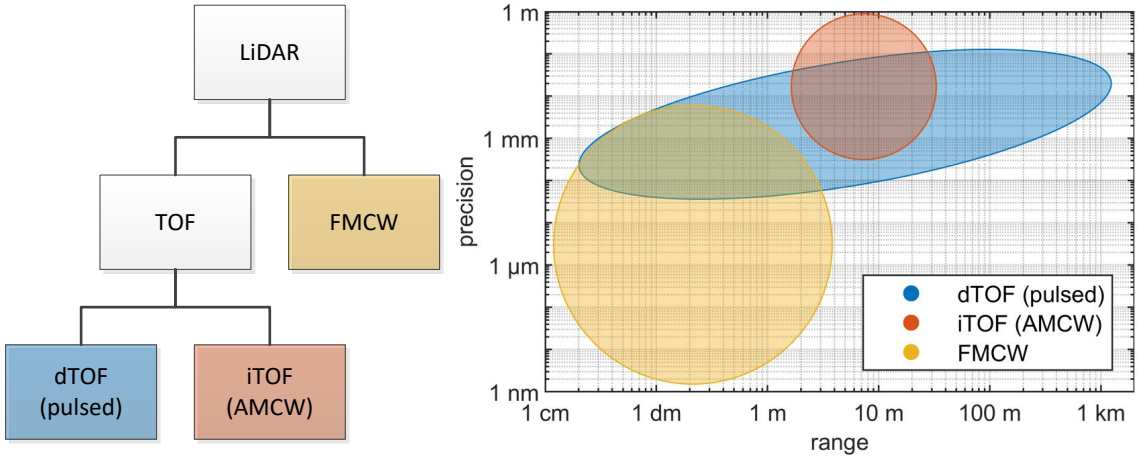

(a) Overview

(b) Precision and range after [1]

Figure 2.1: Representation of most common LiDAR methods. FMCW is based on the light frequency as reciprocal of the wavelength, whereas TOF LiDAR operates in the time domain. dTOF LiDAR is also called pulsed LiDAR and iTOF LiDAR is also called AMCW LiDAR

which is also called pulsed LiDAR, and indirect time-of-flight (iTOF) LiDAR, which is also called amplitude-modulated continuous-wave (AMCW) LiDAR. These methods are suitable for different ranges and precisions of the measured target distances as seen in Figure 2.1b, where the typical performance area of each LiDAR method is shown based on precision and range of academically published and industrial LiDAR systems [1]. With dTOF LiDAR, a moderate distance precision over many orders of range is achieved so that the highest target distances are reached. For iTOF LiDAR, a similar precision is shown but only a moderate range is possible. However, iTOF has other advantageous like low fabrication cost. FMCW systems are able to measure with the highest precision up to a few nanometers but can be limited to a few meters in range. There are recent FMCW LiDAR systems with higher ranges but compared to TOF, these systems can be expensive because of the required laser with widely adjustable wavelength [2]. This work focuses on dTOF LiDAR providing large ranges, which enable promising applications like autonomous driving but also show a higher potential for LiDAR interference than short ranges. However, the increasing research on applications with multiple LiDAR systems but shorter ranges like robotics might increase the interest in interference investigations for all LiDAR methods. In the following, every method is explained in detail with particular focus

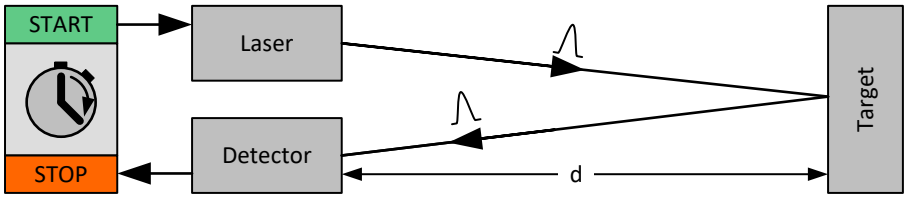

Figure 2.2: Principle of dTOF LiDAR, where the TOF of a reflected laser pulse is measured to determine the target distance d

on single-photon detectors because of their susceptibility to interference.

Direct Time-of-Flight (Pulsed)

For many applications like autonomous driving, the applied LiDAR technique is TOF LiDAR, where the TOF of the emitted and received light is measured as seen in Figure 2.2 and afterwards transformed into a distance. For dTOF LiDAR, short laser pulses are used so that the TOF t_{TOF} can be measured directly by the emission and arrival time of these pulses [3]. Therefore, dTOF LiDAR is sometimes called pulsed LiDAR. The distance d is determined by

$$d = \frac{c \cdot t_{\mathrm{TOF}}}{2}, \tag{2.1}$$

where c is the speed of light. Using SPADs, each photon detection is followed by a dead time of typically 10 ns to 100 ns, within which the SPAD is prepared for the next photon detection [4]. This dead time causes a blind region in the arrival time detection. Assuming a dead time of 20 ns, the light can travel a corresponding distance of about 3 m according to (2.1). However, more relevant is that such a dead time might be longer than the pulse width. If the first photon stems from a laser pulse with a short pulse duration in the order of a few nanoseconds, the next photon might be detected after the end of the pulse. So if the dead time is longer than the pulse width, maximally one laser photon can be detected per pulse, whereas all other photons are from background light.

This is one of the reasons why often only the detection of the first photon is acquired. As it is not known if the origin of this photon is laser or background light, no valid statement can be made based on this single TOF. Even if background light could be excluded, there can still be electrical noise as a potential cause of a triggered event at the LiDAR detector. Therefore, time-correlated single photon counting (TCSPC) is applied, where one photon from each of many successive laser pulses

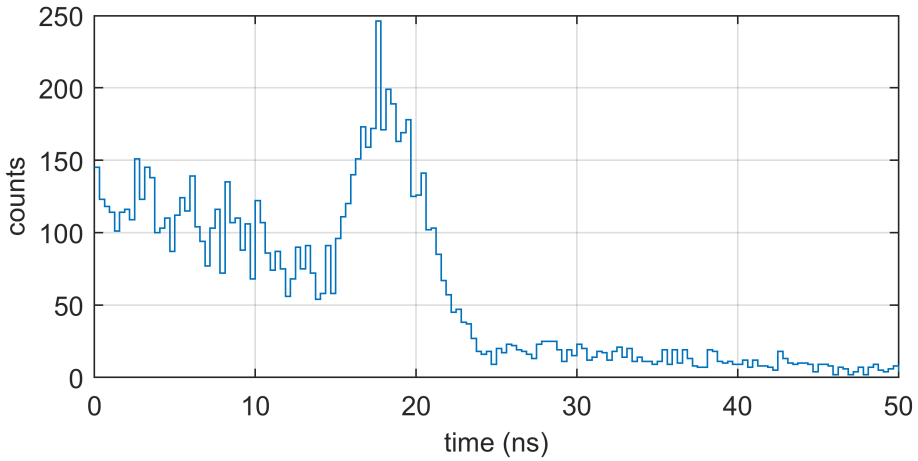

Figure 2.3: Example TCSPC histogram from a LiDAR measurement conducted with LiDAR system *Owl*

is detected before the target distance is determined. For each laser pulse, a first-photon measurement is performed and the TOFs of these photons are accumulated in a histogram. A TCSPC histogram as raw data from a LiDAR measurement is shown in Figure 2.3. In this histogram, the constant background light is detected as an exponential curve, which is called pile-up effect [5][6][7]. This behavior is caused by the first-photon measurement principle because early photons are more likely to be measured than later photons. The pile-up effect changes the laser pulse form as well, which becomes slightly exponential, but especially a narrower pulse width is seen in the histogram. Based on the pile-up effect, the measured pulse also reduces the background detected afterwards so that the exponential function continues lower after the pulse in the histogram. The earliest laser photons represent the shortest distance traveled by the light. Therefore, the rising edge of a laser pulse corresponds to the target distance. The target distance can be extracted from the histogram data by different filter algorithms. If the number of detected background photons is much greater than the number of laser photons in the histogram, the laser TOF can be difficult to determine. Equivalent to background light, an arriving interference signal can suppress the measured pulse due to the first-photon principle. Therefore, this work concentrates on dTOF LiDAR based on SPADs but the results are not necessarily limited to this LiDAR method.

To reduce the background light in the histogram, coincidence detection can be used. A coincidence event is only generated if a specific number of photons is detected within a defined coincidence time. The number of required photon detections

represents the coincidence depth, which are at least two photon detections. The coincidence time must be smaller or equal to the laser pulse width if the coincidence should be predominately triggered by laser photons. Coincidence times slightly larger than the pulse width can also be useful because a background photon before the pulse can be combined with a laser photon afterwards. As arrival time of the coincidence, the last photon can be chosen so that this combination of background photon and later laser photon provides the arrival time of the laser photon. Due to the first-photon principle, the inverse combination of an early laser photon and later background photon is less likely because the laser pulse reduces the detected background light afterwards.

Additionally, multi-event detection can be applied, where multiple photons or multiple coincidence events are acquired after the emission of a single pulse [8][9]. Especially if the dead time is shorter than the laser pulse width, multiple laser photons or multiple coincidence events caused by the laser pulse can be detected. For a dead time higher than the pulse width, multi-event detection can also be useful. Similar to coincidence, the first detected photon can be a background photon so that only a later photon can be detected from the laser pulse. The increased acquisition data requires more storage and data processing. On the other side, the increased number of events can reduce the measurement uncertainty. It must be evaluated if the increase of information justifies the additionally required storage for multi-event detection.

Another possibility of background light reduction is time gating, where the LiDAR system emits the laser pulse as before but the photon measurement is started later so that the reflected laser pulse arrives earlier during the measurement time than before. Especially for far targets, the time between measurement start and pulse arrival time can be reduced, improving the ratio of detected background and laser photons. If the measurement is started too late, the reflected laser light could have already arrived before and hence would be missed in the LiDAR measurement. For optimal time gating, the target distance can be roughly estimated e.g. by the target distance measurement of another sensor like radio detection and ranging (radar). Without prior knowledge of the target distance, an appropriate time gating algorithm can be used, which delays the measurement start step by step through the total measurement time. For a particularly precise target distance determination, the measurement can be repeated with optimal time gating settings, where the

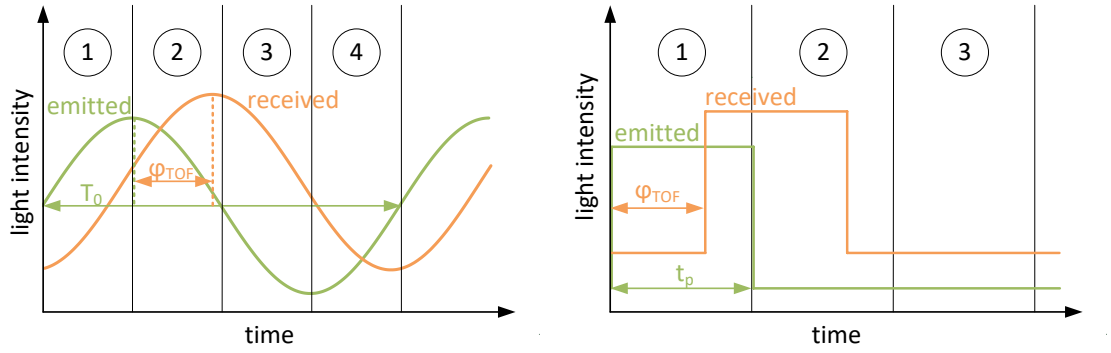

(a) sinusoidal modulation

(b) pulse modulation

Figure 2.4: Two iTOF measurement principles with different light modulation using single-photon detectors resulting in an increased received signal due to background light after [3]

measurement start is set as close as possible to the laser pulse arrival at the LiDAR system. This systematic approach increases the detected laser signal but can also reduce the frame rate of the LiDAR system. The presented methods of coincidence, multi-event and time gating can, individually or in combination, reduce the impact of background light but not necessarily interference signals from other LiDAR systems. Therefore, this work concentrates on dTOF LiDAR measurements without special background suppression settings so that these basic results can be expanded to any combination of coincidence, multi-event and time-gating afterwards. [10]

Indirect Time-of-Flight (AMCW)

For iTOF LiDAR, the TOF is received indirectly by measurements of light intensity during different gating windows as seen in Figure 2.4. The light intensity of the emitted light signal is modulated. Using single-photon detectors, the number of generated events by the reflected light can be counted during consecutive measurement windows. The number of detected photons per measurement window will vary, following the emitted laser modulation form. For example, the laser can be modulated by a continuous-wave (CW) sinusoidal signal or quasi-continuous patterns consisting for example of long rectangular pulses or short pulses. [3]

For sinusoidal modulation, the intensity of a CW signal is modulated by the periodic waveform of a sinusoidal signal [3]. Therefore, this technique is also called

AMCW LiDAR [2]. The principle is shown in Figure 2.4a. The phase difference φ_{TOF} is the TOF calculated from the period duration T_0 via

$$\varphi_{\mathrm{TOF}} = 2\pi \frac{t_{\mathrm{TOF}}}{T_0}, \tag{2.2}$$

where the TOF t_{TOF} can be transformed again into the target distance d by (2.1). For the measurement settings, time gating is applied to adjust the start and the duration of each measurement window. For sinusoidal modulation, the sinus period is divided into multiple measurement windows as seen in Figure 2.4a, where each measurement provides a number of detected events. Assuming four measurement windows, the number of events in the first and third window can represent the sinus signal, whereas the number of events in the second and fourth window are shifted by π representing the cosine signal. Combining both removes the constant background noise floor. With regards to unambiguous range, the maximum distance d_{max} is given by the equivalent equation (2.1) using the period duration T_0, e.g. a period duration of $T_0 = 150\,\mathrm{ns}$ leads to a maximum distance of $d_{\mathrm{max}} = 22.5\,\mathrm{m}$ [11]. [12]

Alternatively, a quasi-continuous-wave signal can be used, e.g. consisting of long pulses, which is called pulse modulation [1][13]. The principle is illustrated in Figure 2.4b. Equivalent to sinusoidal modulation, consecutive time-gated measurement windows with different numbers of events are acquired. Assuming three measurement windows with the same width as the emitted pulse width t_{p}, two measurement windows contain the received signal, whereas the third measurement only provides the constant background level. Equivalent to the sinusoidal modulation, the detectable maximum target distance corresponds to the pulse width t_{p} via (2.1). Depending on the required maximum distance and the available laser sources, continuous light as shown by the sinusoidal modulation or pulsed light like the presented pulse modulation can be chosen for an application. With regards to interference, continuous light of multiple LiDAR systems can produce continuous interference, whereas pulsed light provides the possibility of alternating measurements from different LiDAR systems so that interference can be completely avoided. However, the severity of interference might be higher for pulsed light, as it is used in dTOF LiDAR with first-photon measurement principle. [12]

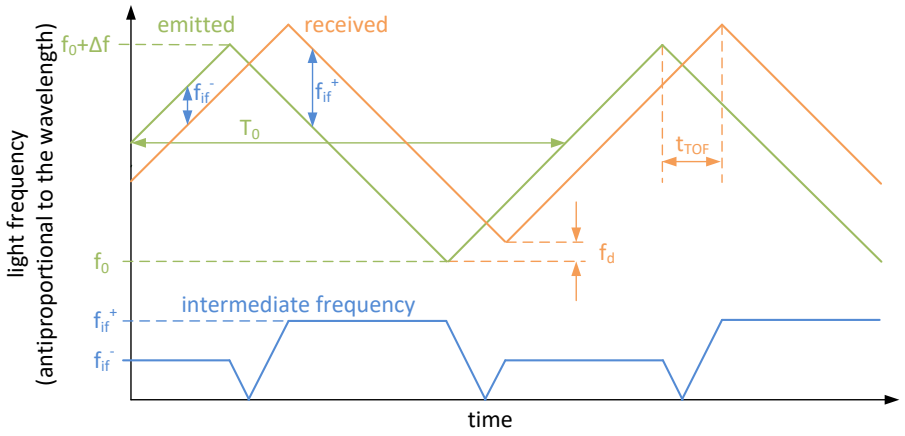

(a) Emitted and received frequencies after [15]

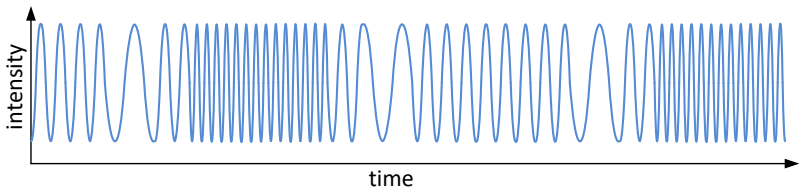

(b) Intermediate beat frequency after [16]

Figure 2.5: FMCW measurement principle based on the determination of the intermediate frequencies f_{if}^{+} and f_{if}^{-} using a light source with adjustable wavelength

FMCW LiDAR

Another recent LiDAR technique is FMCW LiDAR, which also works indirectly by weighting measured intensity values during time intervals but is not included in the longtime studied field of iTOF LiDAR techniques in general [14]. The principle is similar to FMCW radar but instead of the pulse repetition rate, FMCW LiDAR modulates the light frequency, which is proportional to the reciprocal of the wavelength. An example of light frequency modulation is illustrated in Figure 2.5a.

For distance determination, especially the rising linear frequency chirp is used, starting from frequency f_0 with maximum frequency difference Δf corresponding to sweep duration time $T_0/2$. The TOF t_{TOF} is the time delay between the emitted and the reflected signal so that the available maximum target distance is given by the sweep duration time $T_0/2$ using (2.1). In contrast to iTOF LiDAR, the TOF is not determined in time domain but frequency domain. The intermediate frequency

f_{if}^- of emitted and received signal results in

$$t_{\text{TOF}} = \frac{f_{\text{if}}^-}{\Delta f} \frac{T_0}{2}. \tag{2.3}$$

The emitted and reflected signal can be overlapped using an interferometer.

FMCW measurements of moving targets can be influenced by the Doppler effect resulting in a shift of the delayed signal by the Doppler frequency f_{d} as seen in Figure 2.5a. For this modulation scheme, the intermediate frequency in (2.3) should be replaced by the mean value of both beat frequencies f_{if}^+ and f_{if}^- marked in Figure 2.5a, which are both given by the delayed reflected signal but can differ in their heights. The resulting intensity signal of the both beat frequencies is shown in Figure 2.5b. The measured signal can additionally be influenced by different noise sources, e.g. statistical fluctuations of the laser or background radiation [17]. However, FMCW LiDAR is less influenced by background radiation or noise than other LiDAR methods because it suppresses these incoherent sources. There are different techniques to measure the beat frequencies from the measured signal. The simplest method takes the two most distant zero-crossings within one frequency section to count the number of zero-crossing in between, compared to the time duration to get the beat frequency f_{if}^+ or f_{if}^-. Alternatively, techniques like fast Fourier transform (FFT) can be applied to extract the beat frequency of the measured signal [17]. [16]

Besides the distance, the relative velocity can be measured directly from a single measurement using the Doppler effect. Therefore, especially the down sweeping is required, whereas for pure distance determination, a sawtooth signal would be sufficient. For a moving target, the reflected signal is shifted by a constant frequency f_{d} as seen in Figure 2.5a, which is assumed to be smaller than the intermediate frequency with $f_{\text{d}} < f_{\text{if}}$. The Doppler effect can indicate a constant relative velocity with respect to the LiDAR system. For the velocity determination, the Doppler shift is calculated by

$$f_{\text{d}} = \frac{f_{\text{if}}^+ - f_{\text{if}}^-}{2}. \tag{2.4}$$

Then, the velocity of the target is received by

$$v = \frac{c \cdot f_{\text{d}}}{2 \cdot f_0} \cdot \frac{1}{\cos\theta}, \tag{2.5}$$

where c is the speed of light, f_0 the starting frequency of the chirp and θ the angle between the LiDAR line of sight and the target movement direction. If the movement direction is not known ($\theta = 0°$), only the radial velocity component of

this target in the direction of the LiDAR line of sight can be determined. FMCW LiDAR is the only presented method with direct velocity determination from a single measurement, whereas other LiDAR methods require two consecutive distance measurements for the calculation of the velocity. [15]

2.1.2 Photodetectors

To detect the reflected laser light, photoelectric sensors can be applied. In the field of photodiode (PD), there are analogue detectors like avalanche photodiodes (APDs) and the more recent developed digital detectors like SPADs, which are used in this work. Other detectors are for example photomultiplier tubes (PMTs), which are not further discussed here [18].

Avalanche Photodiode

PDs are based on semiconductors, which have an electrical conductivity between those of conductor and insulator. Their electrical structure consist of energy bands. At the lowest temperature of 0 K, the lowest-lying bands are fully occupied by electrons. The highest occupied energy band is called valence band, whereas the one above as fully unoccupied band is known as conduction band. Both bands are separated by the bandgap energy E_g. Photons hitting the semiconductor surface can provide the energy to excite electrons from valence to conduction band. This is the internal photoelectric effect, which has been mathematically described by Albert Einstein in 1905 [19]. The photoelectrons generated by incident photons cause holes at their original positions in the atomic lattice. Holes can also be treated as charge carriers because they move equivalent to electrons but in the opposite direction. [20]

For silicon, the minimum required energy is 1.12 eV, which corresponds to a maximum detectable wavelength of $\lambda_\mathrm{max} = hc/E_\mathrm{g} = 1.1\,\mu\mathrm{m}$, where the photon energy is determined by the speed of light c and the Planck constant h [20]. For lower wavelengths, the sensitivity increases so that the best performance is achieved in the visible range. For example, a silicon SPAD can have the highest photon detection probability (PDP) at 500 nm with 60 % and in the near-infrared range e.g. at 900 nm, the PDP is only 4 % for comparison [21]. However, many applications like autonomous driving require near-infrared wavelengths that are invisible for humans. Besides silicon, LiDAR detectors can be based on other materials like InGaAs, which

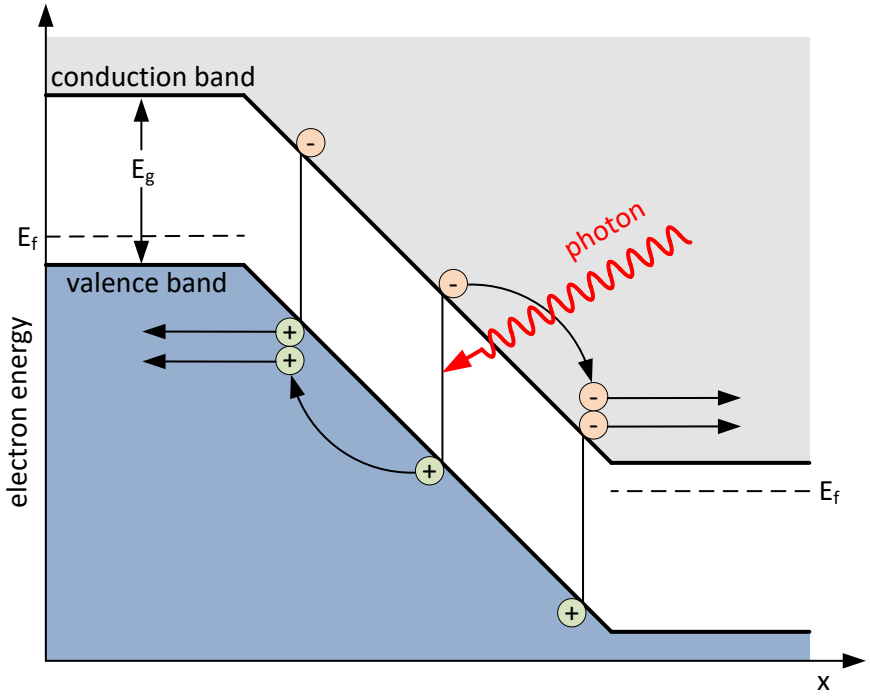

Figure 2.6: Photon detection principle of an APD after [20], where E_f is the Fermi energy and E_g the bandgap energy between valence and conduction band

can operate at higher wavelengths [22]. InGaAs SPADs are sensitive beginning from the near-infrared reaching up to 1.7 µm due to a bandgap of 0.75 eV [23]. Wavelengths beyond 1400 nm allow for orders of higher optical laser powers according to the eye safety standard [2][24]. However, InGaAs detectors are expensive so that the use of silicon SPADs is rather expected for applications with a large number of LiDAR systems, which can be particularly affected by interference.

APDs are photodiodes using large reverse bias voltages so that charged carriers can be accelerated as seen in Figure 2.6. This additional energy allows generated charge carriers to accelerate so much that they can release further electron-hole pairs by impact ionization. Those can produce impact ionization as well resulting in an avalanche. In summary, APDs amplify the electrical signal with a specific gain factor before detection. On the other hand, this gain is responsible for an increased noise. [20]

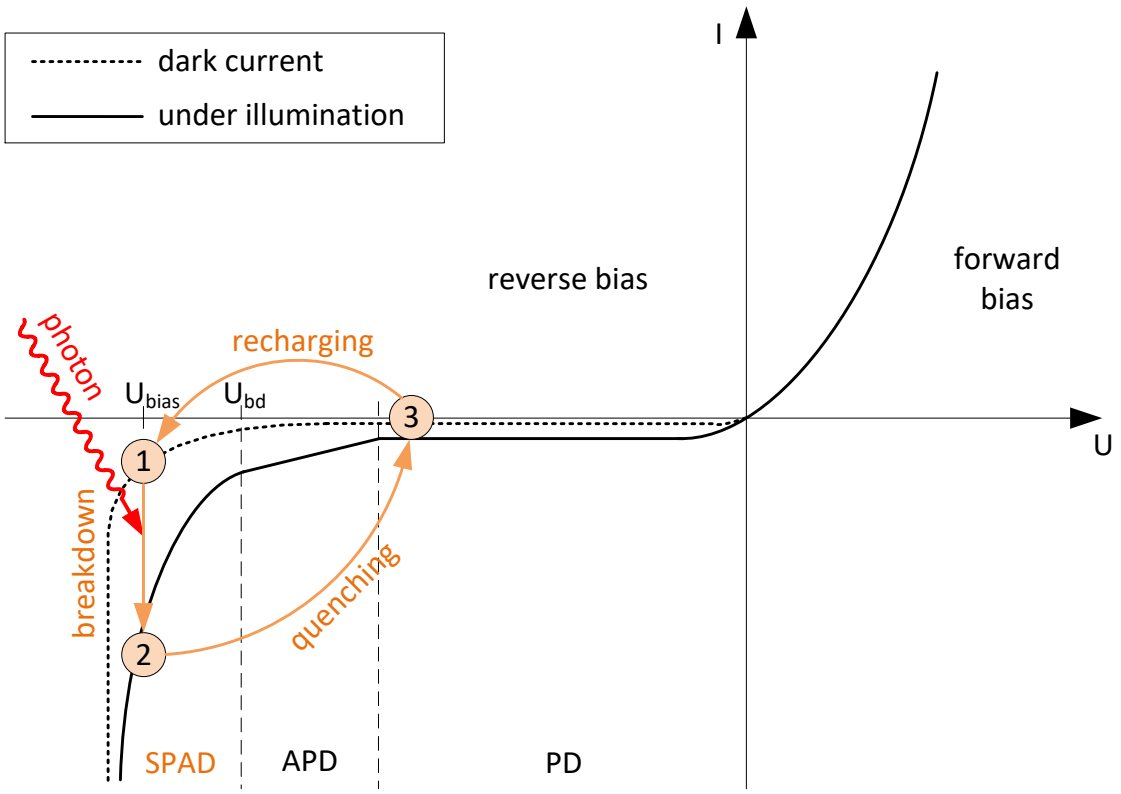

Figure 2.7: Current-voltage characteristics for PD, APD and SPAD with operating points of a SPAD after [25], where U_{bd} is the breakdown voltage and U_{bias} the bias voltage

Single-Photon Avalanche Diode

For the detection of single photons, SPADs are well suited. They are similar to APDs but with an even larger reverse bias voltage as shown in Figure 2.7 so that already a single photon produces an avalanche breakdown as seen in Figure 2.6. Contrary to APDs, the measured electrical signal is not proportional to the incoming light intensity. Here, not only the electrons are accelerated but the holes as well resulting in a large avalanche current. The SPAD represents a digital device because incident photons leads to avalanche breakdowns. Therefore, SPADs are also known as Geiger-mode APDs. The working principle of a SPAD is shown in Figure 2.7. First, the SPAD is charged to the bias voltage at operating point ① in the Figure. Each detected photon causes a breakdown leading to point ②. To reset the SPAD, it is quenched by reducing the voltage below the breakdown voltage to operating point ③ until the high current is stopped. Now, it can be recharged to the bias voltage at

operating point ①. There are several options for quenching. Passive quenching uses a simple resistance. Arriving photons during the quenching phase can expand the passive quenching time. Instead, active quenching controls the quenching process e.g. by a transistor. The SPAD is disabled during a defined hold-off time so that arriving photons have no influence during that time. Due to the quenching process, the SPAD is insensitive after each avalanche during a certain dead time in the order of 10 ns to 100 ns [4]. Therefore, SPAD-based LiDAR systems often measure only the first photon after each laser pulse emission. [3]

In the following, some effects causing noise in the detector are described. One effect is afterpulsing. Depending on the hold-off time of the quenching circuit, most carriers in the SPAD are removed. In silicon detectors, lattice defects can keep an electron or hole, which is released after some nanoseconds. As result, a second avalanche can be produced without a photon arrival. Therefore, this correlated effect is called afterpulsing. Other noise sources are electrical or optical crosstalk. When an avalanche breakdown occurs in a pixel, single electrons can enter adjacent pixels and cause electrical crosstalk. Those pixels can have breakdowns although no photon arrived. Additionally, optical crosstalk can occur when the recombination of an electron-hole pair releases energy to emit a photon, which is called radiative recombination. This photon can again be detected by a neighboring pixel. Furthermore, dark count rate (DCR) as uncorrelated noise can occur, which is independent of any other avalanches in contrast to the noise sources described before. For a single SPAD, this rate is given by avalanches per second without impinging light. Alternatively, the DCR is indicated as avalanches per second and area to compare SPADs with different sizes. The DCR is influenced by the doping quality, bias voltage and temperature. Individual pixels can show an extraordinarily high DCR. These pixels are called hot pixels and can be nearly insensitive to light due to their DCR. The required detector sensitivity and tolerated noise depend on the respective application of the SPAD. [3][20]

Light-generated event rates at DCR level cannot be differentiated by the SPAD. Therefore, the DCR uncertainty represents the lower boundary of the dynamic range. For active quenching circuits, the upper boundary reaches the reciprocal of the dead time. With DCR r_{DCR} and dead time t_{d}, the dynamic range Q of a single SPAD is calculated by

$$Q = 20 \cdot \log_{10}\left(\frac{1}{\sqrt{r_{\mathrm{DCR}}}t_{\mathrm{d}}}\right). \tag{2.6}$$

For example, a DCR of 1 kHz and a dead time of 10 ns result in a dynamic range of 130 dB. SPADs have high dynamic ranges compared to other sensors. The dynamic range of LiDAR systems with multiple SPADs can be further increased, e.g. by coincidence logic, where the photon detections of multiple SPADs are temporally correlated [26]. Finally, SPADs are particularly sensitive to small amounts of light so that they are expected to be also particularly affected by low interfering light from other LiDAR systems. Therefore, this work focuses on LiDAR interference between systems using SPADs. [27]

2.1.3 Light Sources

For illumination, a pulsed laser is used in dTOF LiDAR systems. Short pulse widths lower than 10 ns are advantageous, because photons from the end of the laser pulse arrive later at the detector indicating a larger target distance than earlier arriving photons according to (2.1). For example, an early and late detected photon of a laser pulse with 10 ns pulse width can already cause a distance uncertainty up to 1.5 m given by (2.1). The optical power depends on the chosen field-of-illumination (FOI) representing the illuminated solid angle by the laser opening angles. For many LiDAR applications, the laser wavelength is chosen invisible for human eyes in the near-infrared spectrum, where 700 nm to 1000 nm are suitable for silicon sensors [28] and 1550 nm is often applied for the more expensive InGaAs sensors [22][29]. To exclude background light e.g. sunlight, an optical bandpass filter is placed in front of the sensor with a spectral width in the order of tens of nanometers. The bandpass filter must not be too narrow because the laser has a certain wavelength width of a few nanometers and the central wavelength can drift with changing temperature [30]. The pulse repetition frequency (PRF) depends on the application and reaches values up to 1 MHz for high-speed LiDAR [31][32][33]. To avoid an ambiguous range of the detected target distances, it must be guaranteed that a pulse potentially returns before the next pulse is emitted.

LiDAR Techniques

There are different techniques for the laser beam emission as shown in Figure 2.8, which are described in the following. The simplest realization is flash LiDAR, where the laser illuminates the total observed area at once. These solid-state systems

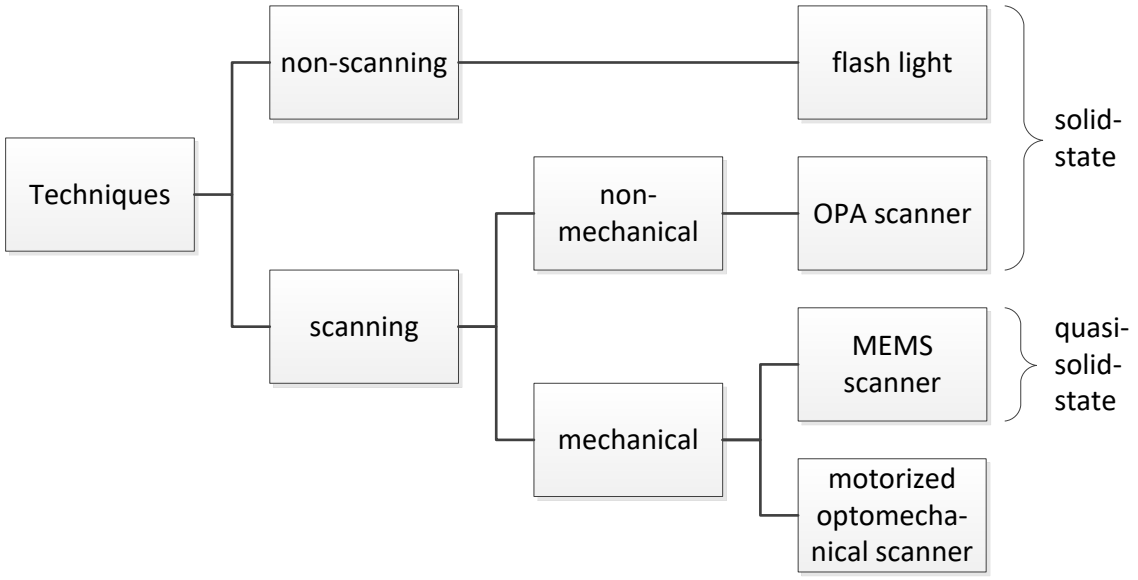

Figure 2.8: Different LiDAR techniques for the laser beam emission after [34]

are considered robust with high durability because they have no moving parts. All pixel measurements can be updated simultaneously and there are no problems with measurement synchronization. A disadvantage is the high laser power, which is required to illuminate such large areas.

Many LiDAR systems apply a scanning technique so that the laser beam moves through the detector field-of-view (FOV). This can be achieved non-mechanically by optical phased array (OPA) scanners, which are solid-state systems like flash systems. Classical scanning systems have mechanical parts. This can be a motorized mirror, which deflects the laser light in the desired direction. Such a scanning system is susceptible to vibration possibly leading to a mismatch between laser FOI and detector FOV. More stable are micro-electro-mechanical system (MEMS) scanners, which can be seen as quasi solid-state systems. The covered scanning laser illumination can be either a small area, a line or even a single point matching only a single detector pixel. Smaller FOVs require smaller optical powers, which are easier to obtain and come along with the great advantage of reduced eye safety limits. On the other hand, the division of the FOV into smaller parts reduces the measurement time per part because the parts are addressed one after the other but the measurement time of the total FOV should remain the same. For scanning LiDAR, the moving laser beam and smaller FOI also reduce the occurrence probability of interference between two LiDAR systems [35]. Therefore, the interference investigations of this

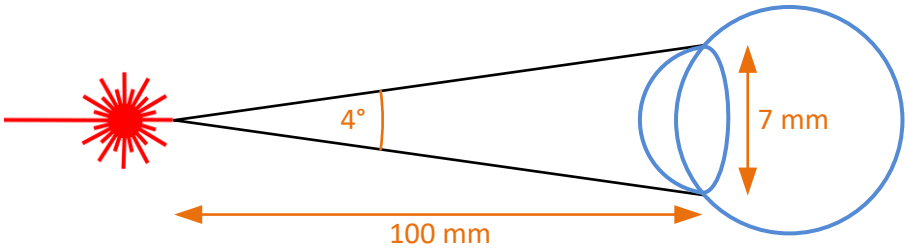

Figure 2.9: Illumination angle of a pupil with regards to eye safety conditions at 10 cm distance to the light source after [25]

work focus particularly on the more frequent case of flash LiDAR interference but the results can be applied to scanning LiDAR as well if the additional laser beam movement is considered. [34]

Eye Safety Considerations

With increasing optical laser power, dTOF LiDAR systems can detect higher target distances. Additionally, higher measurement ranges and higher optical powers provide a larger possibility for interference. However, the emitted laser power is limited with regards to the eye safety for applications including humans. This limit is defined in the IEC standard *Safety of laser products* [24]. The eye safety limit depends on the wavelength. Infrared light is invisible for human eyes but can harm them so that the most restrictive laser class 1 is required for eye safety, which is considered in the following. In contrast, visible laser light allow for higher optical powers classified by laser class 2 because the blink reflex prevents eye damage unless a person intentionally stares in the laser beam for a longer time. For every laser class, the corresponding accessible emission limit (AEL) is defined by the optical power distributed over a pupil with diameter 7 mm in 10 cm distance to the light source as seen in Figure 2.9. The total pupil is illuminated for angles greater than 4°, which is mostly given for flash LiDAR. Besides point sources, laser source areas can be expanded, which is given for vertical-cavity surface-emitting laser (VCSEL) arrays. Additionally, the apparent source size observed by a person through optics can be expanded using diffuse optics. In both cases, more optical power is allowed because the source area is distributed on the retina, whereas more dangerous point sources are imaged on a single point. The AEL per pupil area is given by the most restrictive limit out of three different criteria, which have to be evaluated:

1. Single pulse criterion $\mathrm{AEL}_{\mathrm{single}}$
2. Average power criterion $\mathrm{AEL}_{\mathrm{T}}$ during time T
3. Single pulse train criterion $\mathrm{AEL}_{\mathrm{s.p.train}}$

In the following, a flash LiDAR system with wavelength of 905 nm as it is used in this work, pulse width in the order of nanoseconds and PRF of $f_{\mathrm{p}} \leqslant 200\,\mathrm{kHz}$ is assumed. In this case, the third criterion is always more restrictive than the first criterion given by

$$\mathrm{AEL}_{\mathrm{s.p.train}} = \mathrm{AEL}_{\mathrm{single}} \cdot 0.4 = 79\,\mathrm{nJ}. \tag{2.7}$$

The second criterion is given by a time base of $T = 10\,\mathrm{s}$ resulting in

$$\mathrm{AEL}_{\mathrm{T}} = 0.01\,\mathrm{W} \cdot f_{\mathrm{p}}. \tag{2.8}$$

Depending on the PRF f_{p}, the second or third criterion defines the most restrictive AEL to

$$\begin{aligned} \mathrm{AEL} &= \min\left(\mathrm{AEL}_{\mathrm{single}},\ \mathrm{AEL}_{\mathrm{T}},\ \mathrm{AEL}_{\mathrm{s.p.train}}\right) \\ &= \begin{cases} \mathrm{AEL}_{\mathrm{s.p.train}} & = 79\,\mathrm{nJ}, & f_{\mathrm{p}} < 12.7\,\mathrm{kHz} \\ \mathrm{AEL}_{\mathrm{T}} & = 79\,\mathrm{nJ}...5\,\mathrm{nJ}, & 12.7\,\mathrm{kHz} \leqslant f_{\mathrm{p}} \leqslant 200\,\mathrm{kHz} \end{cases}. \end{aligned} \tag{2.9}$$

The final optical peak power per pulse depends on the laser pulse form. Laser pulse shapes can be assumed as Gaussian distribution or approximated as rectangular pulse form, where t_{p} is the pulse width at full width at half maximum (FWHM) [36]. Assuming a rectangular laser pulse form with pulse width t_{p}, the optical laser power per pulse Φ_{L} is given by

$$\Phi_{\mathrm{L}} = \frac{\mathrm{AEL}}{t_{\mathrm{p}}}. \tag{2.10}$$

Therefore, the laser pulse properties like laser PRF, pulse width and optical power must be optimized with regards to the respective LiDAR application considering the eye safety limit. [24]

2.1.4 Example LiDAR System *Owl*

This work focuses on dTOF LiDAR using SPADs. For measurements, the dTOF LiDAR system *Owl* with sensor *CSPAD alpha* from Fraunhofer IMS as seen in Figure 2.10 is used [38]. The name *Owl* is adopted from the corresponding animal

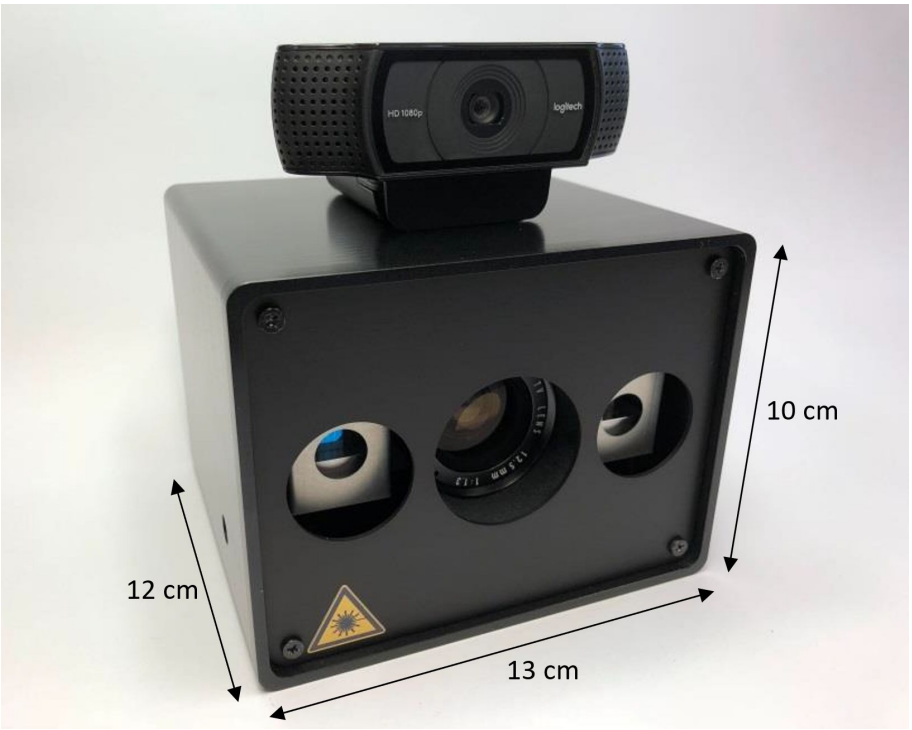

Figure 2.10: LiDAR system *Owl* from Fraunhofer IMS utilizing two lasers and sensor *CSPAD alpha*. On top, a webcam is installed. [37]

due to the similarity, where the two lasers represent two eyes. These lasers of type *LS9-220-8-S10* operate at wavelength 905 nm each with 220 W, which emit simultaneously to achieve a total optical power of 440 W [39]. The laser pulse width is 8 ns and the laser PRF is 10 kHz. The system *Owl* detects light through the optical bandpass filter with central wavelength 905 nm and a width of 30 nm. The sensor *CSPAD alpha* has 64×48 pixels in counting mode. This mode is used to obtain the background intensities per pixel with the lasers switched off by counting the number of avalanches during a few microseconds. In timing mode, *CSPAD alpha* has 32×24 pixels to perform the LiDAR measurement for distance determination. Each pixel consists of four SPADs, which can be combined for coincidence measurements. Their total area contributes to the optical fill factor of 3.64 %, which is the proportion of the all SPAD areas to the total pixel area. The system has a PDP of about 4 % at a wavelength of 905 nm and a DCR of 200 Hz to 700 Hz for about 70 % of all pixels, which is equivalent to 1.3 cps/µm^2 to 4.5 cps/µm^2 and a dead time of 20 ns resulting in a dynamic range of 126 dB corresponding to (2.6). The timing resolution is given by the so-called bin width 312.5 ps corresponding to a distance resolution of 4.7 cm

Table 2.1: Parameters of LiDAR system *Owl* from Fraunhofer IMS divided in light parameters, pixel parameters and timing parameters

Parameter	Symbol	Unit	Value
Wavelength	λ	nm	905
Optical laser power	Φ_L	W	440
Pulse width	t_p	ns	8
PRF	f_p	kHz	10
Bandpass filter	λ_filt	nm	905 ± 15
Number of SPADs per pixel	n_SPAD	–	4
Fill factor	η_FF	%	3.64
PDP	η_PDP	%	4
DCR	r_DCR	cps/µm^2	$1.3 - 4.5$
Number of pixels:			
1) counting mode	$n_\mathrm{H} \times n_\mathrm{V}$	–	64×48
2) timing mode	$n_\mathrm{H} \times n_\mathrm{V}$	–	32×24
Dead time	t_d	ns	20
Bin width	t_bin	ps	312.5

by (2.1).

2.2 Generated Event Rates in LiDAR Systems

Using dTOF with SPADs, single photons can be detected and the total LiDAR measurement can be described with regards to photon statistics. Not every photon produces an avalanche in a SPAD. For example, a photon can produce an electron-hole pair, which recombines instead of producing an avalanche. Vice versa, not every avalanche is caused by a photon but can be produced by the DCR. Therefore, the number of produced avalanches per second is neutrally described as event rate. Although the event rate is not equal to the incident photon rate, the photon rate determines the expected event rate. In the following, the expected event rates at the LiDAR system received from the target reflection are derived. The light received from the target consists of the laser pulse emitted by the LiDAR system and the background light, which is also reflected by the target to the LiDAR system.

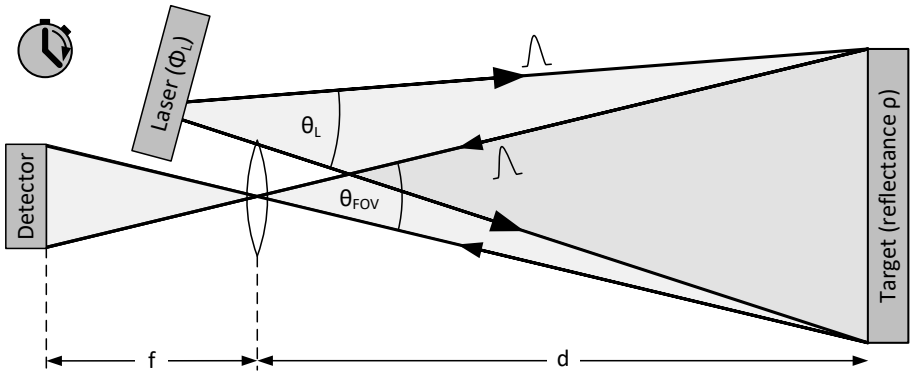

(a) Emission and detection of laser pulses [40]

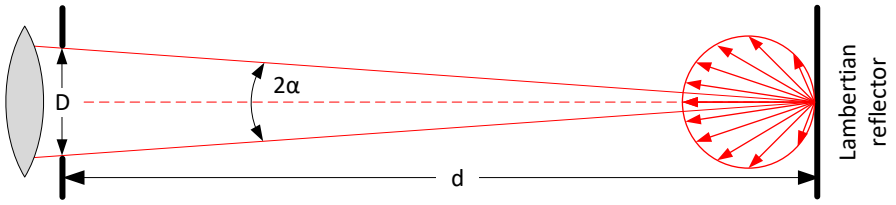

(b) Lambertian reflection received at the LiDAR aperture after [41]

Figure 2.11: Principle of dTOF LiDAR with short laser pulses

This light passes through the optics to the SPADs, where it produces avalanche breakdowns as described in section 2.1.2. There, the laser-generated or background-generated event rate is the number of avalanches per second induced in all SPADs of a pixel due to the laser or background. From these rates, the influencing parameters and the expected signatures of LiDAR measurements can be investigated.

2.2.1 Laser-Generated Event Rate

The generation of the event rate due to laser light is illustrated in Figure 2.11. The laser light origin is the emission of a laser pulse with optical power Φ_L from the LiDAR system towards the target. The laser light is expanded at an angle $\theta_{\mathrm{L,H}}$ in the horizontal dimension and at an angle $\theta_{\mathrm{L,V}}$ in the vertical dimension. In the case of flash LiDAR, the pixel FOV is smaller than the laser solid angle. From this laser FOI, a single pixel cuts out its pixel FOV resulting in the factor

$$\eta_\mathrm{illum} = \frac{\min\left(\Omega_\mathrm{px}, \Omega_\mathrm{L}\right)}{\Omega_\mathrm{L}} = \frac{\min\left(A_\mathrm{target,px}, A_\mathrm{illum}\right)}{A_\mathrm{illum}}, \tag{2.11}$$

where the minimum function denotes the case of scanning LiDAR with the FOI lying within the pixel FOV so that the total laser light is distributed on a single pixel.

Alternatively, the illuminated target can be imagined, where a pixel only observes a small area $A_{\text{target,px}}$ from the illuminated target are A_{illum}. A rectangular target area A at target distance d illuminated by a laser or observed by a pixel using the angles $\theta_{\text{H}} \times \theta_{\text{V}}$ is given by

$$A = 4d^2 \tan\left(\frac{\theta_{\text{H}}}{2}\right) \tan\left(\frac{\theta_{\text{V}}}{2}\right). \tag{2.12}$$

From the target, the laser light can be reflected in many different forms, which can depend on the incident angle. A good approximation for many targets is the assumption of a diffuse reflection as seen in Figure 2.11b following the ideal Lambertian law given by

$$I(\alpha) = L \int\int \cos(\alpha)\ \mathrm{d}A_{\text{target,px}}\mathrm{d}\Omega, \tag{2.13}$$

where L is the constant radiance providing the intensity per area and Ω is the radiating solid angle starting from a single reflecting target point [42]. The central beam from a Lambertian reflection perpendicular to the target surface has the highest intensity with $I(\alpha) = I(0°)$, which falls laterally at an angle of α with $\cos(\alpha)$. Lambertian targets create the impression that they have the same brightness from every point of view because besides the reduced intensity, the observed area from a side view on a flat area is increased as well by $\cos(\alpha)$. In sum, the seen intensity stays the same from every point of view. The Lambertian reflection distributes the light in the total hemisphere independent of the incident angle. For the following calculations, we assume a LiDAR system perpendicular to the Lambertian target surface. The light loss from the Lambertian reflection to the LiDAR aperture D collecting the reflected light is given by the integration in spherical coordinates of the light on the aperture within angle α compared to the total reflected light within the total hemisphere given by

$$\eta_{\text{refl}} = \rho \frac{\int_0^{2\pi}\int_0^{\alpha} \cos(\theta)\sin(\theta)\mathrm{d}\theta\mathrm{d}\phi}{\int_0^{2\pi}\int_0^{\frac{\pi}{2}} \cos(\theta)\sin(\theta)\mathrm{d}\theta\mathrm{d}\phi} \approx \rho\left(\frac{D}{2d}\right)^2, \tag{2.14}$$

where 2α is the small angle of the aperture as viewed from the target allowing for small angle approximations and ρ is the target reflectance reducing the reflected light additionally [3][43]. Moreover, the light intensity can be reduced in the air

or in the LiDAR optics resulting in a total transmission factor $T = T_{\text{air}} \cdot T_{\text{optics}}$. After the optics, the light arrives at the detector. The detector sensitivity depends on the PDP η_{PDP} due to the material properties, which is mainly given by the silicon properties for LiDAR system *Owl* described in section 2.1.4. Furthermore, the amount of detected light depends on the optical fill factor η_{FF} providing the proportion from optically active area to the total pixel area. In combination, the photon detection efficiency (PDE) is determined by

$$\eta_{\text{PDE}} = \eta_{\text{PDP}} \cdot \eta_{\text{FF}}. \tag{2.15}$$

Finally, SPADs as digital detectors measuring single photons indicate the received optical power based on the number of photons so that the optical power must be divided by the photon energy E_{ph} given by

$$E_{\text{ph}} = \frac{\lambda}{hc}, \tag{2.16}$$

where λ is the wavelength, h the Planck constant and c the speed of light. Combining all light transformations, the laser-generated event rate r_{L} at the LiDAR system is given by

$$r_{\text{L}} = \Phi_{\text{L}} \cdot \eta_{\text{illum}} \cdot \eta_{\text{refl}} \cdot T \cdot \eta_{\text{PDE}} \cdot \frac{1}{E_{\text{ph}}}. \tag{2.17}$$

This is the expected event rate of a rectangular laser pulse form. To estimate the number of detected photons during the total laser pulse, the laser-generated event rate r_{L} can be multiplied with the pulse width t_{p}. For example, for a laser-generated event rate of 1 GHz combined with a short pulse width of 8 ns, only 8 possible photon detections are expected at the detector from one laser pulse.

2.2.2 Background-Generated Event Rate

For many LiDAR applications, the background light in LiDAR measurements is mainly given by sunlight. There are different solar spectra depending on the position on the earth or the incident angle so that the sunlight transmits more or less absorbing air mass from the sun to the earth surface. In this work, the solar spectrum AM1.5G as shown in Figure 2.12 is used. This solar spectrum assumes 1.5 air masses and average global conditions on a tilted plane at 37° toward the sun, which is equivalent to a zenith angle of 48° [46][47][48]. The spectrum is defined at sea level. The emitted sunlight can be approximated by an idealized black-body

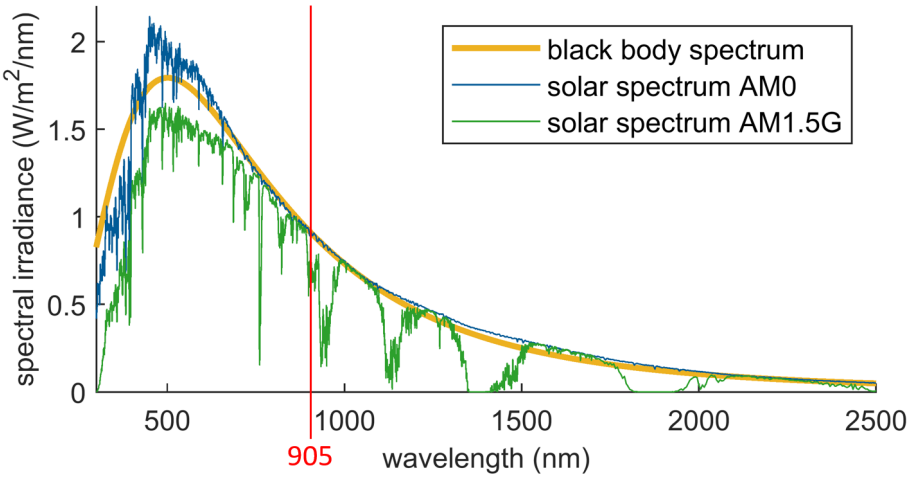

Figure 2.12: Solar spectrum approximated by a black body with temperature 5777 K after [44], measured solar spectrum AM0 without atmospheric transmission after [45] and measured solar spectrum AM1.5G under average global conditions at sea level with zenith angle of 48° through the atmosphere after [46][47]

radiation at an effective temperature of 5777 K [44]. This idealization is close to the measured solar spectrum AM0, which is measured above the atmosphere and hence considers 0 air masses [45]. In comparison to that, the solar spectrum at earth AM1.5G is visibly reduced and contains so-called atmospheric windows, where the sunlight is strongly reduced due to specific molecules in the atmosphere absorbing specific wavelengths. At the wavelengths of these windows, light can be emitted and received very well. The wavelength of 905 nm used by LiDAR system *Owl* lies within such an atmospheric window as seen in Figure 2.12. The parameter η_B is used as a percentage of the maximum background light caused by the sun. Especially for autonomous driving, the background light is given as the photometric illuminance E_v with the unit Lux. Photometric quantities characterize the world as seen by humans which is indicated by the index v standing for *vision*. The corresponding radiometric irradiance E_e with the unit W/m^2 uses e as index because it describes the world with regards to energy. The illuminance E_v is determined by the irradiance E_e according to the luminosity function $V(\lambda)$ as average spectral sensitivity of human visual perception of light, which is also called V-lambda curve [49]. The human vision is defined for wavelengths of 360 nm to 830 nm. Integrating the spectral irradiance $S(\lambda)$ of the solar spectrum AM1.5G over the total wavelength

range provides the maximum illuminance $E_{\mathrm{v,max}}$ by

$$E_{\mathrm{v,max}} = \int_{380\,\mathrm{nm}}^{780\,\mathrm{nm}} K_{\mathrm{m}} \cdot S(\lambda)\,\mathrm{d}\lambda \approx 110\,\mathrm{klx}, \tag{2.18}$$

where the constant $K_{\mathrm{m}} = 683\,\mathrm{lm\,W^{-1}}$ is the maximum value of the photopic luminosity function $V(\lambda)$ for daytime vision. For nighttime vision, the scotopic luminosity function $V'(\lambda)$ has to be applied with $K'_{\mathrm{m}} = 1700\,\mathrm{lm\,W^{-1}}$. Actually, the illuminance given for the visible wavelength spectrum appears to be misleading for LiDAR systems using near-infrared light. However, it is common to use this quantity at autonomous driving and additionally, illuminance provides the possibility to estimate the background light of a scenario based on the human visual perception. This calculation is valid with the assumption that the brightness percentage factor η_{B} of a scenario is the same for all wavelengths of the solar spectrum. For example, if approximately half of the visual light is given with 50 klx, there is also half of the near-infrared light assumed and the background factor is chosen to be $\eta_{\mathrm{B}} = 50\,\%$.

The amount of near-infrared light received at the detector is determined through an optical bandpass filter transmitting wavelengths from $\lambda_{\mathrm{filt,min}}$ to $\lambda_{\mathrm{filt,max}}$. Integrating the spectral irradiance $S(\lambda)$ of the solar spectrum AM1.5G over the theoretical bandpass filter width approximately provides the irradiance reaching the detector given by

$$E_{\mathrm{e}} = \int_{\lambda_{\mathrm{filt,min}}}^{\lambda_{\mathrm{filt,max}}} S(\lambda)\,\mathrm{d}\lambda. \tag{2.19}$$

The maximum irradiance is given without bandpass filter for the integral from $\lambda_{\mathrm{filt,min}} = 0\,\mathrm{nm}$ to $\lambda_{\mathrm{filt,min}} = \infty$ resulting in $E_{\mathrm{e,max}} = 1000.4\,\mathrm{W\,m^{-2}}$. The determined irradiance is distributed on the target area $A_{\mathrm{target,px}}$ seen by one pixel, which can be calculated by (2.12). The sunlight is also subject to the Lambertian reflection with the same reduction factors as for the laser light. The air transmission T_{air} might differ because the solar spectrum already includes the air transmission to the target at sea level so that only the air transmission from the target to the LiDAR system has to be added. Finally, the background-generated event rate r_{B} is determined by

$$r_{\mathrm{B}} = \eta_{\mathrm{B}} \cdot E_{\mathrm{e}} \cdot A_{\mathrm{target,px}} \cdot \eta_{\mathrm{refl}} \cdot T \cdot \eta_{\mathrm{PDE}} \cdot \frac{1}{E_{\mathrm{ph}}}. \tag{2.20}$$

The laser-generated and background-generated event rate only differ by their target illumination seen by one pixel Φ_{target} given by

$$\Phi_{\text{target}} = \begin{cases} \Phi_{\text{target,L}} = \Phi_{\text{L}} \cdot \eta_{\text{illum}}, & \text{laser illumination} \\ \Phi_{\text{target,B}} = \eta_{\text{B}} \cdot E_{\text{e}} \cdot A_{\text{target,px}}, & \text{background illumination} \end{cases}, \tag{2.21}$$

where $\eta_{\text{illum}} = 1$ is possible for scanning LiDAR systems illuminating only one pixel at a time. The background-generated event rate is seen continuously from LiDAR systems, whereas the laser-generated event rate only occurs during the pulse width. Thus, the optical laser power $\Phi_{\text{target,L}}$ indicates the height of a laser pulse, whereas the optical background power $\Phi_{\text{target,B}}$ represents the continuous background power.

2.3 TCSPC Histograms from LiDAR Measurements

For dTOF LiDAR, the target distance cannot be determined from a single first-photon measurement because it can be either a background or laser photon. Therefore, multiple photon measurements are performed during a frame and their arrival times are accumulated in a TCSPC histogram. For each measurement, one laser pulse is emitted and one photon with corresponding arrival time can be detected so that the maximum number of detected photons in the histogram is the number of accumulated measurements. In the following, the statistical modeling of the measured histogram data is presented, which can be used for theoretical calculations and predictions. After that, the simulation of histogram data is explained, which represents a fast histogram analysis possibility including measurement fluctuations. From the histogram data, the target distance must be determined by data processing, which is described in the last section.

2.3.1 Statistical Modeling of Histogram Data

The statistical modeling of the photon statistics is useful to estimate the expected count distribution in a histogram as shown in Figure 2.13b. For simplicity, rectangular pulse forms are assumed so that the laser-generated event rate r_{L} is constant during the pulse width. This model can be extended to more complex temporal intensity profiles but this can also increase the computation time of simulations,

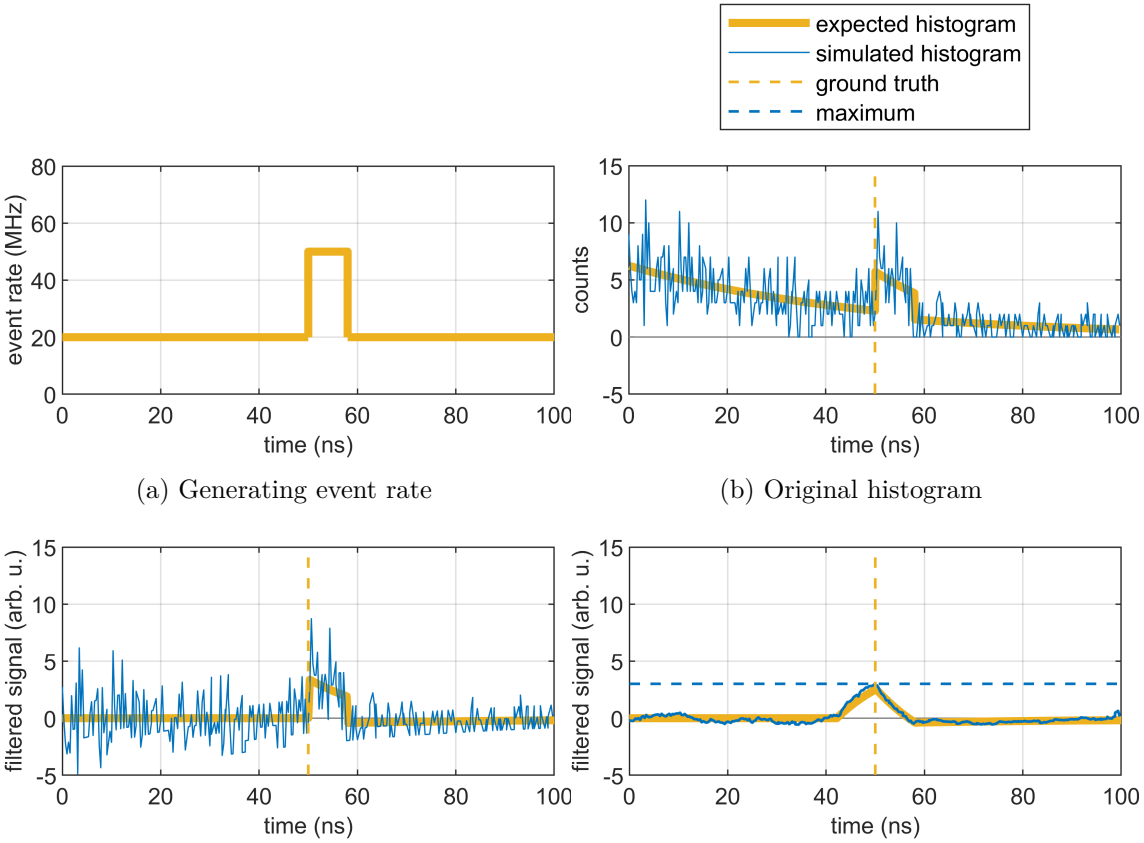

(a) Generating event rate

(b) Original histogram

(c) Background subtraction

(d) Mean filter and maximum detection

Figure 2.13: Algorithm steps of example data processing for one pixel to determine the target distance from the TCSPC histogram

which are described in the next section. Assuming a constant generated rate r at the SPADs of a pixel, the probability to detect the first photon $P_1(t)$ is given by the rate and the condition that no photon has been detected before with

$$P_1(t) = r \cdot \left(1 - \int_0^t P_1(\tau)\mathrm{d}\tau\right) \quad \Leftrightarrow \quad \frac{\mathrm{d}P_1(t)}{\mathrm{d}t} = -r \cdot P_1(t), \tag{2.22}$$

which can be differentiated with respect to the time t to obtain the differential equation of the first-photon process. This differential equation can be solved resulting in the probability $P_1(t)$ to detect the first photon at time t given by

$$P_1(t) = r \cdot \mathrm{e}^{-rt}, \quad t \geqslant 0, \tag{2.23}$$

where a constant event rate r arrives at the pixel. For a constant rate r, this is found to be a special case of the Erlang distribution $P_n(t)$ providing the probability

to detect k photons until time t given by

$$P_k(t) = \begin{cases} \frac{r^k t^{k-1}}{(k-1)!} \mathrm{e}^{-rt}, & t \geqslant 0 \\ 0, & t < 0 \end{cases}, \tag{2.24}$$

which can be used for multi-event detection if the dead time is neglected. The Erlang distribution $P_k(t)$ specifies the number of photons k and provides probabilities for times t to detect the k-th photon, whereas the Poisson distribution $P_r(k)$ as complementary function specifies the time interval t to one second as reciprocal of the rate r and provides the probabilities to detect different numbers of photons $k = 0, 1, 2, \ldots$ during that time. Before and after the arrival of the laser pulse at the LiDAR system, the constant background-generated event rate r_B is present at the SPADs. The total event rate $r(t)$ at one pixel is given by

$$r(t) = r_\mathrm{B} + r_\mathrm{L} \left[\Theta(t - t_\mathrm{TOF}) - \Theta(t - t_\mathrm{TOF} - t_\mathrm{p})\right], \tag{2.25}$$

where the background-generated event rate r_B is temporarily increased by the laser-generated event rate r_L. The Heaviside function $\Theta(t)$ mathematically describes the switching on of the laser pulse during the pulse width t_p beginning from the TOF t_TOF. This time-dependent rate $r(t)$ can be inserted in (2.22) instead of the constant rate r. Solving the new differential equation, the probability density function (PDF) of a TCSPC histogram is given by

$$P(t) = \begin{cases} r_\mathrm{B} \mathrm{e}^{-r_\mathrm{B} t}, & 0 \leqslant t < t_\mathrm{TOF} \\ (r_\mathrm{B} + r_\mathrm{L}) \mathrm{e}^{r_\mathrm{L} t_\mathrm{TOF}} \mathrm{e}^{-(r_\mathrm{B} + r_\mathrm{L})t}, & t_\mathrm{TOF} \leqslant t < t_\mathrm{TOF} + t_\mathrm{p} \\ r_\mathrm{B} \mathrm{e}^{-r_\mathrm{L} t_\mathrm{p}} \mathrm{e}^{-r_\mathrm{B} t}, & t_\mathrm{TOF} + t_\mathrm{p} \leqslant t \end{cases}. \tag{2.26}$$

The detailed derivation of this PDF is found in the appendix A. To obtain the expected count values of a measured histogram, the PDF is integrated over the bin width t_bin and multiplied by the number of measurements per histogram n_meas, which can be approximated by the prefactor $t_\mathrm{bin} n_\mathrm{meas}$. The PDF is useful to determine the expected behavior of histograms under certain conditions. The analytically derivation e.g. of measurement probabilities or expectation values is a fast method to make predictions with regards to new research questions. However, these expectation values cannot be evaluated without variances or uncertainties, but the error propagation can be difficult to determine. Moreover, complex correlations like extensive filter methods applied to the histogram can partly not be calculated explicitly,

for example due to analytically unsolvable integrals. Instead, a fast simulation of the histogram can quickly provide the required information.

Multi-event detection, coincidence detection and time gating can be included in the derived PDF. For example, multi-event detection can be integrated by the general Erlang distribution with k photon detections in (2.24) instead of the first-photon distribution in (2.23) [50]. Coincidence and time gating mainly affect the generated event rates of background and laser at the detector. For example, the coincidence rates can be calculated and inserted instead of the coincidence-free background- and laser-generated event rates r_B and r_L [51]. Therefore, this work concentrates on the basic LiDAR principle without these three techniques so that the results on interference can be transferred to the respective technique by the mentioned adaptions if desired.

2.3.2 Simulation of Histogram Data

The simulation of TCSPC histograms as LiDAR raw data is suitable to obtain the expected performance of a LiDAR system under various circumstances. Especially filter algorithms applied to the histogram data can be tested considering fluctuations caused by photon statistics. An example simulation of a histogram is shown in Figure 2.13b. Using a random number $x \in (0, 1]$, the histogram simulation begins with the generation of a single photon arrival time t_ph according to (2.23) by

$$t_\mathrm{ph} = -\frac{\ln(x)}{r}, \tag{2.27}$$

where r is the present constant event rate. As the underlying Poisson processes caused by different event rates are independent of each other, the background and laser arrival times can be considered separately. For each emitted laser pulse and conducted LiDAR measurement, a background arrival time with background-generated event rate r_B is generated. The generated arrival times by (2.27) are always greater or equal than zero, but they can be later than the acquisition time of the LiDAR system corresponding to the histogram length t_hist. If the generated background photon arrival time is larger than the histogram length, this arrival time is discarded. The laser photon arrival time is generated in the same way with r_L. This arrival time is already discarded if it exceeds the laser pulse width. Otherwise, it is summed up to the ideal TOF. If both the background and laser photon arrival

time are discarded, the simulated arrival time measurement counts as false detection, which is equivalent to a LiDAR system detecting nothing during the current measurement time. If both arrival times are valid, the earlier arrival time is kept according to the first-photon measurement principle. This arrival time simulation is repeated until the desired number of measurements per frame is reached resulting in one histogram. All simulated arrival times are sorted into a histogram. The number of measurements corresponds to the number of emitted laser pulses per frame, but the histogram can contain less counts or even no count at all because of false detections. As seen in Figure 2.13b, the simulated histogram matches well with the expected histogram based on the theoretical PDF.

2.3.3 Histogram Data Processing

There are many filtering algorithms to extract the laser TOF from the histogram to determine the target distance by (2.1). Depending on the respective application, the algorithms can be optimized to perform particularly fast or to provide very precise target distances. In the following, one example of data processing is introduced. The presented algorithm can be applied on many LiDAR applications, which can also include background light. The different steps of this data processing algorithm are shown in Figure 2.13. In contrast to Figure 2.3, the outlines of the single bins are not drawn anymore. Instead, all bin entries are directly connected with a line for simplicity.

There can be many more background events in a histogram than detected laser photons as seen in Figure 2.13b. Furthermore, the exponential background curve can be very high at the histogram beginning which makes background challenging. As first filter step, the exponential background is subtracted following (2.23). For this purpose, the incoming background-generated event rate r_B must be known, which can be measured separately. For the measurement of the continuous background rate, the LiDAR system can operate in a counting mode instead of a timing mode. During a specific measurement time, the number of detected background photons is simply counted without recording the arrival times. Due to the dead time t_d, the LiDAR detector can miss arriving photons. This dead time effect can be statistically corrected to estimate the background-generating event rate r_B by

$$r_\mathrm{B} = \frac{r_\mu}{1 - r_\mu t_\mathrm{d}}, \tag{2.28}$$

where r_μ is the measured photon rate, which is calculated by the measured number of background photons divided by the measurement time. The determined event rate r_B can be used to subtract the exponential background distribution so that only the fluctuations remain from the background light as seen in Figure 2.13c. The expected fluctuation of each bin is given by the square root of the counts in this bin [52]. As the first bins contain the most background counts, the fluctuations are also highest there at the histogram beginning. The fluctuations can increase or decrease the number of counts per bin, but their mean value is expected to be zero. To reduce the fluctuations, the histogram is smoothed by a forward-looking mean filter using a filter width as large as the pulse width. At the beginning of the pulse, this mean filter averages all bins containing possible laser photons. This bin represents the TOF and is expected to be the bin with the highest number of counts in the histogram now so that it can be identified by a maximum detection and converted to the target distance by (2.1). For the example histogram in Figure 2.13d, the determination of the target distance has been successful.

2.4 LiDAR Applications Affected by Interference

There are many different LiDAR applications, but not all of them are strongly affected by interference. Applications with only one LiDAR system are not affected by interference, whereas applications with many LiDAR systems are more critical. Some exemplary applications are presented in Figure 2.14, which are divided into the three main applications of transport, mapping and reconnaissance, supplemented by applications summarized under other uses.

The first main application is transport e.g. of materials or persons. For this purpose, especially industrial applications often use robots [53], whereas human transport is often performed by autonomous driving [29]. Furthermore, transport includes aircraft e.g. planes or drones [54], watercraft e.g. for ship navigation [55], and spacecraft e.g. concerning satellites [56]. Robotics and autonomous driving can provide situations with multiple LiDAR systems in the same location. Drones move in 3D space so that even more LiDAR system can be present in the same space. For ships and satellites, there might be less systems in the same location but interference might still occur. In total, transport applications show an increased probability for potential LiDAR interference.

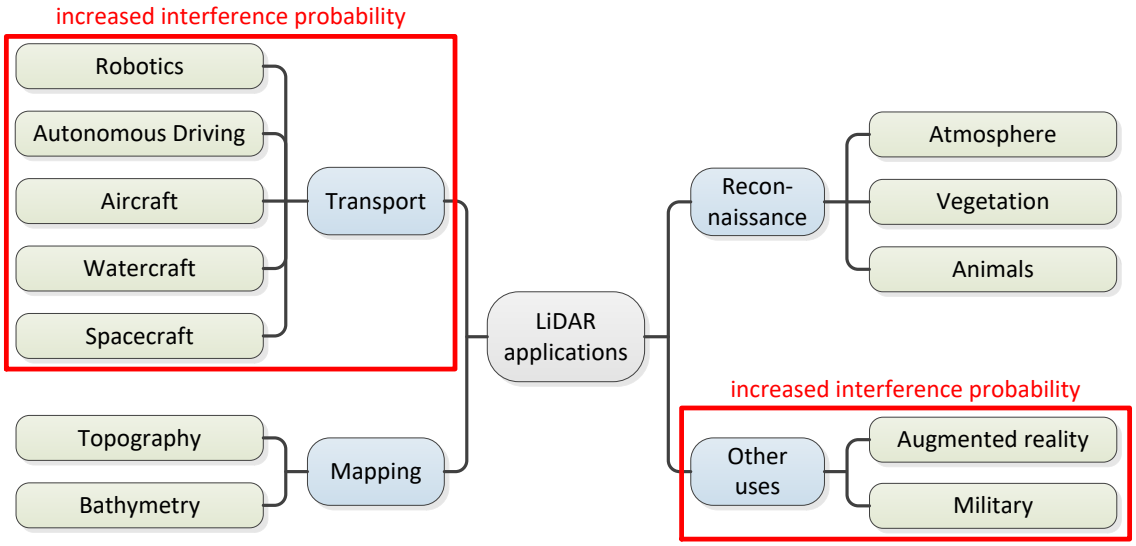

Figure 2.14: Exemplary LiDAR applications with regards to their interference probability

The second main application is mapping, which can be divided into topography as land mapping [57] and bathymetry as underwater mapping [58], e.g. in the field of archaeology, mining or modeling of landslides or tsunamis [59–61]. Although the environments itself are uncontrolled and unknown, mapping can be planned or coordinated because each area is required to be scanned only once by a LiDAR system to create a map. Of course, LiDAR systems from other applications like transport can be present. However, from the application of mapping itself, multiple LiDAR systems in the same location are not expected so that the total interference probability might be low.

A third main application is environment surveillance. Atmospheric LiDAR determines the air composition, e.g. concerning gases, aerosols and clouds, as well as wind, which is especially interesting for renewable energy [62]. The observation of vegetation is used for agriculture or forestry [63, 64]. Moreover, LiDAR is suitable for animal surveillance, e.g. to control the animal species diversity [65]. Similar to the mapping applications, the environment surveillance mostly requires only one LiDAR system per observation target. Therefore, the interference probability is considered to be low.

Other uses possibly affected by LiDAR interference are for example augmented reality [66] and military purpose [67]. Augmented reality can be used by many people in the same location and might require high frame rates in the order of

human perception so that there might be many interference signals at the same time. Military applications can include transport with increased interference probability as discussed before, but the detection ranges might be larger than those of transport applications.

This work concentrates on LiDAR system parameters applied in the field of transport because these applications often implies uncontrolled environments with several LiDAR systems potentially leading to LiDAR interference. Furthermore, transport has particularly high safety requirements, especially with regards to the transport of people.

Chapter 3

Occurrence Probability of Interference

Interference is one of the main challenges to be overcome before using LiDAR in applications with multiple systems like autonomous driving. At first, it must be clarified how interference is defined yielding different interference types and under which conditions interference occurs. After that, the spatial and temporal conditions for the occurrence of interference are analyzed with regards to the different interference types.

3.1 Definition of LiDAR Interference

LiDAR interference is the presence of multiple correlated signals during a LiDAR measurement. For dTOF LiDAR using SPADs, this results in multiple pulses obtained in a measured TCSPC histogram. In this work, the term interference excludes uncorrelated signals like continuous background light or internal noise by the DCR. In the following, two types of LiDAR interference are identified and underlying conditions for interference with regards to different severity levels are identified.

3.1.1 Types of Interference Between LiDAR Systems

Interference can occur in different LiDAR system constellations. It can be divided into two main types, which are illustrated in Figure 3.1. In this work, the interference is described from the perspective of an ego LiDAR system, which is affected by interference caused by one or multiple aggressor systems (agg). Direct interference

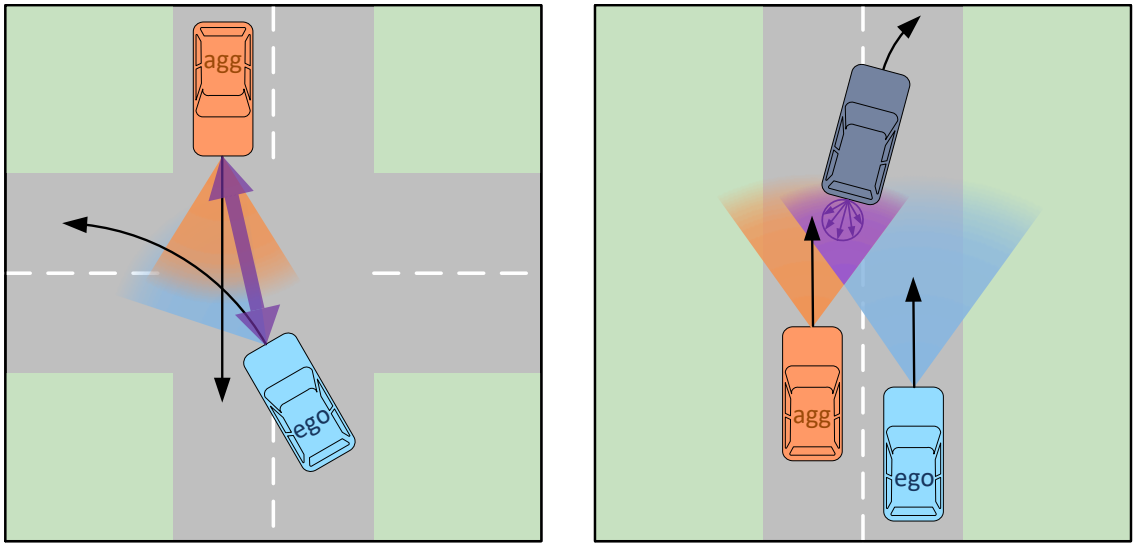

(a) Direct interference

(b) Indirect interference

Figure 3.1: LiDAR interference types shown exemplarily by two LiDAR systems used for autonomous driving potentially interfering with each other, which is marked in violet

is defined for the case that the aggressor system directly illuminates the ego system, whereas indirect interference is given for the ego and aggressor illumination of the same target. Therefore, the aggressor system can be also affected by interference, which is caused by the ego system. Especially laser pulses reflected by the same target might look equally in LiDAR measurements. In general, ego and aggressor system will have different laser emission times so that a common target will be seen with different TOFs in the ego LiDAR measurement. Although the aggressor system illuminates a real target, the corresponding TOF in the ego measurement will represent a phantom object with almost arbitrary target distance. The measurement of such a phantom target can have serious consequences, for example with regards to autonomous driving. The effects of direct and indirect interference are further classified throughout this work.

3.1.2 Conditions for Interference

LiDAR interference has different levels of severity as shown in Figure 3.2. There are different conditions, which must be fulfilled to match these different levels of LiDAR interference. To receive the total probability for LiDAR interference, all sin-

gle probabilities have to be combined. In the following, all conditions are described using the example of an ego system encountering a single aggressor system, but the conditions can equivalently be transferred to multiple aggressor systems.

The easiest case to define is no interference at all, which means the exclusion of every possibility that the ego system measures the laser light of an aggressor system. There are different methods to avoid interference, which can be adopted from the field of communication [68]. No interference is given if ego and aggressor system have no spectral overlap so that the aggressor laser wavelength does not match the bandpass filter width of the ego system. To simplify the considerations in this work, equal LiDAR systems of the same manufacturer are used for the investigations. Interference between equal LiDAR systems is a likely scenario because one or a few LiDAR manufacturers might dominate the market within one field of application so that often the same LiDAR systems are used. This assumption automatically fulfills the first listed condition of spectral overlap because equal systems have the same laser wavelengths and same bandpass filters. Concerning the second condition, ego and aggressor system can differ in their spatial orientation. If the aggressor FOI does not overlap with the ego FOV, aggressor light cannot directly reflect to the ego sensor. A third option avoiding interference is that ego and aggressor system have no temporal overlap. When both systems perform their LiDAR measurements at different times, the aggressor light will not be measured during the ego measurement. For this purpose, all possible aggressor back reflections should arrive at the ego system before it starts its measurement. Here, it must be considered, that the aggressor TOF can be longer than the measurement time although the aggressor would not measure its own signal then. However, for the ego system is only important, when the latest measurable aggressor back reflection will arrive.

If ego and aggressor system overlap in spectrum, space or time, interference can occur. Whereas these conditions are valid for all LiDAR methods, the differentiation of disturbing and non-disturbing interference depends on the measurement principle. As dTOF LiDAR accumulates repeated single-photon measurements, a single aggressor photon will have low impact on the total measurement. The decisive factor is whether ego and aggressor system have the same or multiples of the PRF so that repeated interference can occur. If there is no synchronicity, the interference is might be non-disturbing. Furthermore, when there is the repeated chance for the ego system to observe the aggressor illumination, the aggressor signal might

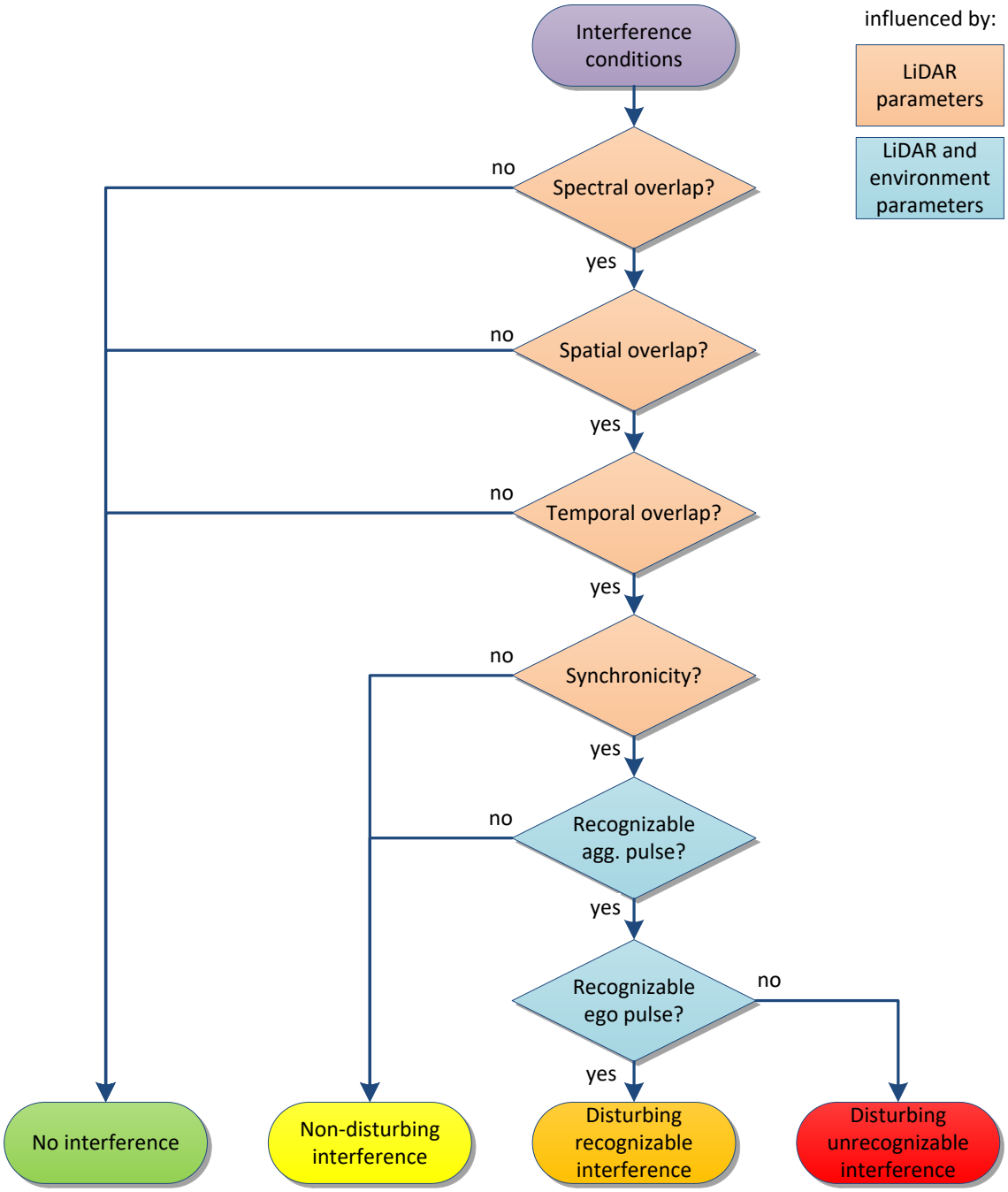

Figure 3.2: Conditions for four interference severity levels. The orange conditions are determined by LiDAR design parameters, whereas the blue conditions are additionally influenced by the environment like target and background light.

still be undetected, e.g. if the sensor is already saturated by the background light. Besides, interference can occur but does not have to be disturbing. This case of non-disturbing interference means for example that the appearing aggressor laser light behaves similar to background light from the view of the ego system.

The more critical case is disturbing interference, in which the aggressor pulse strongly appears in the ego LiDAR measurement. Then, the ego system may mistake this measured aggressor signal for a target. When the ego system recognizes the aggressor signal as well as the ego signal, it has the possibility to proof whether this is multi-target interference or which signal is the aggressor signal and which one the ego signal. This situation is classified as disturbing but recognizable interference. An even more dangerous case is the appearance of the aggressor pulse in the ego measurement, whereas the own ego pulse is unrecognizable. This can lead to disturbing unrecognizable interference so that the phantom object produced by the aggressor signal is mistaken for the real target indicated by the ego signal. The prevailing interference problem cannot be solved because this dangerous situation might not be recognized.

In this and the following chapters, the different interference conditions are further investigated. The condition of spectral overlap is probably given as discussed above. In the next sections of this chapter 3, the condition of spatial overlap is analyzed in section 3.2 as well as the condition of temporal overlap in section 3.3. In chapter 4, an interference test system is developed, which can also be used for general testing of LiDAR systems. The conditions for disturbing or recognizable interference are discussed in chapter 5. The statistical modeling of LiDAR histograms affected by interference and the synchronicity between ego and aggressor are considered in section 5.1. In section 6.2, a method for recognition of aggressor and ego pulse in the LiDAR histogram is developed and evaluated. Still unrecognized interference with potentially unrecognized ego pulse is analyzed in section 5.3. Finally, an interference suppression method to avoid synchronicity is presented in chapter 6.

3.2 Spatial Interference Probability

Besides the simple case of spectral overlap, the probability of occurrence depends on the spatial and temporal overlap as introduced in the previous section. These three conditions determine whether interference can occur or if interference is not

present at all. Therefore, the three conditions represent rough boundary conditions for the presence of interference, whereas the other conditions afterwards distinguish the different manifestations of interference. In this section, the occurrence of LiDAR interference with regards to the spatial conditions is analyzed. For direct and indirect interference, the arrangement of two LiDAR systems in relation to each other is different. Using the example of autonomous driving, vehicle constellations for both interference types are investigated with regards to overlapping LiDAR FOVs as shown in Figure 3.3. Under the condition of overlapping FOVs, the spatial distribution of the received interfering laser light on the different pixels of the LiDAR detector is measured and analyzed.

3.2.1 Minimum Distance of Spatial Overlap Enabling Interference

As presented in Figure 3.3 for a particular automotive scenario, interference is given for an overlap of the aggressor system's FOI with the ego system's FOV. For flash LiDAR systems, FOI and FOV can theoretically be the same. As seen in the Figure, direct interference can occur if two LiDAR systems move towards each other on neighboring lanes with parallel viewing direction so that their lateral distance a is one lane width. Possible median strips between these lanes are neglected but could be easily added to the later assumed lane width. When the LiDAR systems approach each other, the spatial overlap disappears for longitudinal distances smaller than $d_{\mathrm{min,direct}}$ to each other. For indirect interference, the systems are assumed on the same lane level without any longitudinal distance to each other moving in the same direction. Equivalently to direct interference, only large distances with regards to their viewing direction are relevant, which is their common target distance in this case. Starting from distance $d_{\mathrm{min,indirect}}$, there is an overlapping area, in which targets are illuminated by both LiDAR systems.

The minimum distance specifies, from which distance the FOVs overlap. For direct interference, the minimum distance is the distance between both LiDAR systems, whereas for indirect interference, the minimum distance represents the distance of the target, where the laser light of both LiDAR systems is reflected. The overlap of both FOVs depends on the horizontal FOV angle $\theta_{\mathrm{FOV,H}}$. Potential inter-

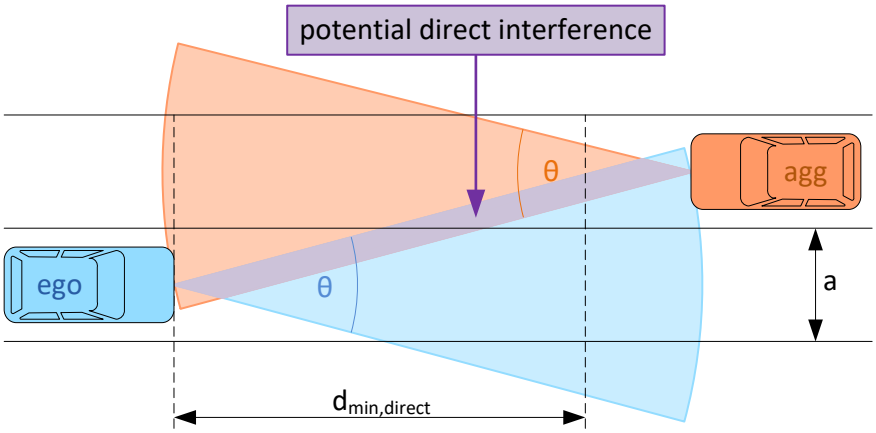

(a) Direct interference

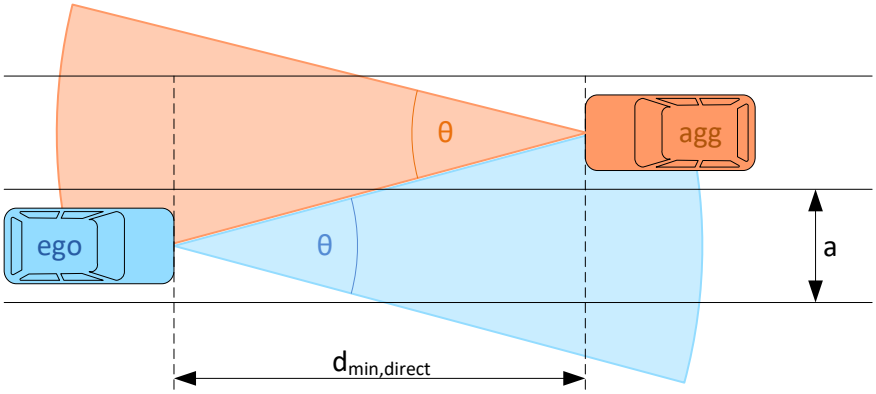

(b) Just no direct interference

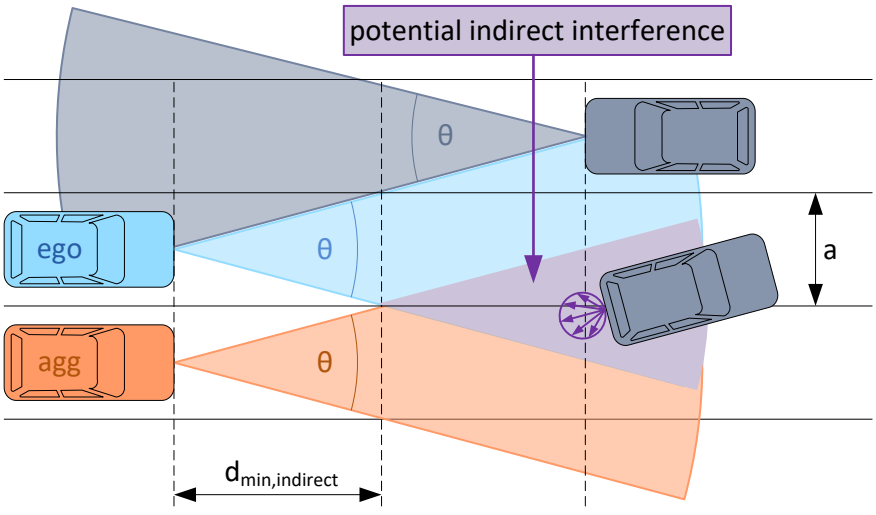

(c) Indirect interference

Figure 3.3: Automotive scenarios showing the spatial overlap starting from distance d_{min} for adjacent LiDAR systems with lateral distance a as one lane width to each other and horizontal FOV $\theta \equiv \theta_{\text{FOV,H}}$

ference occurs starting from the minimum distances $d_{\min}$ given by

$$d_{\min} = \begin{cases} \frac{a}{\tan\left(\frac{\theta}{2}\right)}, & \text{direct interference} \\ \frac{a}{2\tan\left(\frac{\theta}{2}\right)}, & \text{indirect interference} \end{cases}. \tag{3.1}$$

As example application, autonomous driving on a German motorway with a lane width of 3.25 m is chosen [69]. Assuming a single LiDAR system each at the front of a vehicle on a motorway lane, the lateral distance a between those systems is determined for one to three lane widths. The minimum target distances for interference caused by overlapping horizontal FOVs are shown in Figure 3.4. Two continuous bands are seen, which represent direct and indirect interference. The minimum distances are continuously given because a vehicle is not necessarily located in the center of the lane but can vary slightly or even change the lane. Therefore, the resulting minimum distances are drawn as continuous band from one lane width illustrated by the solid lines to three lane widths given by the dashed lines. The geometric analysis shows that direct interference starts from twice the distance than the distance to an interfering target due to indirect interference, which is also seen in (3.1). Therefore, the minimum distances of indirect interference are considered in more detail in the following. For a small horizontal FOV like 1°, indirect interference begins for targets at about 200 m distance for two vehicles on neighboring lanes. If there are more lanes between the vehicles, this minimum interference distance becomes even higher. Thus, such a small FOV has few problems with interference. For a moderate FOV of 10°, the minimum target distance for simultaneous illumination begins at 20 m to 100 m depending on the interference type and the vehicle's distance to each other. This is problematic for LiDAR systems that are designed to cover ranges up to 250 m. Even more critical are large FOVs like 50° to 100° so that every minimum distance is below 10 m for indirect interference.

For equal or higher distances, the spatial condition for the occurrence of interference between both systems is fulfilled. On German motorways, a typical target distance is given by the safety distance to the vehicle ahead. This safety distance given in meters must be larger than half of the speedometer value given in km/h[1] according to the German catalog of fines *BT-KAT-OWI* [70]. For example, a velocity of 120 km/h requires a safety distance of 60 m. At such distances higher than 60 m,

[1]It should be noted that there is currently no general speed limit on German motorways. While uncommon, maximum speeds of 250 km/h − 300 km/h are possible.

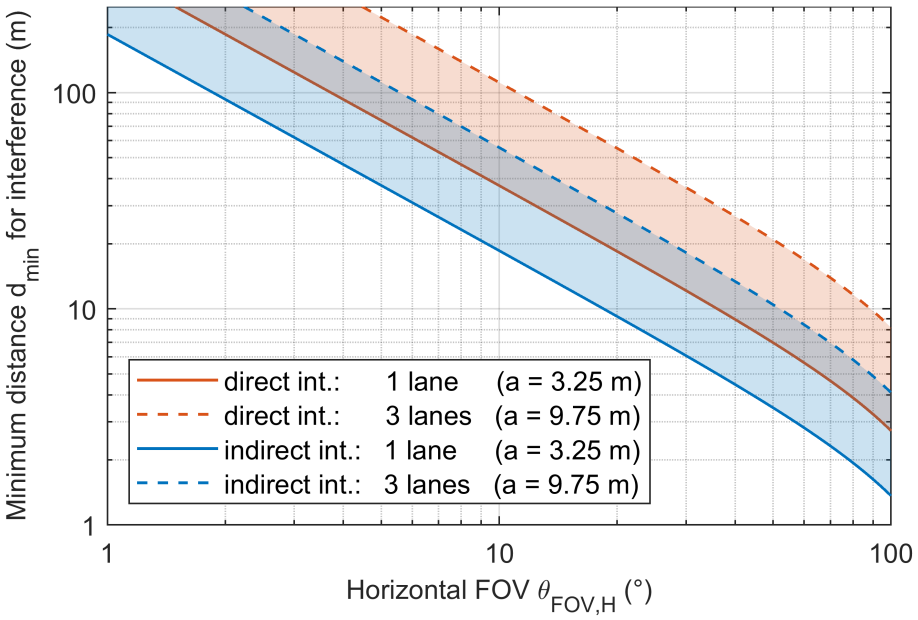

Figure 3.4: Minimum vehicle distance $d_{\text{min,direct}}$ for direct interference and minimum target distance $d_{\text{min,indirect}}$ for indirect interference for one to three motorway lane widths a

potential direct or indirect interference is given for FOVs larger than 11° with three lanes distance between the LiDAR systems. For only one lane, direct or indirect interference at the same distance of 60 m already starts from a FOV of 6° or even 3°. This simple application of LiDAR systems on motorway lanes shows that interference is possible for many constellations of LiDAR systems or targets. As spatial overlap is even probable for this well-defined scenario, more complex environments like intersections can provide more variations for spatial overlap. Finally, many uncontrolled environments with multiple LiDAR systems will show the potential for spatial overlap and hence LiDAR interference. The question remains, how this spatial overlap is imaged on the LiDAR detector, for example how many pixels can be affected by interference.

3.2.2 Measurement of Spatial Interference Distribution on the LiDAR Detector

In this section, the spatial overlap with regards to the affected pixels of the LiDAR detector is discussed. Two LiDAR systems *Owl* as introduced in section 2.1.4 are used to demonstrate the measurement of direct and indirect interference as shown

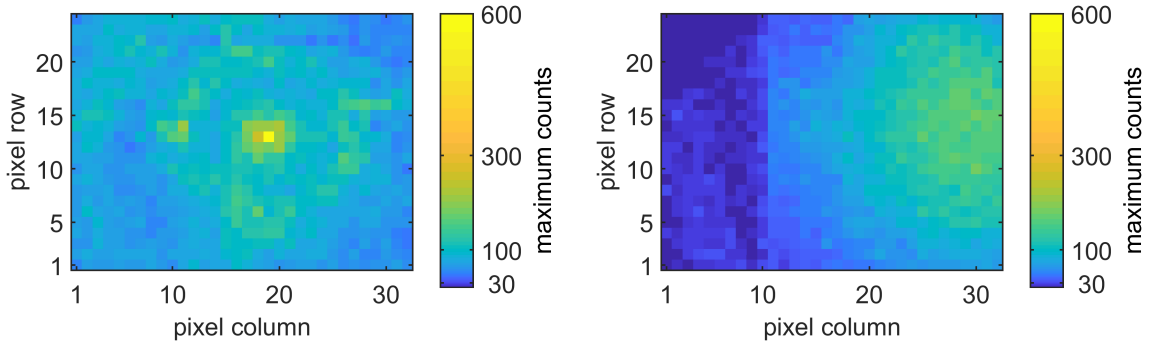

(a) Direct LiDAR Interference

(b) Indirect LiDAR Interference

Figure 3.5: Spatial interference distribution on the LiDAR detector by example intensity measurements for the two LiDAR interference types measured by LiDAR system *Owl*

in Figure 3.5. For the detection of the interfering light, the self-emitted laser light of the ego system is switched off. In the Figure, the color indicates the number of arriving photons from each direction. For each pixel, a LiDAR histogram has been accumulated from 1000 photon detections. In the histograms, signatures of the detected aggressor pulses have been detected with different heights. To compare their peak intensities, the highest histogram count value is extracted for each pixel. These maximum counts at the different pixel columns and pixel rows are seen in Figure 3.5 and show the spatial distribution of the obtained laser light received from the aggressor LiDAR system. The brightest color corresponds to the highest aggressor photon rates, whereas pixels with a dark color probably contain no laser light but only low background light.

For direct interference, the two LiDAR systems are positioned in front of each other. The resulting intensity map in Figure 3.5 shows a very high intensity in one pixel, whereas the neighboring pixels already show an intensity not even half as high. All other intensities are at about 5 % of the maximum intensity. There are some circular structures with low intensity around this pixel. If the aggressor laser points to the ego system, the aggressor laser source area is imaged on the ego sensor. As laser sources have typical diameters of a few micrometers, the total source area fits into a single detector pixel. Depending on the details of the imaging optics, the interference is expected to lie within one pixel or maximally within four pixels of the ego LiDAR detector if the source area is imaged exactly on the edges

between the pixels. As expected, the main intensity is measured in one pixel. The low intensities in the neighboring pixels and the larger circular structures might be caused by unwanted multipath reflections within the receiving optics of the ego systems. Although the optics are designed for the highest possible light-transparency, a little light amount can be reflected at the lenses of the optics, which is detectable for single-photon detectors like SPADs. This light can be reflected to other pixels than intended. However, the main pixel affected by direct interference shows a much higher intensity indicating a strong influence of direct interference, whereas all other pixels seems to be almost unaffected.

For the demonstration of indirect interference, two LiDAR systems *Owl* are positioned next to each other in front of the same flat target. The pixels on the right hand-side show moderate intensities at about 100 to 200 maximum counts, which are the brightest at about pixel column 30 and pixel row 15, whereas most pixels of the first ten columns contain less than 30 maximum counts. It can be seen that the illumination of the aggressor system has been centered on the target area observed by the right half of the ego FOV. Therefore, the left part of the sensor up to pixel column 10 is not affected by the indirect interference. The measured intensity distribution within the aggressor light has a brighter center because the radially emitting laser light is projected on a flat target. Edge pixels observe higher target distances of flat targets than central pixels so that the optical laser power is reduced more by the inverse square law [71]. This is given for the aggressor and ego LiDAR system in the same way. Only the position of the illumination center of both systems might differ, depending on the positions relative to the target and to each other. With increasing spatial overlap of the FOIs on the target, more pixels of the ego system are affected by the indirect interference. Compared to direct interference affecting only one to four pixels, indirect interference can influence a large number of pixels or even all pixels of a LiDAR system. This represents a higher risk because direct interference provides the possibility to recognize or compensate interference effects by the comparison of the affected pixel with the measurement data of neighboring pixels, whereas indirect interference does not provide such a possibility. The result of the spatial interference analysis is that LiDAR FOVs can overlap because uncontrolled environments have only little or no influence on the positions and FOV orientations of the present LiDAR systems. Moreover, indirect interference might affect many pixels of the ego detector, which complicates interference recognition by the spatial

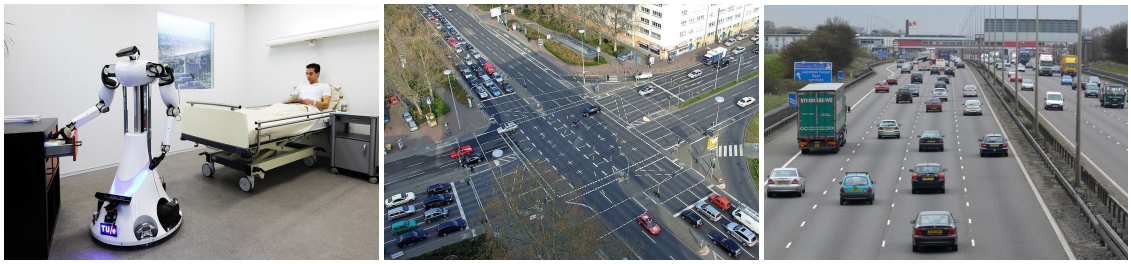

(a) Robot (b) Intersection (c) Motorway

Figure 3.6: Use case scenarios for the analysis of temporal overlap between measurements of different LiDAR systems (pictures taken from [72][73][74])

correlation of pixels as it can be performed for direct interference. Therefore, this work will focus more on indirect interference. Instead of spatial parameters, the temporal parameters of a LiDAR system might provide a higher potential for low interference probabilities.

3.3 Temporal Interference Probability

Spectral and spatial overlap will still not necessarily lead to interference. When spectral and spatial overlap are given, another significant condition for the occurrence of interference is the temporal overlap of the LiDAR measurements of these systems, which is determined for a single pixel as follows.

3.3.1 Use Case Scenarios

The requirements for LiDAR systems vary with the application and result in different temporal behavior. As discussed in section 2.4, the potential number of aggressor systems also depends on the application. For the analysis of temporal overlap, three use case scenarios from the field of transport with different parameters are defined. The scenarios are illustrated in Figure 3.6. The first scenario are mobile robots using simultaneous localization and mapping (SLAM), the second scenario is an intersection with autonomous vehicles and the third scenario is a motorway with autonomous vehicles as well. The parameters are listed in Table 3.1.

In the first use case, the mobile robot has probably no fixed lanes and can choose free paths. For the robot, a low range up to 10 m can be sufficient because it can

Table 3.1: LiDAR parameters of use case scenarios

Use Case	Robot	Intersection	Motorway
LiDAR type	High Speed	Short Range	Long Range
Frame rate	1000 fps	100 fps	10 fps
Range	10 m	50 m	250 m
Number of potential aggressors	10	5	3

move slowly and requires a very precise location of itself in the self-created map. For such a short range of 10 m, a high-speed LiDAR system can be applied, e.g. with a high frame rate of 1000 fps [75]. Especially for high-speed LiDAR, higher target distances can be problematic because they produce more data requiring more storage and can lead to an ambiguous range detection of the measured target distances. For all scenarios, it is assumed that 1000 laser pulses are emitted per frame so that 1000 measurements are accumulated for each frame. This is explained in more detail in chapter 5. With a frame rate of 1000 fps and 1000 pulses per frame, the laser PRF thus is 1 MHz, which is high but possible to be realized for flash LiDAR [31][32][33]. For a target distance of 10 m, the corresponding measurement time can be calculated by (2.1) to about 67 ns. During this measurement time, the ego system is sensitive to interfering light emitted by an aggressor system. However, the time window for present aggressor laser light can be larger than the measurement time, e.g. by multipath reflections. Of course, the aggressor system will not measure the self-emitted light if it is reflected back to the aggressor system after the measurement time stopped. Nevertheless, the ego system could have started its measurement later than the aggressor system and hence can still measure the present aggressor light. Apart from these exceptional cases, the time of a present laser signal is equivalent to the measurement time, which is assumed in the following analysis of the temporal overlap as well. Within the range of 10 m, 10 robots with aggressor LiDAR systems are assumed.

The second use case treats autonomous driving on an intersection. The required range on German urban roads is defined by the minimum stopping sight distance in the standard *Directives for the Design of Urban Roads* [76]. This distance must be large enough that a driver can stop in front of a hazard even on a wet road [69]. The stopping sight distance is given by the addition of driving distances due to the

driver's reaction time as well as the vehicle's response time and the breaking distance. For urban roads with a longitudinal gradient of 0 %, vehicles with 50 km/h require a stopping sight distance of about 50 m [76]. The potential measurement range of the LiDAR system can be higher, but the urban autonomous driving only needs to utilize this measurement range up to 50 m. The frame rate can be chosen moderately to 100 fps. On an intersection, vehicles can arrive from different directions. An opposite vehicle will produce direct interference, whereas vehicles of the same direction on neighboring lanes can illuminate this opposite aggressor system producing indirect interference. Thus, both interference types can occur in the ego measurement of one pixel at the same time. Additionally, vehicles from the crossing road to the left or right of the ego system can also cause direct or indirect interference if the FOV is large enough. In this case, five aggressor LiDAR systems are assumed on the intersection.

For the third use case, autonomous driving on a German motorway is chosen. In this case, long ranges must be covered to detect more distant targets while the autonomous vehicle has a high velocity reducing the available reaction time. The requirements for German motorways are described in the standard *Guidelines for the Design of Motorways* [69]. For motorways without speed limit, the minimum stopping sight distance for velocities of 130 km/h is used, which is about 250 m for a longitudinal road gradient of 0° [69]. This range makes it impossible to apply high frame rates like those of high-speed LiDAR due to the ambiguous range of target distances. In general, a lower frame rate than those of the other scenarios is required because motorways have a lower variety of different situations and there is a small number of selectable lanes or general actions by the autonomous vehicle making the action choice easier. Here, 10 fps are chosen. Due to the median strip separating the oncoming traffic, indirect interference by vehicles on neighboring lanes will be predominately. Assuming a full motorway with three lanes and an additional motorway ramp, three aggressor LiDAR systems are assumed.

3.3.2 Theoretical Maximum Number of Aggressor Systems

For each use case, an example number of potential aggressor systems was estimated in the last section. Another approach is the conservative estimation of the theoretical maximum number of potential aggressor systems that can produce interference in one pixel of the ego system at the same time. This maximum number of aggressor

systems can be compared to the estimated number of aggressor systems and might provide limitations to possible interference scenarios. For both interference types, the maximum number of aggressors depends on the dimensions of the vehicle on that the LiDAR systems are fixed. In the use cases, main LiDAR users strongly affected by interference are cars with autonomous driving and robots. The average car width is $w_{\mathrm{car}} = 178\,\mathrm{cm}$ [77], whereas an example robot width is $w_{\mathrm{robot}} = 55\,\mathrm{cm}$ [78]. The constellations with maximum number of aggressors are shown in Figure 3.7. It is assumed that each LiDAR system is mounted centrally at the front of the vehicle at the level of the bumper. As the chosen applications of car and robot often use LiDAR systems with focus on the horizontal FOV, only horizontally arranged vehicles are considered now and not the vehicle heights. For direct interference, the ego system observes the aggressor systems with a width of the vehicle width. For indirect interference, all LiDAR systems are assumed to illuminate a target at the same height as those of the LiDAR systems so that a two-dimensional geometrical analysis is performed.

For direct interference, there is a maximum number of aggressor systems seen within the ego system FOV. Only for large pixel FOVs observing more than one vehicle, direct interference of multiple aggressor systems can be measured at once. For short-range applications, a large pixel FOV of 1° can be assumed [79]. One pixel of a robot LiDAR system with such a FOV will observe a total robot with the assumed width $w_{\mathrm{robot}} = 55\,\mathrm{cm}$ in a distance of 32 m. Only for larger distances, more than robot is seen by this single pixel, e.g. twice the distance will allow to observe two robots. For autonomous short-range LiDAR systems, a car will be seen in 102 m distance, which would rather be considered as long-range distance. Long-range LiDAR uses smaller pixel FOVs like 0.1° [79]. A pixel with this FOV observes a total car in a distance of over 1000 m. Both use cases show that such applications are unlikely to be affected by direct interference of multiple aggressor systems within one pixel. Instead, different aggressor systems are probably imaged on different pixels of the ego system. In conclusion, direct interference by multiple robots is possible, but the total number of direct interferers will be small.

For indirect interference, it must be analyzed how many aggressor systems can illuminate the same target point that is observed by a specific pixel of the ego system as well. On each vehicle, one potentially interfering LiDAR system is assumed. Although there could be more than one LiDAR system on a vehicle, the FOIs of

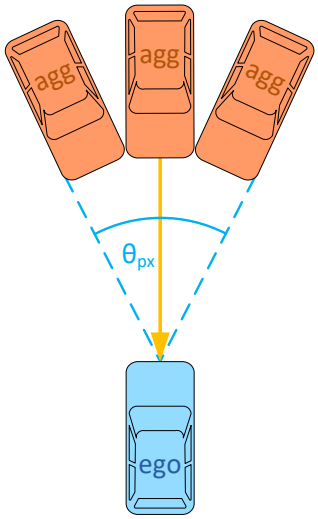

(a) Direct interferences are likely imaged on multiple pixels with FOV θ_{px} so that they probably not sum up in the LiDAR measurement of a single pixel

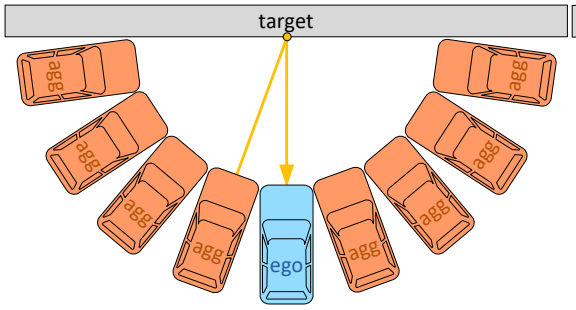

(b) Indirect interference with same target distances

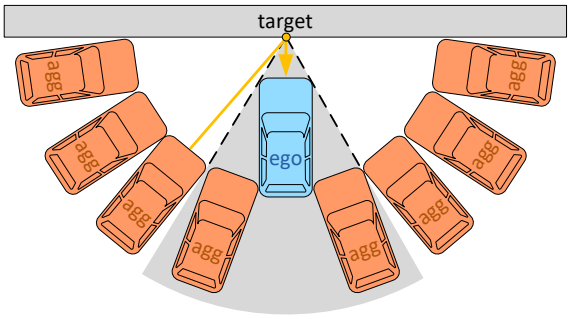

(c) Indirect interference with shorter target distance of ego system than of aggressor systems

Figure 3.7: Constellations for the maximum number of aggressor systems that can produce interference at the same time at the same pixel of the ego system.

several systems should be discontinuous due to eye safety so that only a single LiDAR system per vehicle can illuminate a certain target. The number of drawn aggressor systems in Figure 3.7 depends on the distance from the aggressor systems to the ego system with regards to direct interference and to the target with regards to indirect interference. For indirect interference, the position of the ego systems in relation to the aggressor systems is also relevant. The easiest case is indirect interference with equal target distances from ego system and aggressor systems as seen in Figure 3.7b. The maximum target distance of the ego system to the target

is given by the range of this LiDAR system. Due to the assumption of equal LiDAR systems, the same maximum target distance is valid for the aggressor systems. In combination, the same range is valid if the aggressor system emits a laser pulse to the target and the ego system detects it because the traveled light distance is the same as if the ego system had emit and detect the laser light. The LiDAR ranges of the use cases are 10 m for robots and 50 m or 100 m for autonomous cars.

From the view of the target, the covered angle by an aggressor system θ_{agg} on a vehicle with width w is given by

$$\theta_{\text{agg}} = 2 \arctan\left(\frac{w}{2d_{\text{max}}}\right), \tag{3.2}$$

where d_{max} is the range of the LiDAR systems. Thus, the maximum number of aggressor LiDAR systems n_{agg} within a horizontal pixel FOV θ_{px} for a point target observed by a single pixel becomes rounded up to

$$n_{\text{agg}} = \left\lceil \frac{180° - \theta_{\text{ego}}}{\theta_{\text{agg}}} \right\rceil, \tag{3.3}$$

where θ_{ego} is the angle occupied by the ego LiDAR system's vehicle within the hemisphere and w is the vehicle width, which is either the car or robot width as defined before. If ego and aggressor vehicle have the same distance to the target, the covered ego LiDAR angle is the same as the aggressor covering angle with $\theta_{\text{ego}} = \theta_{\text{agg}}$. The resulting maximum numbers of aggressors are shown in Table 3.2. For the robot, the maximum number of aggressors is 57, whereas cars with 50 m range allow maximally 88 aggressors and cars with 250 m allow 441 aggressors. In the case of robots, the maximum number of aggressors can depend on the environment structures, e.g. indoor applications with small floors, which also can spatially separate the robots from each other. For autonomous driving, urban environment structures can also provide limitations for the maximum number of aggressors.

In the other example of indirect interference in Figure 3.7c, the ego system is located closer to the target, which shortens the light path. As result, the aggressor systems could be positioned more distant to the target, which would allow even more aggressor systems than before. At the same time, there is less room for aggressor LiDAR systems due to the larger ego coverage angle

$$\theta_{\text{ego,short}} = 2 \arctan\left(\frac{w}{2d_{\text{ego}}}\right). \tag{3.4}$$

Table 3.2: Maximum number of aggressor systems for indirect interference as shown in Figure 3.7b and 3.7c

Scenario	Range $d_{\max}$ (m)	Maximum number of aggressor systems	
		Same target distances at range $d_{\max}$	Short ego target distance $d_{\text{ego,short}} = 1\,\text{m}$
Robot	10	57	48
Intersection	50	88	48
Motorway	250	441	237

For a target distance $d_{\text{ego}} = 1\,\text{m}$, this coverage angle reduces the maximum number of aggressor systems only slightly as seen in Table 3.2. The maximum number of aggressors in the case of the robot is reduced by nine systems. For the car, the aggressor systems are almost reduced by half, but the absolute numbers of 48 or 237 aggressor systems are still very high. Larger distances from the aggressor systems to the target would just further enlarge this maximum number of aggressor systems.

The derived maximum number of aggressors for robots and autonomous vehicles is very high. The resulting number of aggressor systems is much higher than the estimated number of aggressor systems of the use cases. Thus, the maximum number of aggressors produces no additional restriction to the estimated number of aggressors. Therefore, the realistically chosen number of aggressors from the uses cases are considered in the following. In the future, different LiDAR applications might arise, where a higher number of aggressors can be imagined. For example a high number of LiDAR systems at the same location can be given if every pedestrian wears a LiDAR system or if even smaller bee drones are equipped with LiDAR systems. Furthermore, drones moving in 3D space can also be affected by aggressors in the vertical dimension. 3D constellations can also be given for vehicles moving on the ground but observing targets that are higher than the vehicles so that vehicles behind each other can illuminate the same target and interfere with each other. For a specific application, the possible maximum number of potential aggressors can be determined more appropriately if the available space in horizontal and if applicable vertical dimension of this application is considered, including environment limitations like walls reducing this space.

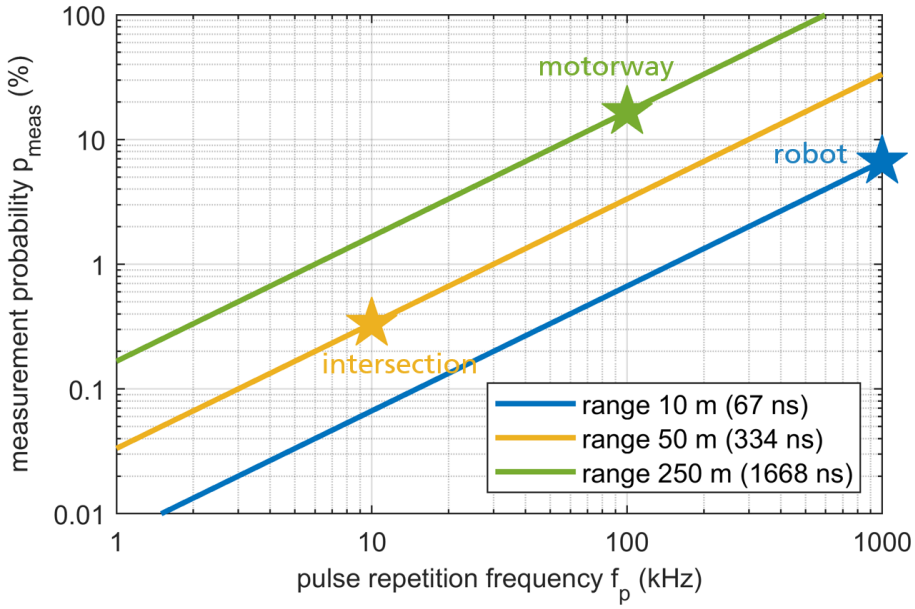

Figure 3.8: Probability that a LiDAR system performs a measurement at a specific time given by the sensor duty cycle, depending on maximum range or rather histogram length and the laser repetition rate. For each frame, 1000 laser pulses are emitted to create a histogram from 1000 first-photon measurements.

3.3.3 Sensor Duty Cycle of One LiDAR System

LiDAR system interference occurs only if the aggressor system emits a laser pulse while the ego system performs a measurement. The probability to measure at a specific time is determined by the sensor duty cycle, which is the proportion of the photon measurement time to the time between to emitted laser pulses. The required measurement time must be large enough to emit a laser pulse and receive its reflection from targets at the maximum distance. Therefore, the measurement time of a LiDAR system corresponds to the range by (2.1). The measurement time is equivalent to the histogram length t_{hist} and the time between two consecutive laser pulses is given by the reciprocal of the pulse repetition rate f_{p}. From these values, the sensor duty cycle can be determined, which indicates the probability p_{meas} that a system is currently conducting a measurement at an arbitrary point of time given by

$$p_{\text{meas}} = t_{\text{hist}} \cdot f_{\text{p}}. \tag{3.5}$$

The resulting probabilities are shown in Figure 3.8. The robot has a probability of 6.7 % to conduct a measurement at a specific time. In contrast, the autonomous

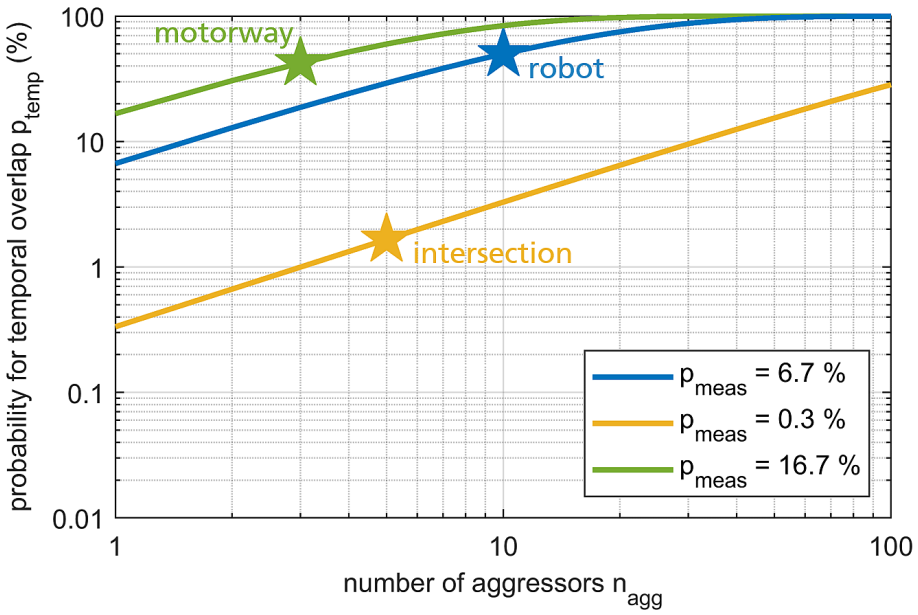

Figure 3.9: Probability for temporal overlap between the ego system and any of the present aggressor systems based on the measurement probabilities of the three use case scenarios shown in Figure 3.8

vehicle on the intersection has a small sensor duty cycle of only 0.3 % because the PRF is lower. The autonomous vehicle on the motorway has the highest measurement probability with 16.7 %, which is caused by the long measurement times due to the large measurement range of 250 m. As the PRF often directly correlates with the number of measurements per frame, it must be considered that an increased number of measurements can require a higher PRF or otherwise leads to a decreased frame rate, which could be crucial for the respective application.

3.3.4 Temporal Overlap of Multiple LiDAR Systems

Combining the sensor duty cycle as probability to conduct a measurement p_{meas} at a specific time and the number of aggressors n_{agg}, the final temporal overlap probability per pixel becomes

$$p_{\text{temp}} = 1 - (1 - p_{\text{meas}})^{n_{\text{agg}}}. \tag{3.6}$$

This is the probability for a minimum of one aggressor laser pulse arriving during the measurement of the ego system. The resulting probability values are seen in Figure 3.9. For the use case of the robot, this probability is very high with 49.9 %,

which is mainly caused by the high number of potential aggressor systems. The motorway use case also has a high probability of temporal overlap with 42.2 %, but this is caused by the long measurement time corresponding to the high range, whereas the number of aggressor systems is small. The lowest probability for a simultaneous measurement between the ego and any aggressor system is 1.7 % for intersections, which combines a moderate measurement time with a moderate number of aggressor systems. In the standard *Road vehicles – Functional safety*, hardware failure rates have to be less than $10^{-7}\,\mathrm{h}^{-1}$ for all possible safety levels [80, 81]. Alternatively, the failure rate for human drivers can be determined, which is about 10^{-10} failures per driving kilometer [82]. Compared to these orders of failure rates, the probability for temporal overlap is very high for all drawn scenarios. However, it must be considered that this is solely the temporal condition of LiDAR interference, which must be combined with all other condition probabilities presented in section 3.1.2. Only the total interference probability should be compared to the allowed functional safety standards to evaluate if the total interference probability is high or not. Later in chapter 6, interference suppression methods are described, which can reduce the total interference probability.

Chapter 4

Interference Test System

If the interference conditions of spectral, spatial and temporal overlap are met, interference can occur in the LiDAR measurements. To analyze affected LiDAR measurements, a test setup is developed. To produce the worst case of interference between two LiDAR systems, their measurement times must be synchronous to guarantee their temporal overlap and hence facilitate the occurrence of interference. Additionally, different scenarios should be tested, i.e. different values for the TOF and the intensities of laser and background light. Besides LiDAR interference, general LiDAR testing is crucial for applications like autonomous driving. To the best of my knowledge, such a test system under laboratory conditions is currently not available. Therefore, the concept of an LiDAR target simulator (LTS) is developed in this chapter as a new general LiDAR testing method for a laboratory environment. The LTS is designed with particular focus on autonomous driving representing LiDAR applications with critical timing requirements. At the end of this chapter, a first experimental realization of the LTS is demonstrated.

4.1 Current State of LiDAR System Tests

In the future, the number of vehicles with advanced driver assistance systems (ADAS) might grow and the ADAS level is expected to reach level 5, which refers to fully autonomous driving [83, 84]. Autonomous driving is based on different sensors like cameras, radar, LiDAR or ultrasound. To guarantee the driver's safety, these sensors require standardized reliable tests, which can be performed at different states of the sensor development. A typical product development applied to automotive

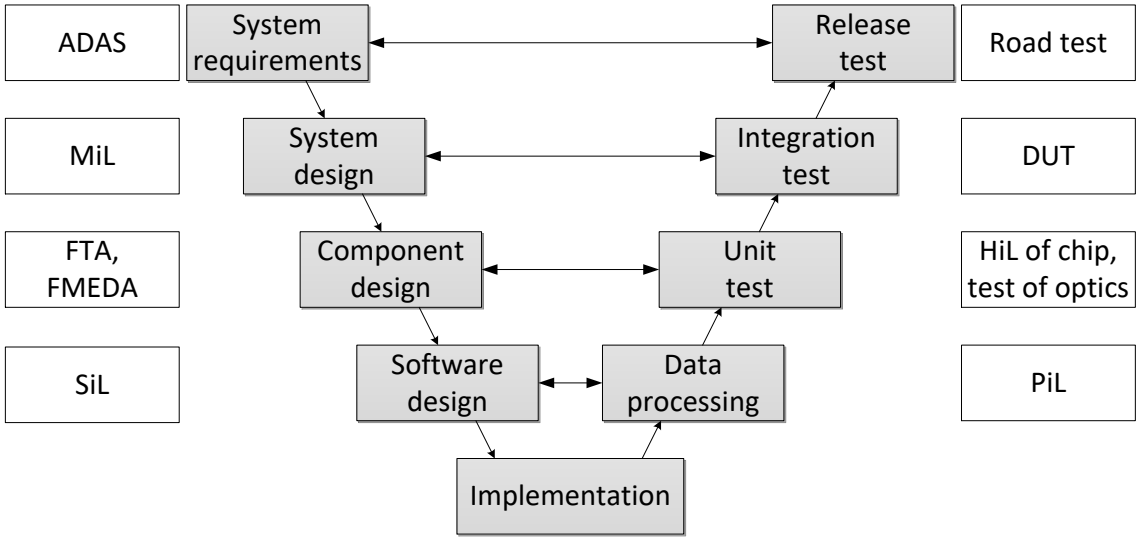

Figure 4.1: Integration test of V-model realizable by target simulator with device-under-test (DUT) [40]

elements is described by the V-model shown in Figure 4.1. At first, the system requirements are defined depending on the intended ADAS. For example, a LiDAR system should be able to perform distance measurements of targets with defined distance and reflectance in the presence of bright sunlight. Based on these requirements, the system is designed. For the mentioned example of bright sunlight, active background light suppression as described in section 6.3 might be part of the LiDAR system to suppress the sunlight. The system functionality can be tested with the help of a model-in-the-loop (MiL), where the LiDAR system is modeled within an environment simulation. For example, the environmental simulation physically models the expected background-generated event rates at the LiDAR system from bright sunlight reflected at different targets with defined distance and reflectance. For each scenario, optimal background suppression parameters can be set so that it is evaluated if the sunlight suppression works for all scenarios and can be adjusted precisely enough. For the safety of the entire system, the single components are designed with regards to their interaction by methods like fault tree analysis (FTA) or failure modes effects and diagnostic analysis (FMEDA). As a result, additional components or controlling mechanism might be required to increase the functional safety, e.g. a warning can be given in the unexpected case that the sunlight is brighter than the background suppression method can handle. From the determined system and component design, the actual code is created and optimized on the basis of software-

in-the-loop (SiL), which tests the compiled code again with regards to functionality but also individual requirements like execution time or memory allocation. At the end, the implementation of all parts into the overall system is performed. After that, all design steps are tested with corresponding testing steps in reversed order. First, the code is executed on the target processor as processor-in-the-loop (PiL), e.g. to identify compilation errors. If the code runs correctly, separate unit tests can be performed, e.g. a hardware-in-the-loop (HiL) of the chip or a test of the optics. For example, the test of the chip might identify hot pixels, which always indicate too bright sunlight, although most triggered events might be electrically induced. As a result, the chip might be replaced by another one or these pixels might be switched-off to avoid permanent warnings. After the test of the single components, the integration test can analyze the DUT, which is the complete LiDAR system in this case. For this purpose, the environment is simulated with analogue signals, e.g. a suitable light source can represent artificial sunlight. Finally, road tests prove the functionality of the overall vehicle including the LiDAR system. For example, the performance of the LiDAR system can be tested under real sunlight conditions.

For the modern technology LiDAR, there are still no common standards or testing strategies. Often, general testing standards of the automotive industry are applied. For example, some LiDAR manufacturers certificate their processes by the norm ISO 26262 that includes functional safety methods like FTA or FMEDA [80]. Besides, custom LiDAR testing solutions are developed. There are LiDAR software testing solutions like SensorSim from dSpace [85] or CarMaker from IPG Automotive [86]. The optics of LiDAR systems can be tested as single components by DIOPTIC [87]. Simple LiDAR system tests with short distances can be performed in the laboratory using targets with defined reflectance [88]. For road tests, driving areas are offered [89]. In the near future, there will be huge a need for comprehensive integration tests in the automotive industry testing the complete LiDAR system in laboratories. LiDAR systems are going to be a standard feature in series vehicles with autonomous driving. Since 2017, the first LiDAR system is integrated in a series vehicle with autonomous level 3 [90]. However, tests for a complete LiDAR system with regards to strict automotive requirements are still not yet available. There are only final road tests using the complete LiDAR system, but they strongly depend on the appearing road scenarios and hence are not reproducible. For example, road test scenarios are defined by daytime, weather like the current solar radiation and

environment like buildings or flora. Furthermore, testing rare scenarios requires a huge number of driving hours to achieve the desired confidence level. In contrast, the suggested LTS represents a suitable integration test under laboratory conditions providing not only reproducible scenarios but also a time and cost efficient testing solution. The LTS can validate the complete LiDAR system with regards to the interaction of all single components, which have been tested before in separate unit tests. Dangerous scenarios like accidents can be tested without any risk and waste of material.

4.2 LTS Setup

The main principle of the LTS is shown in Figure 4.2, where the LTS is the orange screen in front of a vehicle with a LiDAR system at the front. Unlike HiL with hardware connection to the LiDAR system, the LTS screen receives the emitted light of the LiDAR system over-the-air (OTA). The LTS provides a virtual scenario, where targets with defined reflectance and distance can be included. These scenarios can be either simulated in advance or in real-time to determine the properties of the light after the target reflection. The target reflection can be emulated for multiple light sources illuminating the target, for example the ego laser pulse (ego), aggressor laser pulse (agg) and background light (bg). To achieve the desired TOF in the histogram for the ego or aggressor signal, the signal received from the LiDAR system is delayed. Additionally, the optical power of the light emitted by the different light sources and reflected by the target can be determined according to the virtual target. The LTS screen emulates the different scenarios by emitting light back to the LiDAR system. Thus, the LTS itself can work electrically independent of the DUT, which requires neither system intervention nor data sheet information. There are two patents within this research field [93][94]. However, only a few manufacturers indicate that first ideas concerning this innovation might be under development [95][96]. A first basic test system has been realized by the manufacturer HORIBA testing only the basic LiDAR functionality [97]. The focus of this test system is rather on the implementation of the LiDAR system into the whole vehicle, which is tested by a HiL system. Some researcher groups developed concepts for long-range LiDAR systems, which are useful for military purpose with ranges up to 2.5 km but not automotive scales [98][99]. Currently, there are some research projects like

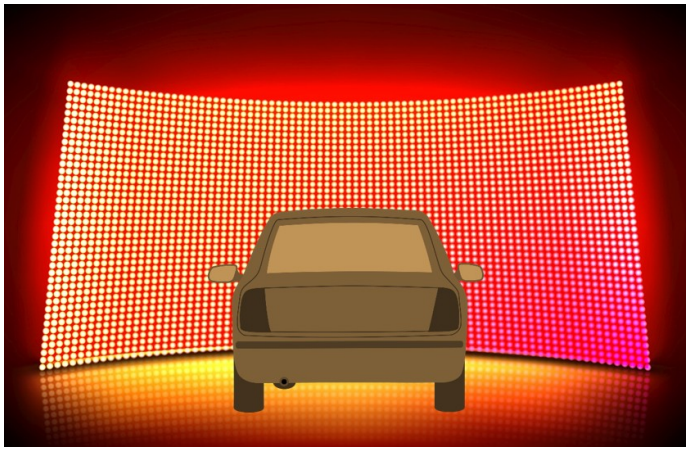

(a) Illustration of vehicle with LiDAR system in front of an LTS screen observing the emulated target reflections emitted by the LTS sources (pictures are taken from [91][92])

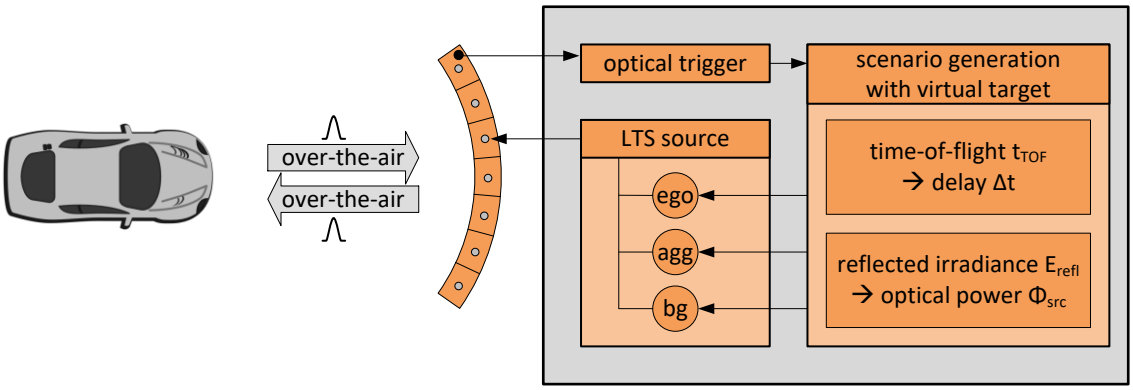

(b) Working principle

Figure 4.2: A LiDAR system on a vehicle emits a laser pulse towards the LTS screen. The LTS detects the laser pulse from the LiDAR system with an optical trigger and generates the virtual scenario for each LTS source with regards to the ego reflection (ego), aggressor reflection (agg) and background reflection (bg). Each LTS source on the screen combines these light signals and emits the resulting signal to the LiDAR system at the vehicle [40].

"SafeMove" and the follow-up project "Vivaldi" mainly concerned with radar and camera testing but expanding their scope to LiDAR implementations as well [100].

For automotive applications, stricter requirements must be fulfilled than for other applications like long-range LiDAR with distances up to 2.5 km, which are equivalent to a TOF of 17 µs according to (2.1). In contrast, the traffic in cities mainly requires measurement ranges up to 50 m corresponding to time measurements up to 0.3 µs. The distance resolution can be in the order of centimeters leading to high-precision timescales in the order of picoseconds. Besides timing, standard testing of LiDAR systems in vehicles must be fast and efficient so that modifications at each vehicle or LiDAR system should be avoided. Instead of a hardware connection between LiDAR system and LTS, OTA testing only requires the exchange and positioning of the DUT. Then, the LTS receives the LiDAR laser pulse and emits the emulated LiDAR reflections always in the same manner. On the other hand, the OTA signal transfer implies the risk of undesired multipath reflections. Although there is a patent describing a flat screen with multiple optical triggers to receive LiDAR signals OTA, there is no discussion about the problematic multipath reflections [94]. A possible solution is developed in this work and will be presented later.

The LTS is not limited to automotive applications. An appropriate design allows the testing of various LiDAR methods like dTOF, iTOF and FMCW LiDAR as described in section 2.1.1. Besides flash LiDAR, the adaption to scanning LiDAR systems is possible. The testing scenarios can be chosen with regards to the challenges of each DUT and the desired application. The LiDAR system can be tested individually as an end-of-line (EOL) test or already integrated in a vehicle, which is placed in front of the LTS. In case of several LiDAR systems mounted on the vehicle enabling a 360° view, identical LTS systems can be positioned in front of each LiDAR systems illustrated in Figure 4.3. For vehicles with sensor fusion of different types like LiDAR, radar and camera, the LTS can be expanded to a general target simulator including the existing approaches of radar target simulators [101, 102].

4.3 Used Example LiDAR Systems for LTS Design

To evaluate the feasibility of the introduced LTS design, a possible LTS is designed during the following concept description with regards to three example LiDAR sys-

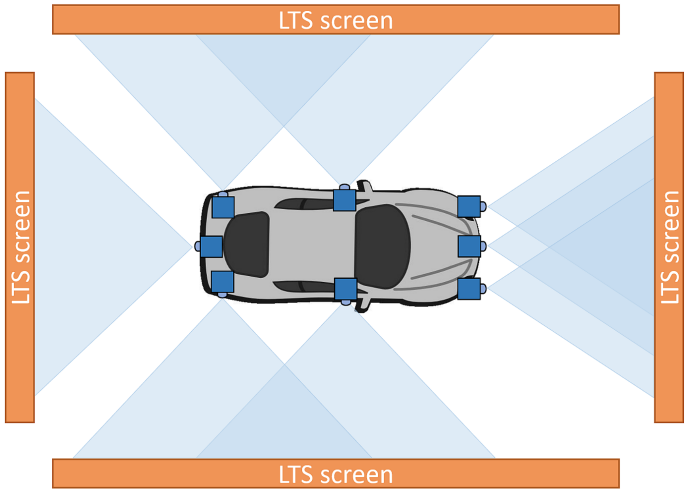

Figure 4.3: Vehicle with multiple LiDAR systems with arbitrary FOVs simultaneously tested by four flat LTS screens surrounding the vehicle

tems with the parameters given in Table 4.1. In this section, these system parameters are explained in more detail to outline the similarities and differences of these systems, which will influence the LTS design. The focal length f and the pixel area A_{px} determine the FOV. The receiving optics are defined by the focal length f and the aperture diameter D, which determine the received light amount given by the reciprocal of the f-number k, which is calculated by $k = f/D$. Therefore, the LiDAR system of Lange is expected to collect the most light followed by Beer and after that Padmanabhan et al. For the sensor performance, it is relevant on which pixels this light is distributed. The pixel area is the largest for Padmanabhan et al., whereas it is small for Beer presenting four SPADs per pixel and very small for Lange containing one SPAD per pixel. The highest optical power is 75 W of Beer's system, which is projected on a line with $40° \times 1°$, Lange has 0.700 W in a round solid angle with diameter 50° and Padmanabhan et al. distribute 0.020 W on $20 \times 20\ (°)^2$. The transmissions of all optic components like emitting and receiving lens systems is best for Padmanabhan et al. with 80 %, Beer states 50 % and Lange 35 %. As Lange states only the values for a single SPAD, the fill factor can be assumed as 100 %. The fill factor of Padmanabhan is high with 50 % and lowest for Beer with 5.32 %. Lange has a high PDP of 65 % at a wavelength of 630 nm, which is part of visible wavelength range including the highest PDP values of silicon detectors. Padmanabhan et al. have a PDP of 10 % at 780 nm, where the near-infrared range begins. Beer has 1.89 % PDP at a near-infrared wavelength of 905 nm, where the

Table 4.1: Parameter values of example LiDAR systems

Parameter	Symbol	Unit	Lange [41]	Beer [103]	Padmanabhan et al. [104]
Focal length	f	mm	2.6	12	15.4
Aperture diameter	D	mm	2.6	9.23	11
Pixel area	A_{px}	µm^2	12.5×14.5	40.6×52.4	240×240
Optical power	Φ_{L}	W	0.7	75	0.02
Laser opening angle	θ_{L}	°	50 (round)	40×1	20×20
Optics transmission	T	%	35	50	80
Fill factor	η_{FF}	%	100[a]	5.32	50
PDP	η_{PDP}	%	65	1.89	10
Wavelength	λ	nm	630	905	780

[a] The pixel area A_{px} means the active optical area of the pixel so that the fill factor is set to 100 %.

PDP of silicon is significantly lower than in the visible range. These different LiDAR system parameters will influence the LTS design and the corresponding calculations, which are presented in the following.

4.4 LTS Screen

The suggested screen of the LTS is shown in Figure 4.4. The drawn screen is curved in both directions: horizontal and vertical. To receive the original laser pulses of the LiDAR system, it contains a single optical trigger, which is marked as black filled circle in the top left corner of the screen. This optical trigger is suitable for flash LiDAR but can also be adapted to scanning LiDAR, which is described later in section 4.6. Multiple LTS sources are placed on the screen, which can emit signals to emulate a virtual scenario on the pixels of the LiDAR system. The drawn light

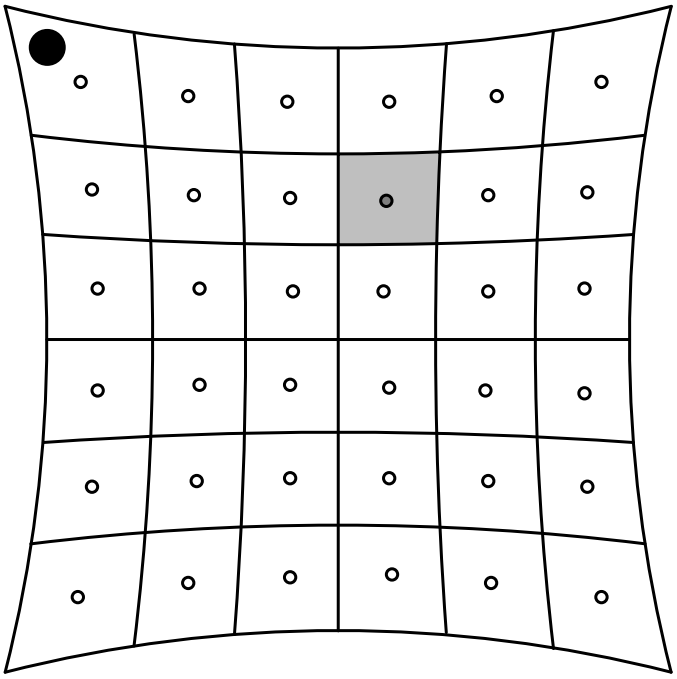

Figure 4.4: Example of a curved LTS screen with 36 LTS sources and one optical trigger in the top left corner. One LTS source with area A_{src} is marked in dark gray with its LTS pixel area $A_{\text{LTS,px}}$ in light gray. [40]

gray area demonstrates the area belonging to one LTS pixel, whereas the dark gray circle represents the LTS source area. In the following, more detailed considerations are discussed. The required screen distance is determined. The curved screen form is compared to a screen that is flat in one or both directions. After that, possibilities for the LTS source placement on the screen will be investigated. If the original laser pulse of the LiDAR system is not fully absorbed by the LTS screen, the real reflection from the screen can be detected by the LiDAR system under test. Therefore, a concept for an antireflective screen is developed.

4.4.1 Required Screen Distance

The screen distance is an important factor to produce a sharp image at the LiDAR system. The optics of a LiDAR system defines in which range this system can produce a sharp image of the seen targets. If a target is too close in front of the sensor, its image can be blurred. Depending on the optics, the same problem can occur again for very distant targets. Especially for automotive applications, the

receiving lens system is often focused to infinity by placing the sensor in the focal plane of the receiving optics. Then, the depth of field (DOF) begins comparatively far away from the LiDAR system but reaches infinity. For infinity focus, the focal length of the receiving optics is set to the hyperfocal distance, which is defined by the tolerated circle of confusion (CoC) indicating the maximum size of blurred image elements. For LiDAR systems, the allowed CoC is given by the largest pixel dimension or the corresponding pixel pitch z. The resulting DOF begins at the near point d_n, which is the half of the hyperfocal distance d_h given by

$$d_\mathrm{n} = \frac{d_\mathrm{h}}{2} = \frac{f}{2}\left(1 - \frac{D}{z}\right), \tag{4.1}$$

where f is the focal length and D the aperture diameter [105]. The LTS screen should be placed in within the DOF, which means a screen distance equal or larger than the near point. The near points are calculated for the three example LiDAR systems. Lange and Padmanabhan et al. have short near points with 8 cm and 26 cm, whereas Beer has a large near point of 1.37 m. For these exemplary cases, a sufficient screen distance s of an LTS designed for all of these three systems would be $s = 1.5\,\mathrm{m}$. With this screen distance, the screen size can be calculated now for a given FOV. Many LiDAR systems are designed with larger horizontal than vertical FOV. Assuming a large FOV of $\theta_\mathrm{FOV,H} \times \theta_\mathrm{FOV,V} = 90° \times 30°$, the screen size results in

$$A_\mathrm{LTS} = 2s \sin\left(\frac{\theta_\mathrm{FOV,H}}{2}\right) \times 2s \sin\left(\frac{\theta_\mathrm{FOV,V}}{2}\right) = 2.1\,\mathrm{m} \times 0.8\,\mathrm{m}. \tag{4.2}$$

Of course, the screen can be designed larger and only the required LTS sources seen by the respective LiDAR system can be switched on.

4.4.2 Comparison of Curved and Flat Screen

A curved screen is the simplest possibility to control all LTS sources in the same way. If the LiDAR system is positioned exactly in the focus point of the screen curvature, the distance from the LiDAR system to every LTS source is the same. Furthermore, the angular orientation of every LTS source is perpendicular to the screen surface and therefore equal in terms of their angular albedo. Besides, all pixels can be placed in a regular grid on the screen having equal pixel area sizes so that they are seen within the same solid angle from the LiDAR system. In contrast, a flat screen would be easier to construct. Concerning the properties of a curved screen as described

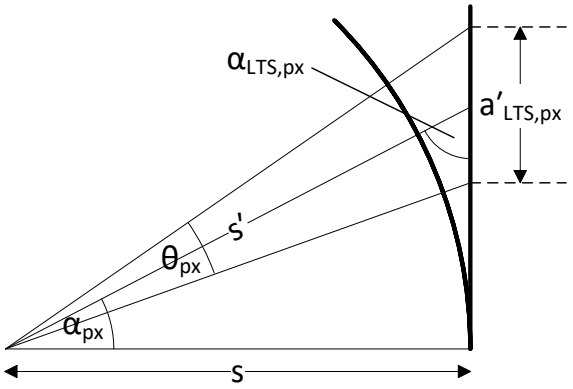

Figure 4.5: Effects of vertically flat screen on LTS source under angle α_{px} with regards to screen distance s' and LTS pixel area $a'_{\mathrm{LTS,px}}$ [40]

above, some adaptions have to be considered if one or both dimensions of the screen are chosen to be flat. In the following, the flattening on the basis of one dimension is discussed, for example if the vertical dimension is desired to become flat. The upper half of a curved screen becoming flat in the vertical dimension is illustrated in Figure 4.5.

The first obvious change is the distance from the LiDAR system to the LTS source especially at the edge of the screen. For a curved screen, every LTS source has the same screen distance s to the LiDAR system. An LTS source observed under angle α_{px} by the LiDAR system results in a new screen distance s' given by

$$s' = \frac{s}{\cos\left(\alpha_{\mathrm{px}}\right)}. \tag{4.3}$$

The angular orientation of the LTS source should be adjusted to the LiDAR system so that the central beam of the LTS source points to the center of the LiDAR aperture. Assuming identical LTS sources with equal optical power, the central beam has the same optical power, which makes calculations easier as discussed later in section 4.5.2. The angle between the central beam of an LTS source changes from the perpendicular orientation to the underlying screen to the new angle $\alpha'_{\mathrm{px}} = \arcsin\left(s/s'\right)$, where s is the screen distance of a curved screen, whereas s' is the new screen distance due to the flat screen form. Alternatively, every LTS source can stay perpendicular on the flat screen and instead, the different intensities arriving at the LiDAR are calculated or measured for each LTS source. This provides the additional advantages that one LTS screen can be used for multiple LiDAR systems, which look on the same LTS screen from different angles. The testing of multiple

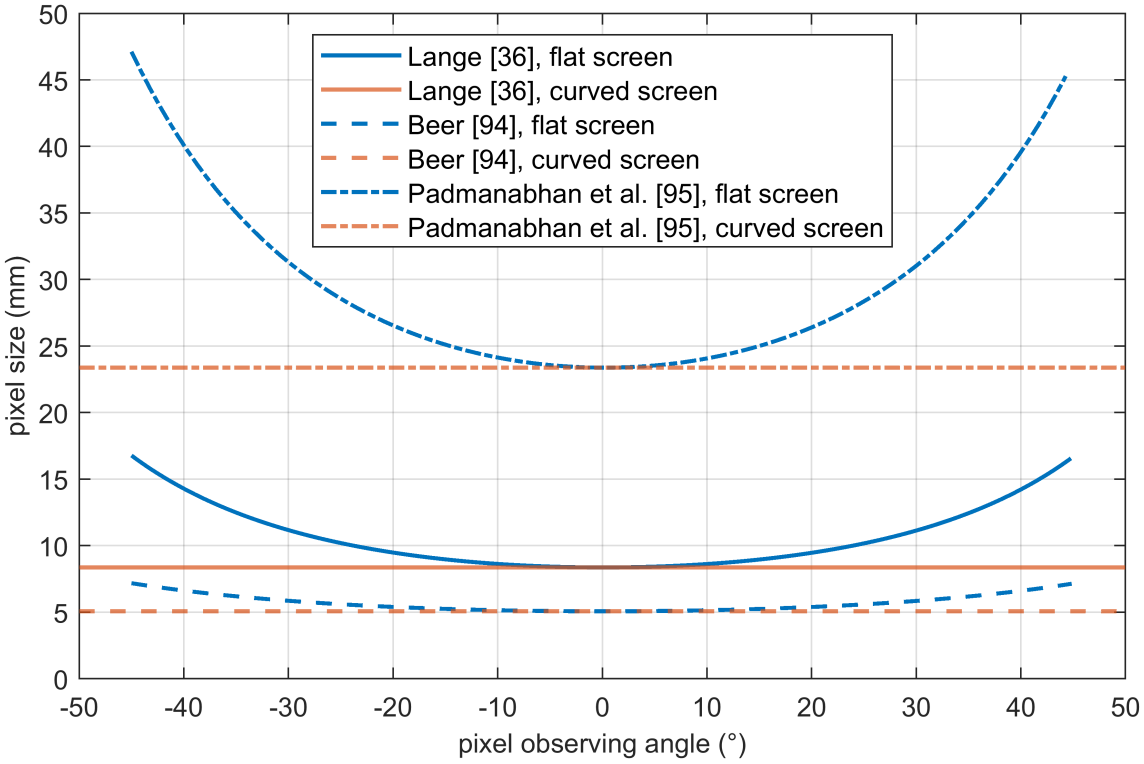

Figure 4.6: Pixel size for curved or flat screen [40]

LiDAR systems can be useful if these systems are used together. For example, several LiDAR systems can be mounted on one vehicle as shown in Figure 4.3. If there are LTS screens in front of all LiDAR systems, the complete autonomous vehicle can be tested at once. This can be realized by curved screens as well but then, there should be one separate curved screen in front of each LiDAR system, which must be exactly placed in the focus point of its screen.

Besides the LTS source angle, the LTS source position must be considered. In general, the LiDAR optics create a homogeneous angular resolution for all pixels resulting in equal pixel FOVs. If these pixels observe a curved screen, each pixel observes the same area on that screen, which is for example one LTS pixel area containing one LTS source. To keep this grid as seen by the LiDAR system, the previously equal grid of LTS sources on the curved must be expanded on the flat screen. Especially LTS sources at the edges would have larger pixel areas on the screen resulting in a new pixel size $a'_L TS, px$ given by

$$a'_{\mathrm{LTS,px}} = \frac{2s' \sin\left(\frac{\theta_{\mathrm{px}}}{2}\right)}{\cos\left(\alpha_{\mathrm{px}} - \frac{\theta_{\mathrm{px}}}{2}\right)}, \tag{4.4}$$

where θ_{px} is the LiDAR pixel FOV. α_{px} is the angle, under which the LiDAR system observes the LTS pixel. These parameters are also drawn in Figure 4.5. The LTS pixel sizes at the edge of the flat screen are significantly larger than those in the center, which is shown in Figure 4.6. For a curved screen, all LTS pixel areas are equally small. The LTS pixel areas are different for each LiDAR system because with increasing pixel FOV, a single pixel can observe more area of the LTS screen. For example, Padmanabhan et al. have a large pixel FOV resulting in a large LTS pixel area.

4.4.3 Comparison of Possible LTS Light Source Grids

The light sources of the LTS can be placed on the LTS screen with different grid sizes. In contrast to real target reflections, the LTS can only emulate discretized reflections by specific target points. With increasing number of LTS sources on the screen, the LTS approaches the continuous reflection pattern of real targets. There are three main possibilities to choose the LTS source grid, which are shown in Figure 4.7. At a minimum, there should be as many LTS sources as there are pixels in the LiDAR systems so that each LiDAR pixel observes one LTS source representing a matching LTS source grid. With increasing number of LTS sources, one LiDAR pixel can be illuminated by more than one LTS source. Depending on the observed number of LTS pixels, the total optical power arriving at one LiDAR pixel can be calculated, which is denoted as rematching LTS source grid. The third option is a fine LTS source grid, where the large number of sources behaves approximately like a real scene and the LiDAR pixel FOV does not have to be considered anymore. These three grids are analyzed in the following.

For the matching LTS source grid, each LTS source must be placed on the screen within one LiDAR pixel FOV as seen in Figure 4.7a. For example, Beer provides the smallest pixel FOV θ_{px} in the horizontal dimension, which is determined by

$$\theta_{\text{px}} = 2 \arctan\left(\frac{a_{\text{px}}}{2f}\right), \tag{4.5}$$

where a_{px} is the pixel size and f the focal length. This pixel FOV requires an LTS pixel size $a_{\text{LTS,px}}$ given by

$$a_{\text{LTS,px}} = s \cdot \theta_{\text{px}} = 5\,\text{mm}, \tag{4.6}$$

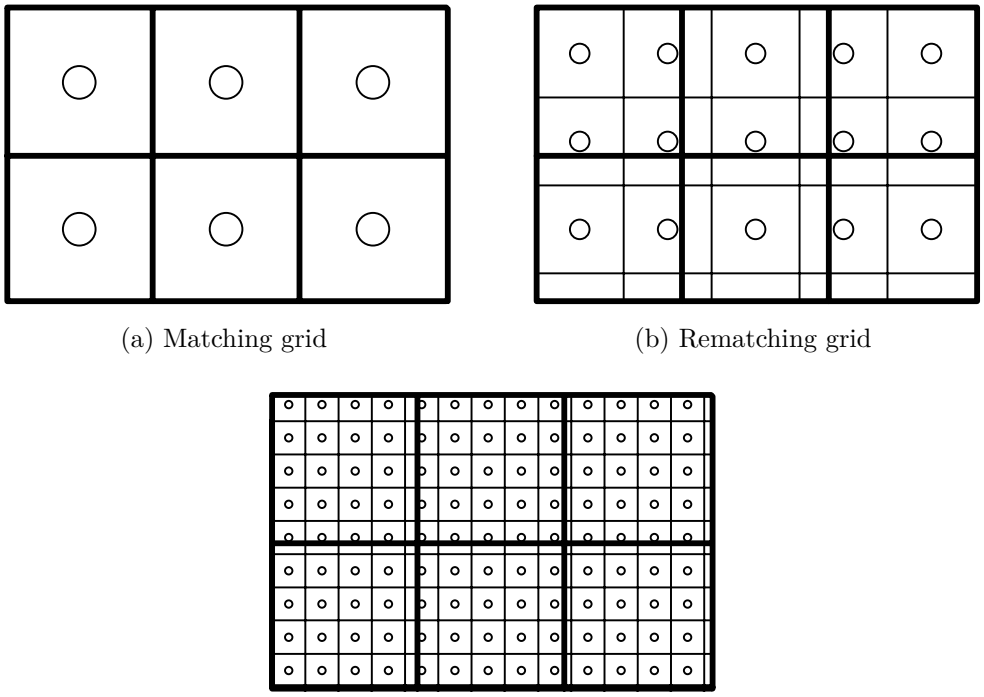

(a) Matching grid

(b) Rematching grid

(c) Fine grid, with LiDAR pixel observing most LTS sources (top center) and least LTS sources (bottom left)

Figure 4.7: Possible LTS source grids on LTS screen (thin grids) overlaid by grid of six LiDAR pixels observing the LTS screen (thick grid) [40]

which depends on the screen distance s. This LTS pixel area is very small, especially with regards to the electronics like the laser drivers, which must be placed side by side behind the LTS screen. Furthermore, every LiDAR system requires a different matching grid so that the LTS sources must be rearranged for every LiDAR system to be tested. On the other hand, manufacturers can use a separate LTS for each of their LiDAR system types so that no rearrangement of the LTS sources is required. The matching grid has the great advantage that the determination of the optical power becomes easier because there is only one LTS source providing the total optical power of one LiDAR pixel but the LTS sources have to be rearranged for each new LiDAR system.

The rematching LTS source grid requires no rearrangement of the LTS sources on the screen. The grid can always stay the same, whereas only the calculation of the optical power changes. In general, the number of LTS sources is not a multiple of

the number of LiDAR pixels so that the LiDAR pixels can observe different numbers of LTS sources. This is seen in Figure 4.7b, where the top left LiDAR pixel looks at four LTS sources, whereas the bottom left LiDAR pixel observes two LTS sources and the bottom center LiDAR pixel even sees only one LTS source. To adjust the optical power at the LiDAR pixel received by the LTS, the desired optical power must be split on all observed LTS sources within one LiDAR pixel FOV.

The fine LTS source grid must contain a large number of LTS sources as illustrated in Figure 4.7c. As already seen at the rematching grid, the number of observed LTS sources per pixel varies. In Figure 4.7c, the most LTS sources are seen by the LiDAR pixel in the top center containing 25 LTS sources, whereas only 16 LTS sources lie within the pixel FOV of the bottom left pixel. The mismatch between the highest and lowest number of seen LTS sources should be negligible. For an LTS pixel area $A_{\mathrm{LTS,px}} = a_{\mathrm{LTS,px,H}} \times a_{\mathrm{LTS,px,H}}$ and LiDAR pixel FOV $\Omega_{\mathrm{px}} = \theta_{\mathrm{px,H}} \times \theta_{\mathrm{px,H}}$, this maximum uncertainty can be calculated by

$$\sigma_{\mathrm{mismatch}} = 1 - \frac{\left\lfloor \frac{s \cdot \theta_{\mathrm{px,H}}}{a_{\mathrm{LTS,px,H}}} \right\rfloor \left\lfloor \frac{s \cdot \theta_{\mathrm{px,V}}}{a_{\mathrm{LTS,px,V}}} \right\rfloor}{\left\lceil \frac{s \cdot \theta_{\mathrm{px,H}}}{a_{\mathrm{LTS,px,H}}} \right\rceil \left\lceil \frac{s \cdot \theta_{\mathrm{px,V}}}{a_{\mathrm{LTS,px,V}}} \right\rceil}, \tag{4.7}$$

where s is again the screen distance. Assuming again the smallest pixel FOV of 0.2° for the horizontal as well as the vertical dimension and a maximum uncertainty of 5 %, the number of LTS sources must be larger than the number of LiDAR pixels by a factor between 39 and 40. As a result, the maximum LTS pixel size becomes 0.1 mm, which seems to be impossible to realize. Besides, such a large number of LTS sources would increase the potential of unwanted reflections from the LTS screen surface to the LiDAR system, which is analyzed in the following section.

4.4.4 Concept for an Antireflective Screen

The laser light from the LiDAR system is probably not completely absorbed by the LTS screen because the screen itself and the LTS sources on it can reflect the light back to the LiDAR system. The coverage of the laser path from the laser exit aperture at the LiDAR system to the optical trigger at the LTS screen seems to be a simple solution. Without an installed mounting option for the coverage or without removing the LiDAR system housing, it can be difficult to attach a

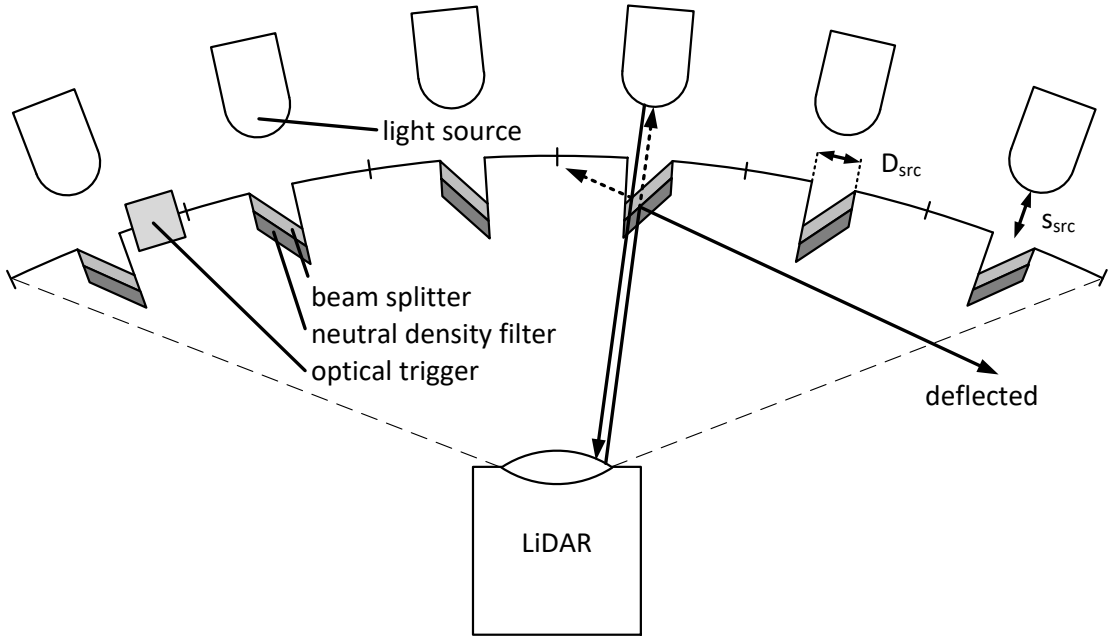

Figure 4.8: Cross-section of LTS screen with antireflective surface by beam splitters and neutral density filters [40]

light-proof coverage. Especially for scanning LiDAR with moving mirrors or a FOV of 360°, such a coverage can be unrealizable. Instead, a concept of an antireflective screen is developed as illustrated in Figure 4.8. The Figure shows a cross-section of the LTS screen seen from above with the LiDAR system in front of it. In the Figure, the LiDAR system illuminates six LTS pixels, of which the pixel at the left edge additionally contains the optical trigger to receive the laser light from the LiDAR system.

At first, the maximum optical power at the LiDAR system is calculated, which must be small enough that the influence on the LiDAR measurement becomes negligible. Assuming the third use case scenario from Table 3.1 in the previous chapter, a range of 250 m is realistic for a long-range LiDAR system. The measurement time corresponding to the histogram length t_{hist} is determined by rearranging (2.1) resulting in $t_{\text{hist}} = 1.67\,\mu\text{s}$. An acceptable low laser-generated event rate in a LiDAR measurement can be defined by one or less expected event per measurement time. This maximum rate r_{LTS} caused by the own laser light is given by the reciprocal of the histogram length t_{hist} with

$$r_{\text{LTS}} = \frac{1}{t_{\text{hist}}} = 600\,\text{kHz}. \tag{4.8}$$

Assuming a shorter detection range, this event rate can be even higher, which makes the longest range the most restrictive case. The reflectivity of one LTS pixel depends on the event rate due to the LTS pixel area r_{px} and the event rate produced by the LTS source of this pixel r_{src} resulting in

$$r_{\mathrm{LTS}} = r_{\mathrm{px}} + r_{\mathrm{src}} \approx r_{\mathrm{src}}, \tag{4.9}$$

where the influence of the pixel area can be neglected compared to the impact of the LTS source as seen in the following. The proportion of the illumination of the screen surface η_{px} from one pixel area without the LTS source area A_{src} is given by

$$\eta_{\mathrm{px}} = 1 - \frac{A_{\mathrm{src}}}{A_{\mathrm{LTS,px}}} = 1 - \frac{A_{\mathrm{src}}}{s^2 \Omega_{\mathrm{px}}}, \tag{4.10}$$

where the LTS pixel area $A_{\mathrm{LTS,px}}$ is determined by the LiDAR pixel with solid angle Ω_{px} in the case of a matching grid. If the screen surface is covered by material with beam trap quality, the reflectance can be very low like $\rho_{\mathrm{screen}} = 10^{-6}$ [106]. The laser-generated event rate due to the screen surface is given by the optical power equation (2.17), which transforms here into

$$r_{\mathrm{px}} = \Phi_{\mathrm{L}} \eta_{\mathrm{px}} \left(\frac{D}{2s} \right)^2 \frac{\Omega_{\mathrm{px}}}{\Omega_{\mathrm{L}}} \rho_{\mathrm{screen}} T \eta_{\mathrm{FF}} \eta_{\mathrm{PDP}} \frac{\lambda}{hc}. \tag{4.11}$$

The resulting event rates are small for all example LiDAR systems as seen in Table 4.2. Therefore, the screen reflectance itself is negligible and the LTS source reflection is investigated in the following.

To reduce the LTS source area, the actual LTS lights can be placed behind the screen that gets small holes to let their light pass as seen in Figure 4.8. A hole diameter of $D_{\mathrm{src}} = 100\,\mu\mathrm{m}$ leads to an LTS source area A_{src} of

$$A_{\mathrm{src}} = \pi \left(\frac{D_{\mathrm{src}}}{2} \right)^2 = 0.008\,\mathrm{mm}^2. \tag{4.12}$$

To guarantee that the LiDAR system observes this total LTS source area, the minimum LiDAR pixel FOV θ_{px} must be

$$\theta_{\mathrm{px}} = 2 \arctan \left(\frac{D_{\mathrm{src}}}{2s} \right) = 0.004°, \tag{4.13}$$

which is probably fulfilled for all LiDAR systems. Furthermore, the holes must be large enough that the LTS sources can illuminate the total LiDAR aperture, which

Table 4.2: Antireflective screen parameters with laser-generated event rates for example LiDAR systems specified in Table 4.1

Parameter	Symbol	Unit	Lange [41]	Beer [103]	Padmanabhan et al. [104]
Max. event rate from total LTS	r_{LTS}	kHz	600	600	600
Event rate from screen	r_{px}	kHz (%)	0.001 (0.0001)	0.53 (0.09)	0.02 (0.0003)
Max. event rate from LTS sources	r_{src}	kHz (%)	599.9990 (99.9998)	599.4653 (99.91)	599.9781 (99.997)
Max. LTS source reflectivity	ρ_{src}	%	100	100	100
Max. ND transmission	T_{ND}	%	0.05	0.05	0.05

is given for real target reflections as used later in the optical power calculation. Alternatively, the LTS lights can be placed closer to the screen so that their light gets through the hole at larger angles. For a large round LiDAR aperture with diameter $D = 5\,\mathrm{cm}$, the maximum distance s_{src} between LTS light and hole is calculated by

$$s_{\mathrm{src}} = \frac{s \cdot D_{\mathrm{src}}}{D - D_{\mathrm{src}}} = 3.0\,\mathrm{mm}. \tag{4.14}$$

Applying these geometric considerations, only the reflectivity of the LTS sources remains as an adjustable parameter. To achieve an antireflective screen, beam splitters are suggested in front of the LTS sources as shown in Figure 4.8. The beam splitter divides the laser light from the LiDAR system into a transmitting proportion still reaching the LTS source surface and a deflected proportion. The transmitted light will still be reflected at the LTS sources but then again passes the beam splitter, where once again only half of the light is transmitted back to the LiDAR system. For the deflection, the angle of the beam splitter must be chosen large enough so that the light is not reflected back to the LiDAR system but anywhere next to it. Considering a LiDAR system in front of a mirror as seen in Figure 4.9, the minimum

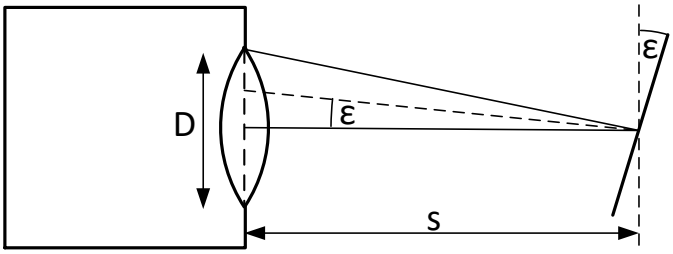

Figure 4.9: Minimum mirror angle for deflection of LiDAR's laser beam [40]

deflection angle is given for the central ray because with increasing emitting angle, the incident angle on the mirror and hence the reflection angle will increase due to the law of reflection. Therefore, the required minimum angle ε of the central mirror on the LTS screen is given by

$$\varepsilon = \frac{1}{2} \arctan\left(\frac{D}{2s}\right) \geqslant 0.48°. \tag{4.15}$$

This angle is very small and easy to realize so that it is not necessary to calculate the even smaller minimum deflection angles of the LTS sources at the edge of the screen. Choosing an angle equal or larger than the calculated one, all beam splitters can be arranged with the same angle with respect to the radial line of sight of the LiDAR system.

The light transmitted two times by the beam splitter or diffusely reflected from the beam splitter surface directly back to the LiDAR system can be combined in a total beam splitter reflectivity. The remaining light from the beam splitter to the LiDAR system determines the received laser-generated event rate r_{src} of the LTS source with reflectivity ρ_{src} calculated by

$$r_{\mathrm{src}} = \Phi_{\mathrm{L}} \eta_{\mathrm{src}} \left(\frac{D}{2s}\right)^2 \rho_{\mathrm{src}} T \eta_{\mathrm{FF}} \eta_{\mathrm{PDP}} \frac{\lambda}{hc}, \tag{4.16}$$

which is again the application of (2.17). η_{src} is the proportion of the LiDAR light on the LTS source area A_{src} compared to the total target area A_{target} given by

$$\eta_{\mathrm{src}} = \frac{A_{\mathrm{src}}}{A_{\mathrm{target}}} = \frac{A_{\mathrm{src}}}{s^2 \Omega_{\mathrm{L}}}, \tag{4.17}$$

where the illuminated target area A_{target} is determined by the laser solid angle Ω_{L} of the LiDAR system. Combining the approximation of (4.9) and the other calculations, the allowed maximum reflectivity of the LTS source ρ_{src} is determined by

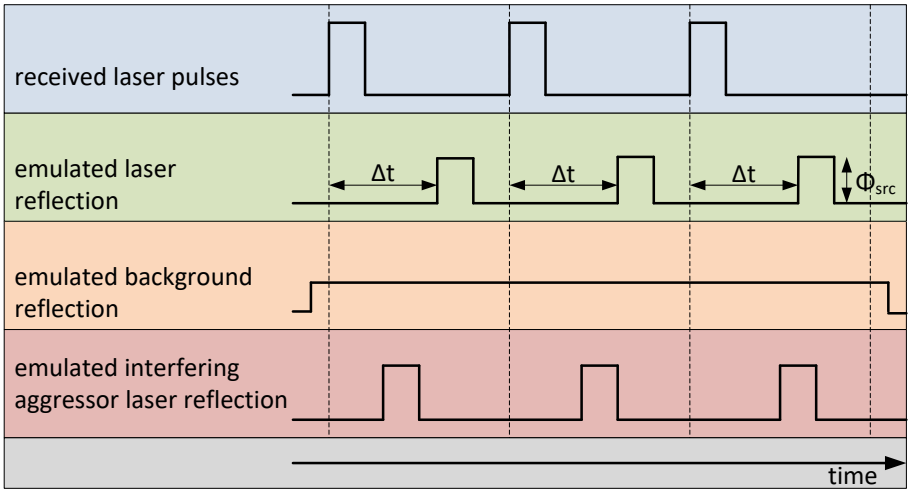

Figure 4.10: Adjusted time delay Δt and optical power of the LTS source Φ_{src} for emulation of reflected ego laser pulses, background light and aggressor laser pulses from direct or indirect interference.

$$\rho_{\mathrm{src}} \approx \left(\frac{2s}{D}\right)^2 \frac{r_{\mathrm{LTS}} hc}{\Phi_{\mathrm{src}} T \eta_{\mathrm{FF}} \eta_{\mathrm{PDP}} \lambda}. \tag{4.18}$$

If the beam splitter with reflectivity ρ_{splitter} has a higher reflectivity than this source reflectivity ρ_{src}, the total LTS source reflectivity must be further reduced by neutral density (ND) filters with transmission $T_{\mathrm{ND}} = \rho_{\mathrm{splitter}}/\rho_{\mathrm{src}}$. The ND filters would affect the LTS light as well, but the LTS source power can easily be increased corresponding to the ND filter attenuation. For all example LiDAR systems the maximum LTS source reflectivity exceeds 100 % so that this is the limiting parameter resulting in a required ND filter transmission of 0.05 %, which can be easily achieved by commercial ND filters [107]. Therefore, the concept of an antireflective LTS screen appears as an effective and feasible solution.

4.5 Virtual Scenario Simulation

The LTS provides simulated scenarios with a TOF representing the distance to the simulated target and optical powers of the emulated ego laser reflection, aggressor laser reflection and background reflection for each pixel of the LiDAR system. The concept including timings as well as optical powers is shown in Figure 4.10.

4.5.1 Time of Flight

The LiDAR system emits a laser pulse and starts its TOF measurement at the same time. The laser pulse is transferred to the LTS screen in distance s, where it is detected after a time of $t_\mathrm{s} = 2s/c$, which is derived from (2.1). The required delay at the LTS is the desired TOF corresponding to the virtual target distance after (2.1) minus two times the time t_s because the laser pulse emitted from the LiDAR system to the LTS screen and the pulse later emitted from the LTS screen travels to the LiDAR system.

Due to electrical delays e.g. because of cable lengths, the pulse emitted from the LTS can be delayed more than desired. This can make it impossible to emulate short target distances. Besides electrical delays, the possible minimum target distance cannot be less than the LTS screen distance, which is traveled by the real light. As a possible solution, the LTS can skip the first received laser pulse from the LiDAR system as shown in Figure 4.11. At the second LiDAR measurement, the LTS emits a pulse before the second laser pulse of the LiDAR system is detected based on a prediction of the arrival time of this second laser pulse from the LiDAR system. This only works for predictable regular and not for random pulse emission patterns. However, it must be considered that targets at very short distances might not be sharply imaged on the LiDAR detector, which is the reason for the large screen distance $s = 1.5\,\mathrm{m}$ as described in section 4.4.1. For applications like autonomous driving, it might be irrelevant whether such a close target is sharply imaged because it can be more important to detect the target at all allowing for a fast reaction of the autonomous vehicle. However, it is possible to simulate the blurring effect by the sharply imaged LTS screen for virtual target distances shorter than the screen distance. Therefore, the calculated light amount can be distributed within the CoC given by

$$z = \frac{f \cdot D}{2d_\mathrm{n} - f}, \tag{4.19}$$

which is equivalent to (4.1). In general, the focal length f might be unknown for a LiDAR system so that this can be an unrealistic possibility.

For the delay at the LTS, a delay element can be used with coarse and fine delay. The coarse delay can control the waiting time to the next laser pulse emission by the LiDAR system for the emulation of short target distances. In the automotive field, often 25 Hz are demanded because the reciprocal corresponds to a frame time

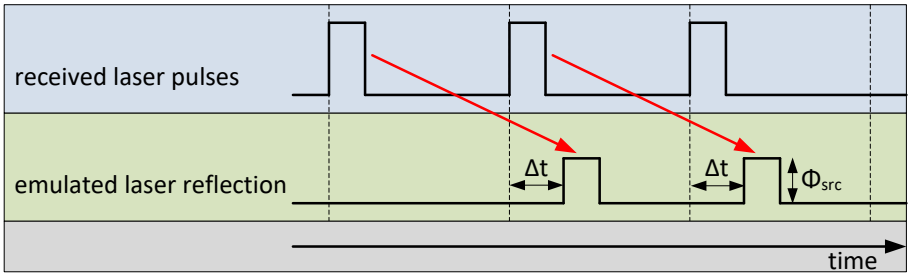

Figure 4.11: Timing at LTS for emulation of short virtual target distances, which might be even shorter than the LTS screen distance

$t_{\text{frame}} = 40\,\text{ms}$, which is in the order of visual perception and hence also used in video recording [108]. After (2.1), a target distance of 250 m from the third use case scenario in Table 3.1 is equivalent to a measurement time or rather histogram length of $t_{\text{hist}} = 1.67\,\mu\text{s}$. The LiDAR system is assumed to use a regular pulse emission pattern, where the duration between two pulses is any multiple of the measurement time. The time between two pulses can change from pulse to pulse but at a certain point, the pattern must be repeated so that the LTS can predict the next pulse. Such a pattern can be given for scanning LiDAR systems or interference suppression methods, which are explained in more details later in section 6.1. Therefore, the coarse delay must be adjustable in steps of the histogram length $t_{\text{hist}} = 1.67\,\mu\text{s}$ up to the total frame time $t_{\text{frame}} = 40\,\text{ms}$ resulting in a number of coarse steps n_{coarse} determined by

$$n_{\text{coarse}} = \left\lceil \frac{t_{\text{frame}}}{t_{\text{hist}}} \right\rceil = 20000 \quad \Rightarrow \quad 15\,\text{bit}, \tag{4.20}$$

which is equivalent to a counter with 15 bit. The fine delay represents the time resolution given by the bin width of the LiDAR system. Considering the bin width $t_{\text{bin}} = 312.5\,\text{ps}$ from LiDAR system *Owl* described in section 2.1.4, the required number of fine steps n_{fine} is calculated by

$$n_{\text{fine}} = \left\lceil \frac{t_{\text{hist}}}{t_{\text{bin}}} \right\rceil = 6400 \quad \Rightarrow \quad 13\,\text{bit}, \tag{4.21}$$

which corresponds to a counter with 13 bit. To emulate aggressor laser pulses, the same delays are applicable because the derived delay elements only depend on the LiDAR detector but not on the laser properties of the LiDAR system. The aggressor system is completely virtual and requires no other real LiDAR system in the laboratory. Therefore, the aggressor system can also be emulated with a irregular pulse pattern, which is chosen as part of the virtual scenario.

4.5.2 Optical Power of Laser Reflection

The required optical power of an LTS source must be known to emulate the virtual target reflection of the real laser pulse emitted from the LiDAR system. From the LTS source illumination, only the solid angle pointing to the LiDAR aperture is relevant. The flat LiDAR aperture is illuminated under a full angle $\alpha_{\mathrm{src,illum}}$ of

$$\alpha_{\mathrm{src,illum}} = 2 \arctan\left(\frac{D}{2s}\right) \approx \frac{D}{s} = 2°, \tag{4.22}$$

where the small angle allows for approximations. For these small angles, the illumination of the LiDAR aperture can be assumed to be homogeneous. For larger angles, most light sources show a spatially decreasing illumination on a flat area producing inhomogeneous irradiances on the LiDAR aperture as well. The irradiance E_{src} of an LTS source with optical power Φ_{src} and solid angle Ω_{src} on the LiDAR aperture is given by

$$E_{\mathrm{src}} = \frac{\Phi_{\mathrm{src}}}{s^2 \Omega_{\mathrm{src}}}, \tag{4.23}$$

where s is the screen distance up to which the LTS source illumination is expanded within the solid angle. For LTS sources at larger angles α_{px}, especially at the screen edge, the irradiance is reduced by $\cos(\alpha_{\mathrm{px}})$ because these LTS sources illuminate a larger area at the flat plane of the LiDAR aperture. To correct this irradiance loss, the optical power can be simply increased by the same factor. The irradiance E_{src} must match the irradiance $E_{\mathrm{refl,laser}}$ that is given by a real target reflection at the LiDAR aperture resulting in the condition

$$E_{\mathrm{src}} \stackrel{!}{=} E_{\mathrm{refl,laser}}. \tag{4.24}$$

The optical power $\Phi_{\mathrm{target,L}}$ of the LiDAR system arriving at the target area observed by one LiDAR pixel is given in (2.11). There are three main reflection types that are discussed in the following: a diffuse Lambertian reflection, a retroreflection and a specular reflection. In reality, often mixed forms occur like combinations of diffuse and specular reflection. In the following, the ideal reflection types and their scenario simulations with regards to optical power are considered.

A Lambertian reflection of a single target point distributes the reflected light in a hemisphere as shown in Figure 4.12. Depending on the emission angle, the reflected irradiance on the hemisphere follows the Lambertian law in (2.14) so that the irradiance is the highest at an angle of 0°, which is indicated by the brightest

color in the center of each distribution corresponding to 100 % intensity. According to the inverse square law, with increasing radius of this hemisphere, the irradiance decreases [71]. The Lambertian angular distribution remains unchanged for a larger hemisphere radius corresponding to a higher target distance. However, a flat area with fixed size like the LiDAR aperture will receive less reflected light at a larger target distance, which is seen in Figure 4.12 for three illumination distances on an example area with fixed size of 2.8 m. With regards to a small LiDAR aperture with a diameter equal or less than 5 cm, the illumination change due to different distances becomes negligible as seen in the enlarged section shown in Figure 4.12. Even for the short screen distance $s = 1.5\,\mathrm{m}$, the intensity at the aperture edge is still 99.986 %. Therefore, it is assumed that the Lambertian reflection illuminates the total LiDAR aperture homogeneously. The irradiance of a Lambertian target at an angle of 0° in distance d is given by

$$E_{\mathrm{refl,diffuse}} = \frac{\rho \Phi_{\mathrm{target,L}}}{\int_0^d \int_0^{2\pi} \int_0^{\frac{\pi}{2}} \delta(r-d) r^2 \cos(\theta) \sin(\theta) \mathrm{d}\theta \mathrm{d}\phi \mathrm{d}r} = \frac{\rho \Phi_{\mathrm{target,L}}}{d^2 \pi}, \tag{4.25}$$

where ρ is the target reflectance and $\delta(r-d)$ represents the integration over a spherical shell with target distance d as radius r. Inserting this in (4.24) and converting to the required LTS source power $\Phi_{\mathrm{src,diffuse}}$ provides

$$\Phi_{\mathrm{src,diffuse}} = \frac{s^2 \Omega_{\mathrm{src}} E_{\mathrm{refl,diffuse}}}{T_{\mathrm{src}}}, \tag{4.26}$$

where the optical power loss given by the transmission T_{src} of the LTS source due to optics transmissions or the realization of an antireflective screen as described in section 4.4.4 using a beam splitter and ND filters is already compensated. Inserting the required irradiance due to the target reflection $E_{\mathrm{refl,diffuse}}$ from (4.25) and the included $\Phi_{\mathrm{target,L}}$ from (2.21), the calculated optical power of the LTS source $\Phi_{\mathrm{src,diffuse}}$ can be divided into several factors so that the working principle of scenario simulation is better seen. The resulting term is given by

$$\Phi_{\mathrm{src,diffuse}} = \Phi_{\mathrm{L}} \cdot \rho \cdot \underbrace{\left(\frac{s}{d}\right)^2}_{=\eta_d} \cdot \underbrace{\frac{\Omega_{\mathrm{src}}}{\pi}}_{=\eta_{\mathrm{src}}} \cdot \underbrace{\frac{\min\left(\Omega_{\mathrm{px}}, \Omega_{\mathrm{L}}\right)}{\Omega_{\mathrm{L}}}}_{=\eta_{\mathrm{illum}}} \frac{1}{T_{\mathrm{src}}} = \Phi_{\mathrm{L}} \cdot \rho \cdot \eta_d \cdot \eta_{\mathrm{src}} \cdot \eta_{\mathrm{px}} \cdot \frac{1}{T_{\mathrm{src}}}. \tag{4.27}$$

The optical laser power Φ_{L} is not affected because this optical power from the real LiDAR system is transferred to the virtual scenario connecting reality and virtual reality. As reflectance, only the virtual target reflectance ρ is included because the

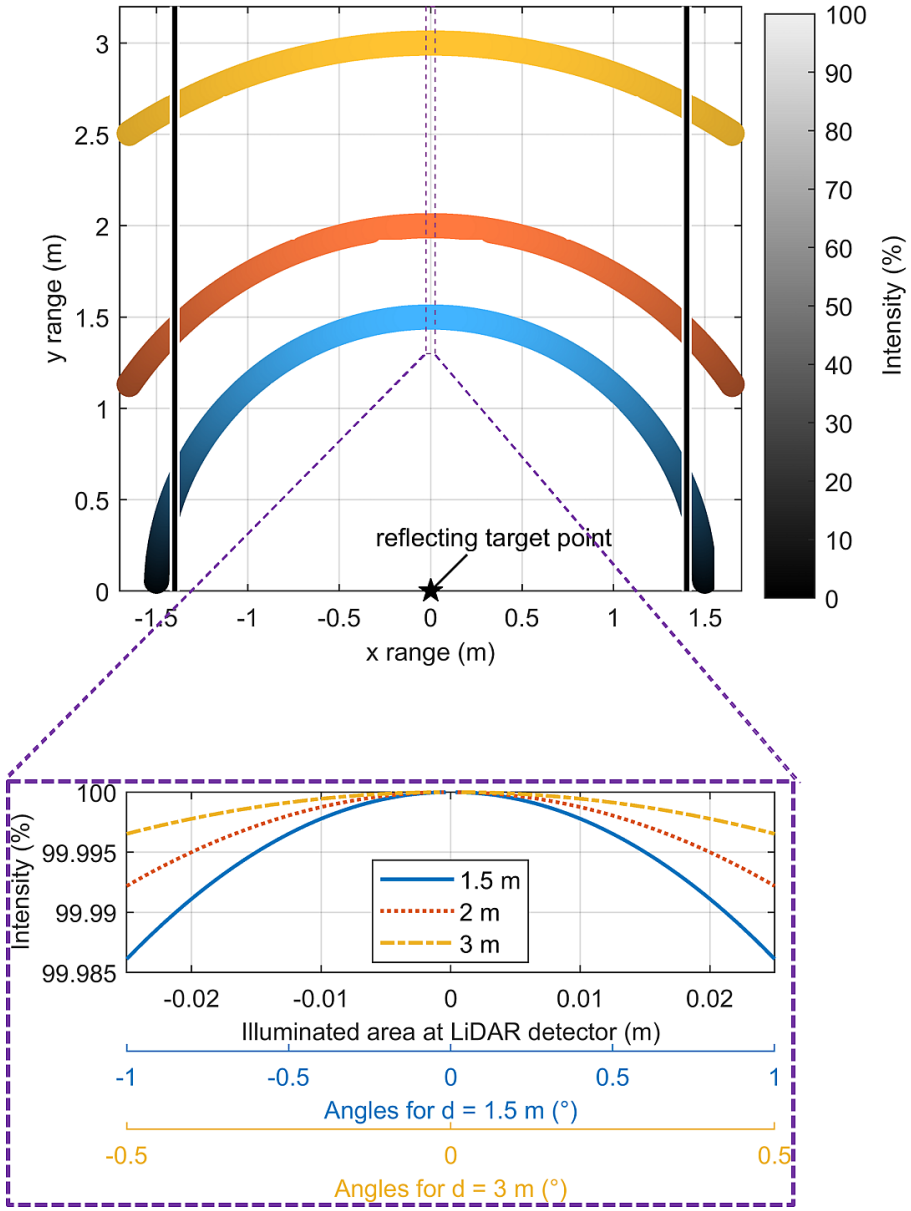

Figure 4.12: Influence of target distance on Lambertian cosines distribution in horizontal dimension within fixed illumination area of 2.8 m, which is zoomed in to 5 cm [40]

real reflectance at the LTS screen can be avoided using the concept of the antireflective screen described in section 4.4.4. The factor η_d indicates the proportion of the virtual target distance d to the real screen distance s. The illumination factor η_{illum} is known from (2.11) and represents the proportion from the total illuminated target area to the target area observed by a single pixel, which must be emulated by a single LTS point source instead of a target area. Finally, the transmission T_{src} demonstrates the unwanted optical power losses at an LTS source. This optical power calculation for a diffuse Lambertian target reflection shows the connection from the optical power of a real target compared to a virtual target with chosen distance and reflectance.

A retroreflector is designed to reflect incident light back in the same direction producing a high visibility. For example, road signs and license plates are made of retroreflectors. Their reflectivity R can reach values up to $R = 80\,\% - 90\,\%$ [109]. The resulting irradiance from a retroreflector at the LiDAR aperture with area A_{aperture} is given by

$$E_{\text{refl,retro}} = \frac{R\Phi_{\text{target,L}}}{T_{\text{src}} A_{\text{aperture}}} = \frac{4R\Phi_{\text{target,L}}}{\pi D^2 T_{\text{src}}}, \tag{4.28}$$

where D is the aperture diameter. Inserting this in (4.24) and again transforming to the required LTS source power $\Phi_{\text{src,retro}}$ results in

$$\Phi_{\text{src,retro}} = \frac{4s^2 R\Phi_{\text{target,L}}\Omega_{\text{src}}}{\pi D^2 T_{\text{src}}}. \tag{4.29}$$

There are different retroreflector types, which might have an even higher reflectivity R resulting in a higher required optical power of the LTS source.

A specular reflection reduces the light only by the reflectance ρ. The light is reflected at the same angle as the incident angle according to the law of reflection. Thus, the reflected light is only received back at the LiDAR system if the mirror surface is almost perpendicular to the system with small enough angle ε as seen in Figure 4.9 with the opposite angle condition of (4.15). If this condition is fulfilled, the required optical power $\Phi_{\text{src,specular}}$ of the LTS source is calculated equivalently to the retroreflection given by

$$\Phi_{\text{src,specular}} = \frac{4s^2 \rho\Phi_{\text{target,L}}\Omega_{\text{src}}}{\pi D^2 T_{\text{src}}}, \quad \varepsilon < \frac{1}{2}\arctan\left(\frac{D}{2s}\right). \tag{4.30}$$

For the construction of the LTS, the dynamic range of the optical power is relevant. The dynamic range is estimated by the diffuse Lambertian reflection because

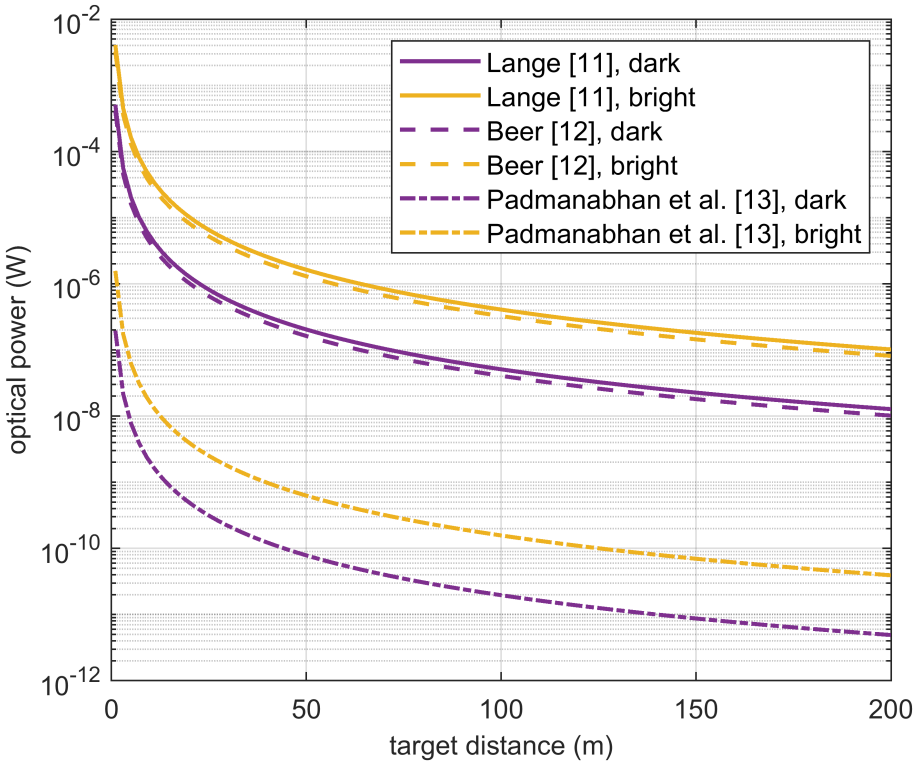

Figure 4.13: Required optical power of LTS sources Φ_{src} for example Lambertian targets, where the dark target is assumed with 10 % reflectance and the bright target with 80 % reflectance [40]

it strongly depends on the target distance in contrast to the retroreflection or specular reflection. Applying the scenario simulation of the Lambertian reflection on the three example LiDAR systems, the required optical power of the central LTS source can be calculated for different desired target distances as seen in Figure 4.13. The dark target has a low reflectance of 10 % and the bright target has 80 % reflectance. With these two target reflectances, the corner cases of required optical power are identified as shown in Table 4.3. Assuming a dark target at a particularly high target distance of 200 m provides the corner case of a very low optical power $\Phi_{\text{src,far,dark}}$ required at the LTS source, whereas a bright target at a low distance of 1 m results in the other corner case of a very high optical power $\Phi_{\text{src,near,bright}}$. The resulting dynamic range is given by

$$Q_{\text{target}} = \frac{\Phi_{\text{src,near,bright}}}{\Phi_{\text{src,far,dark}}} \approx 10^6, \tag{4.31}$$

which is the same for all LiDAR systems. However, this dynamic range starts at different minimum optical powers differing for the LiDAR systems of Lange and

Table 4.3: Corner cases of required optical power of LTS source Φ_{src} (W) of figure 4.13

Target type	Reflectance (%)	Distance (m)	Optical power (W)		
			Lange [41]	Beer [103]	Padmanabhan et al. [104]
Dark	10	200	$1.3 \cdot 10^{-8}$	$1.1 \cdot 10^{-8}$	$4.9 \cdot 10^{-12}$
Bright	80	1	$4.1 \cdot 10^{-3}$	$3.6 \cdot 10^{-3}$	$1.6 \cdot 10^{-6}$

Padmanabhan et al. by a factor Q_{LiDAR} of

$$Q_{\text{LiDAR}} = \frac{\Phi_{\text{src,Lange}}}{\Phi_{\text{src,Padmanabhanetal.}}} \approx 10^3. \tag{4.32}$$

The LiDAR system of Padmanabhan et al. requires the lowest optical power because it uses the lowest optical laser power. An LTS sufficient for all three systems over the total dynamic range of possible scenarios requires LTS sources providing an extreme dynamic range of $Q_{\text{LTS}} = Q_{\text{target}} Q_{\text{LiDAR}} = 10^9$. Such a large dynamic range can be challenging because the LTS light source should be adjustable in sufficient gradations over the total range resulting in many adjustment possibilities. Alternatively, the LTS can be designed only for the dynamic range of a single LiDAR system or the scenarios can be limited to achieve a smaller dynamic range Q_{target}, which is easier to realize. For example, a simple optical power reduction can be achieved by a single ND filter, which can be purchased with small transmissions like 10^{-6} [107]. Furthermore, a light source with adjustable optical power might be suitable. For an automatic LTS setting, the optical power adjustment should be remotely controllable. Altogether, high dynamic range might be achievable but smaller scales simplify the LTS setup.

4.5.3 Optical Power of Interfering Aggressor Laser

For indirect interference, the optical power of aggressor laser pulses reflected from the target is the same as the optical power of reflected ego laser pulses if aggressor and ego LiDAR system are equal and have the same target distance. In the calculations of optical power, a LiDAR system perpendicular to the target surface is assumed. It is impossible that ego as well as aggressor system are located at this same position

in front of the target. If a more precise scenario emulation is desired, exact angular orientations from ego and aggressor system to the target surface can be chosen. With these angles, the Lambertian reflection factor η_{refl} derived in (2.17) can be calculated again for ego system and aggressor system. Besides aggressor LiDAR systems, there can also be other direct light sources illuminating a LiDAR system, e.g. headlights or traffic light for the example of autonomous driving. These light sources are only detected if their spectra lie within the bandpass filter. In general, they differ from aggressor systems because they often provide CW light with a low intensity instead of pulsed light with a high optical power.

4.5.4 Optical Power of Background Reflection

Background light from the sun can continuously illuminate the target so that a CW light at the LTS screen is suitable for the emulation of background light. The pulsed light source for the emulation of reflected laser pulses and the CW light source for the emulation of background light can be combined behind the LTS screen so that the combined light can be emitted through the LTS source holes seen in Figure 4.8. Alternatively, the background light emulation can be achieved by doubling the LTS sources so that there are two light sources per pixel seen in Figure 4.4. The increased number of LTS sources increases the potential for unwanted reflections as discussed for the antireflective screen in section 4.4.4. The optical power caused by background light on a target area seen by one LiDAR pixel is given by $\Phi_{\text{target,B}}$ from (2.21). The reflection types with regards to reflected laser light discussed in the section before can be applied as well for the background light. Only the target illumination by the laser $\Phi_{\text{target,L}}$ has to be replaced by the target illumination due to background light $\Phi_{\text{target,B}}$.

4.6 Calibration

The LTS should ideally benchmark different LiDAR systems without previous knowledge about these systems so that no bias or misleading information can influence the testing results. However, some LiDAR system parameters must be known to calibrate the LTS with regards to the specific requirements of each LiDAR system. For the screen design, especially the LTS source grid must be adjusted, which requires knowledge about spatial LiDAR parameters. For the scenario simulation including

TOF and optical power, the LiDAR parameters with regards to time and optical power must be known. The LiDAR parameter from these three fields space, time and optical power are discussed in the following.

The spatial resolution of a LiDAR system depends on the pixel FOV. This FOV can be measured by moving a target through the pixel FOV. The resulting observed target area from the pixel can be transformed to the pixel FOV by the target distance. If the number of pixels in the horizontal and vertical dimension is unknown, the total LiDAR FOV can be determined in the same way and divided by the pixel FOV to obtain the number of pixels. With the pixel FOV and the number of pixels, the matching or rematching LTS source grid from section 4.4.3 can be arranged on the LTS screen.

To achieve a precise timing of the LTS, the optical trigger on the LTS screen must be able to detect the rising edge of the arriving laser pulse. As the LiDAR system measures with a defined time resolution, the timing of the LTS should be sufficiently precise. This resolution corresponds to the distance resolution. If a target is moved away from the LiDAR system, the smallest distinguishable distance can be converted to the time resolution by (2.1). For example, LiDAR system *Owl* from section 2.1.4 has a bin width of $t_{\mathrm{bin}} = 312.5\,\mathrm{ps}$, which corresponds to a distance resolution of 4.7 cm. If for example a photoreceiver with photodiode is used as optical trigger on the LTS screen, the minimum sampling rate of the photoreceiver f_{PD} should be hence $f_{\mathrm{PD}} = 1/t_{\mathrm{bin}} = 3.2\,\mathrm{GHz}$. This photoreceiver can be used once to measure the emitted pulse form of the LiDAR system, which can provide the optical peak power of the laser and the temporal intensity profile. When pulses from the LiDAR system arrive at the LTS screen, the photoreceiver can detect the rising edge of these pulses as a starting point of the applied LTS delay. For flash LiDAR, one laser pulse is emitted within the total FOV so that this pulse arrives at the total LTS screen. At the edges of a flat screen, this pulse can arrive slightly later than in the center as calculated in section 4.4.2. For scanning LiDAR, the received pulse pattern can strongly vary for the different pixels. The simplest solution would be to place one optical trigger on each LTS pixel, which has the drawback to possibly reduce the antireflectivity of the LTS screen. Instead, the scanning pattern can be measured in advance. Therefore, either the available optical trigger can be moved on the screen to each LTS pixel measuring the specific pulse pattern there or a calibration screen with multiple optical triggers can be placed in front of the LiDAR

system to quickly characterize the scanning pattern.

For virtual scenarios with short target distances, the next pulse arrival time at the LTS screen must be predicted, which is easy for regular pulse patterns. Irregular pulse emission patterns are not only given for scanning LiDAR but can also appear at flash systems with interference suppression methods as described in chapter 6. Similar to scanning LiDAR, the laser pulse emission pattern of the LiDAR system must be identified once. If the pulse emission times are randomly produced, there is no chance for the LTS to predict the next laser pulse so that short target distances cannot be tested.

The jitter of the LTS must be small enough so that it does not affect the emulated TOF. The LTS jitter consists of the jitter given by the optical trigger σ_{trigger}, the electrical jitter due to controlling electronics σ_{ctrl}, the measurement uncertainty of pulse pattern measured in advance σ_{pattern}, each single pulse detection by the optical trigger σ_{pulse} and the emission time jitter of the LTS source σ_{src}. These jitters can be combined by the root mean square (RMS) to a total LTS jitter σ_{LTS} given by

$$\sigma_{\text{LTS}} = \sqrt{\sigma_{\text{trigger}}^2 + \sigma_{\text{ctrl}}^2 + \sigma_{\text{pattern}}^2 + \sigma_{\text{pulse}}^2 + \sigma_{\text{src}}^2}. \tag{4.33}$$

For a precise LTS testing, this jitter should be smaller than the time resolution of the LiDAR system, which is nominally given by the bin width t_{bin}.

As mentioned before, a photoreceiver used as an optical trigger on the LTS screen can not only measure the pulse arrival time at the screen but also the pulse form including the optical peak power and the pulse width. These parameters are required to create the emulated pulse form emitted by the LTS sources. The LTS must emit pulses with the same form or at least the same pulse width. The optical peak power is used for the calculation of the reflected optical power considering the virtual target distance and target reflectance. Furthermore, the aperture diameter of the LiDAR system must be known, which can be measured at a lens or could even be read from the label of a lens system. Apart from that, only properties from the known LTS sources are required for the optical power calculation of the virtual target reflections.

4.7 Demonstrator

A demonstrator of a one-channel LTS has been constructed as shown in Figure 4.14, which is designed to test one pixel of a LiDAR system. The LiDAR system in front

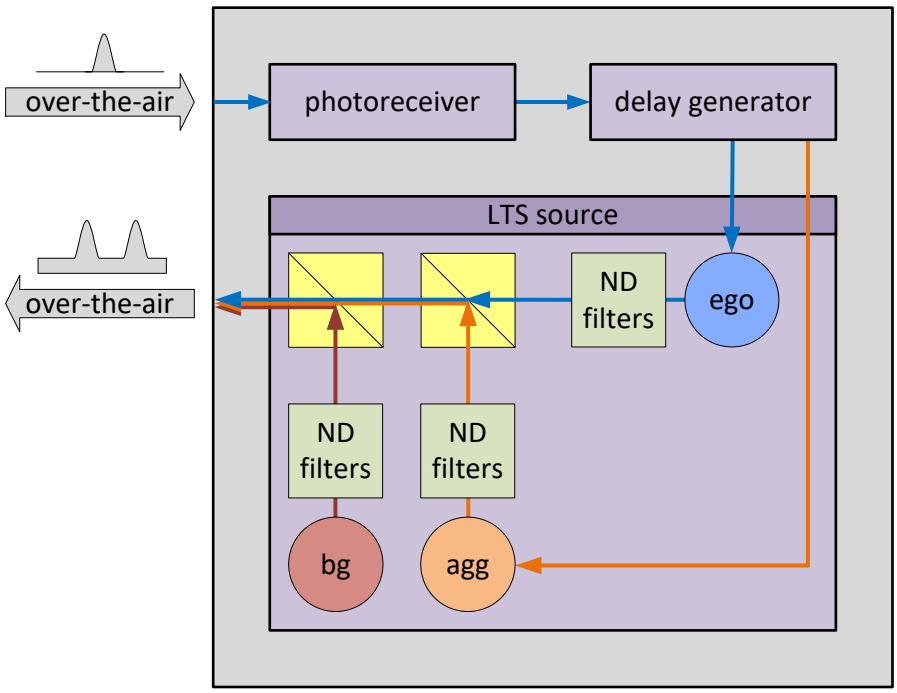

Figure 4.14: Setup of a one-channel LTS demonstrator with TOF setting by a delay generator and optical power setting by ND filters. The generated scenarios based on a virtual target can be emulated by three lasers representing a reflected ego pulse (ego), reflected interfering aggressor pulse (agg) and reflected continuous background light (bg).

of this one-channel LTS can theoretically be moved so that every LiDAR pixel can be tested successively by this demonstrator if desired. For a multi-channel LTS, the hardware would have to be scaled up. In this work, interference is tested for a single pixel. If the potential problem of interference can already be solved on the level of a pixel, it will also be no problem for the total LiDAR detector.

4.7.1 Hardware Setup

The hardware setup of the LTS demonstrator is shown in Figure 4.15. This LTS is designed to test LiDAR system *Owl* from section 2.1.4. As the optical trigger, a photoreceiver with photodiode with a bandwidth up to 1.4 GHz has been used [110]. It has three lasers. The first pulsed laser (ego) emulates the reflected laser pulse of the ego LiDAR system, which is under test. The second pulsed laser (egg) emulates interfering aggressor pulses, which can either represent target reflections producing

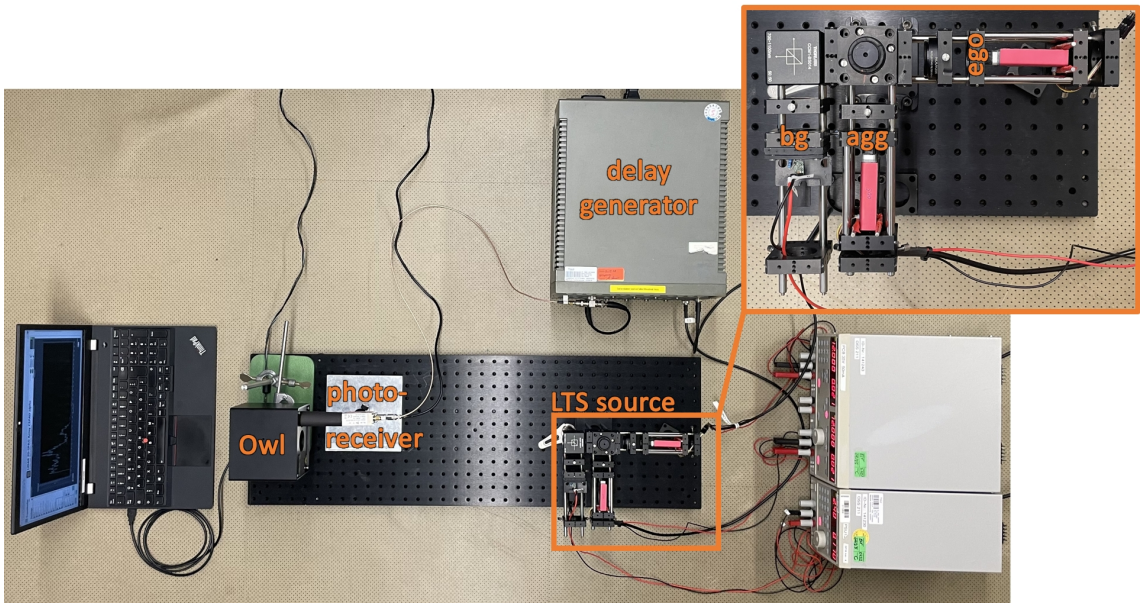

Figure 4.15: Hardware realization of the one-channel LTS demonstrator as illustrated in Figure 4.14 testing LiDAR system *Owl*

indirect interference or a direct light source causing direct interference at the LiDAR system depending on the adjusted optical power. For these two pulsed lasers, the same laser type *LS9-220-8-S10* was used as built into the LiDAR system *Owl* so that the pulse width is the same [39]. The third laser (bg) is a CW laser of type *QL90O7SA* used with laser driver *LSC-030*, which provides a wavelength of 905 nm and maximum power of 100 mW distributed over a solid angle of $20° \times 9°$, which emulates the continuous background light [111][112]. These three lasers are combined by two beam splitters to one light beam, which represents one LTS source emitting light to one pixel of the LiDAR system under test. For this single LTS source, no LTS screen was required and the antireflective screen concept from section 4.4.4 was not realized. Alternatively, the photoreceiver has been placed as close as possible in front of the LiDAR system and a lightproof corridor consisting of a black cardboard roll has been installed from this LiDAR system to the photoreceiver. For the scenario generation, the desired TOF is adjusted by a 50 MHz *programmable function generator* of model 8500 from Kontron, which can generate delay steps of 1 ns corresponding to a distance of 15 cm [113]. The optical power of the three lasers is adjusted by ND filters. Several ND filters can be placed in front of each laser to achieve the required optical powers. Different scenarios can be emulated by the LTS.

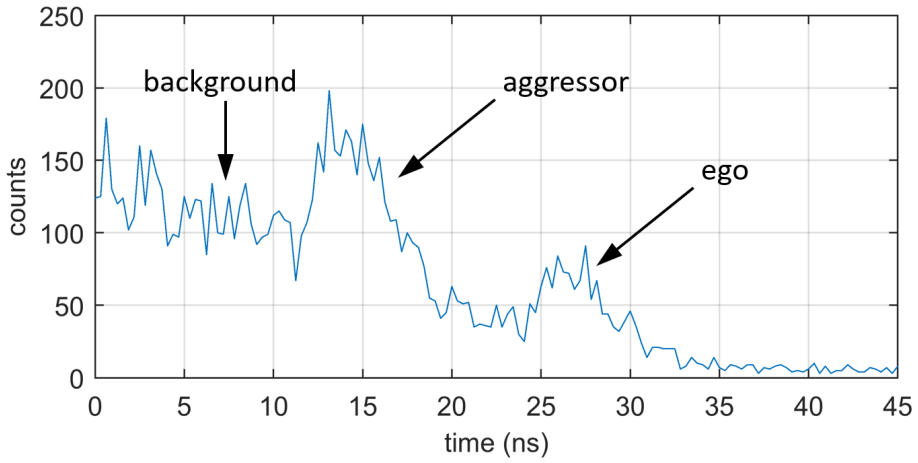

Figure 4.16: Example LiDAR measurement produced by the LTS demonstrator

In Figure 4.16, an emulated scenario is measured by the LiDAR system *Owl*. In the LiDAR histogram, background light can be seen with two laser pulses. Without further knowledge, these two pulses cannot be distinguished but in this case, the first pulse is simulated as aggressor pulse, whereas the second pulse in the histogram represents the ego pulse.

4.7.2 Tuning of Signal-to-Noise Ratio

The LTS demonstrator is designed to generate a broad range of scenarios, which are based on a virtual target with adjustable distance and reflectance. Based on this target, the LTS demonstrator can emulate the reflections of the ego laser pulse, aggressor laser pulse and background light. To characterize the LTS demonstrator, its capability to emulate scenarios over a large parameter space is evaluated in the following. For this purpose, an evaluation metric is required. A common figure of merit is the signal-to-noise ratio (SNR), which can be determined from the measured LiDAR histogram. The various virtual scenarios with different targets can be reduced to LiDAR histograms with specific SNRs. In a measured LiDAR histogram, the SNR indicates the proportion between the detected laser pulse as signal and the fluctuations due to the laser pulse itself and due to the background distribution as noise. To detect a pulse in the presence of background light, the signal given by the pulse must be higher than the noise produced by the background and by laser fluctuations. Therefore, the minimum SNR value required by a LiDAR system to determine the target distance from a histogram evaluates the performance of a LiDAR

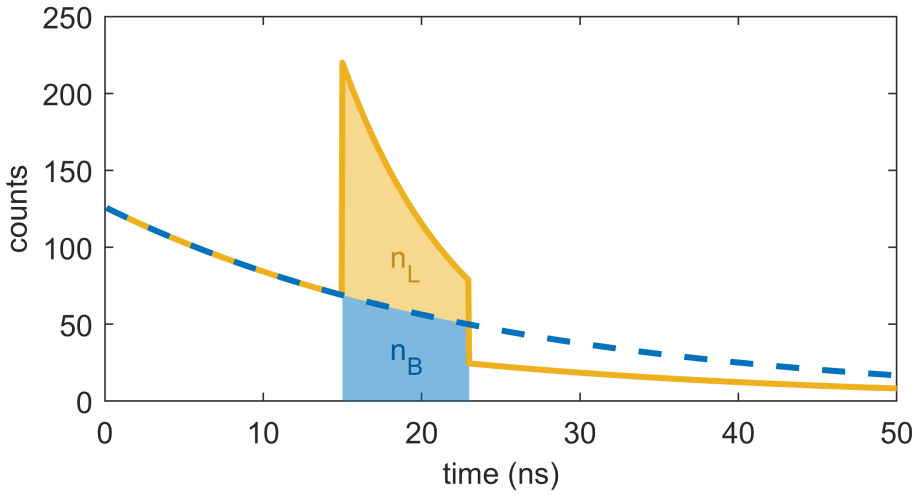

Figure 4.17: SNR determination by the number of laser photons n_L and the number of background photons n_B detected in the histogram during the laser pulse width

system. An LTS can provide the possibility to figure out this performance limit by tunable SNRs values. Furthermore, the determination of minimum SNR values for multiple LiDAR systems by the same repeatable scenarios of an LTS enables the benchmarking of these LiDAR systems.

For the determination of the SNR, the signal and noise must be determined as illustrated in Figure 4.17. The evaluable signal in histograms required for the SNR calculation is given by the number of detected laser photons n_L in the histogram. The noise in the SNR determination is given by the fluctuations of background and laser photons, which can be added as RMS to a combined fluctuation. The SNR k_SN as proportion of signal and noise is calculated by

$$k_\mathrm{SN} = \frac{n_\mathrm{L}}{\sqrt{\sigma_\mathrm{L}^2 + \sigma_\mathrm{B}^2}} = \frac{n_\mathrm{L}}{\sqrt{n_\mathrm{B} + n_\mathrm{L}}}, \tag{4.34}$$

where the uncertainties of laser and background are simply given by $\sigma_\mathrm{L} = \sqrt{n_\mathrm{L}}$ and $\sigma_\mathrm{B} = \sqrt{n_\mathrm{B}}$ according to Poisson statistics [52]. For the theoretical case of known target properties, the number of laser and background photons in the histogram can be theoretically derived by the event rate calculation as explained in section 2.2. For real LiDAR measurements, only the measured LiDAR histogram is available, from which the SNR can be determined. As it is difficult to determine the laser-generated event rates from a histogram, a different SNR determination than the theoretical one is developed. Both methods for SNR determination are presented in the following by the example of one detected laser pulse without interference.

The statistical modeling and SNR determination for histograms containing multiple pulses is described in the next chapter. After that, the behavior of SNR values from the histograms emulated by the LTS demonstrator are compared with the properties of the theoretically determined SNR.

SNR Determination from Theory

For the SNR determination, the number of laser photons n_L in the histogram is required but with increasing background light, the number of detected laser photons in the histogram is reduced. The maximum signal width of the laser in the histogram is given by the pulse width. Due to pile-up effects, the pulse width in the histogram is often narrower than the pulse width emitted by the laser, but potentially laser photons can be found over the total pulse width so that the total pulse width must be considered. The influencing number of background photons n_B is given by the background light during the pulse width. To determine the SNR, the PDF in (2.26) as theoretical event distribution with calculated laser-generated event rate r_L and background-generated event rate r_B can be used. First, the number of background photons n_B is calculated by the integration starting from the TOF t_TOF over the pulse width t_p in a histogram without laser resulting in

$$n_\mathrm{B} = n_\mathrm{meas} \int_{t_\mathrm{TOF}}^{t_\mathrm{TOF}+t_\mathrm{p}} P(t)|_{r_\mathrm{L}=0}\,\mathrm{d}t = n_\mathrm{meas}\left(1-\mathrm{e}^{-r_\mathrm{B}t_\mathrm{p}}\right)\mathrm{e}^{r_\mathrm{B}t_\mathrm{TOF}}, \tag{4.35}$$

where n_meas is the number of measurements for this histogram. The number of laser photons n_L is calculated by the total number of photons minus the number of background photons n_B with

$$n_\mathrm{L} = n_\mathrm{meas} \int_{t_\mathrm{TOF}}^{t_\mathrm{TOF}+t_\mathrm{p}} P(t)\mathrm{d}t - n_\mathrm{B} = n_\mathrm{meas}\left(\mathrm{e}^{-r_\mathrm{B}t_\mathrm{p}} - \mathrm{e}^{-(r_\mathrm{B}+r_\mathrm{L})t_\mathrm{p}}\right)\mathrm{e}^{-r_\mathrm{B}t_\mathrm{TOF}}. \tag{4.36}$$

Inserting both in (4.34), the SNR can be determined from the theoretical PDF to

$$k_\mathrm{SN} = \sqrt{n_\mathrm{meas}\mathrm{e}^{-r_\mathrm{B}t_\mathrm{TOF}}}\frac{\mathrm{e}^{-r_\mathrm{B}t_\mathrm{p}} - \mathrm{e}^{-(r_\mathrm{B}+r_\mathrm{L})t_\mathrm{p}}}{\sqrt{1-\mathrm{e}^{-(r_\mathrm{B}+r_\mathrm{L})t_\mathrm{p}}}} \approx \sqrt{n_\mathrm{meas}t_\mathrm{p}\mathrm{e}^{-r_\mathrm{B}t_\mathrm{TOF}}}\frac{r_\mathrm{L}}{\sqrt{r_\mathrm{B}+r_\mathrm{L}}}, \tag{4.37}$$

which can be approximated for small values of $r_\mathrm{B} \ll t_\mathrm{p}^{-1}$ and $(r_\mathrm{B}+r_\mathrm{L}) \ll t_\mathrm{p}^{-1}$. The comparison of (4.34) with the approximated form of (4.37) shows that the number of laser and background photons in a histogram approximately correspond to the laser- and background-generated event rate.

SNR Determination from Measurements

In measured LiDAR histograms, the laser pulse can be seen as well, but it is difficult to determine the laser-generated event rate r_L so that the SNR is calculated differently to the theoretical determination presented in the previous section. From the measured histogram, the number of laser and background photons for (4.34) can be determined as developed in the following.

First, the background intensity must be known. For this purpose, a LiDAR histogram with pure background with switched-off or covered laser. From the exponential background distribution in the histogram, the background-generated event rate can be determined by a maximum likelihood estimator considering the histogram length t_hist as finite observation time. The resulting estimated background-generated event rate $\hat{r}_\mathrm{B}$ is given by

$$\hat{r}_\mathrm{B} = \frac{\sum_{i=1}^{n_\mathrm{bin}} n_i}{\sum_{i=1}^{n_\mathrm{bin}} n_i \cdot i \cdot t_\mathrm{bin} + \left(n_\mathrm{meas} - \sum_{i=1}^{n_\mathrm{bin}} n_i \right) \cdot t_\mathrm{hist}}, \tag{4.38}$$

where n_i are the counts in the i-th bin with bin width t_bin and n_bin is the number of bins in the histogram. The first term in the denominator represents the reciprocal of all photon arrival times in the histogram. The second term in the denominator describes the number of undetected photons, which arrive at the LiDAR detector at times larger than the finite histogram length t_hist. Therefore, the number of detected photons in the histogram is only $n_\mathrm{meas} - \sum_{i=1}^{n_\mathrm{bin}} n_i$, although n_meas measurements have been performed for this histogram. With the estimated background-generated event rate $\hat{r}_\mathrm{B}$, the expected exponential background distribution in the histogram is given by the PDF in (2.26) without laser-generated event rate $P(t)|_{r_\mathrm{L}=0}$.

The number of background photons n_B influencing the detected laser signal is determined by the sum of all counts in the bins from t_TOF to $t_\mathrm{TOF} + t_\mathrm{p}$ that are below the estimated exponential background distribution. All other counts of the same bins above this exponential background distribution are assumed to be laser photons n_L. With the known numbers of background and laser photons, the SNR can be determined by (4.34). For this SNR determination, uncertainty propagation is applied, which is based on the measurement uncertainty $\sqrt{n_i}$ for each bin i with n_i counts [52]. With the presented method, SNR values and their uncertainties can be determined from measured histograms without previous knowledge.

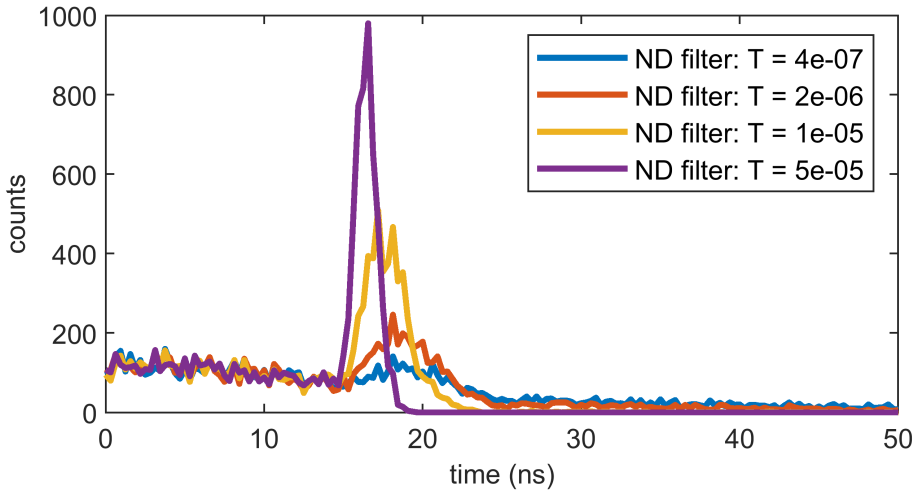

Figure 4.18: Example Histograms with number of measurements $n_{\text{meas}} = 10000$ and adjusted TOF $t_{\text{TOF}} = 15\,\text{ns}$, background-generated event rate of 40 MHz and multiple laser-generated event rates produced by different ND filter transmissions T

SNR Scenario Generation by LTS Demonstrator

The LTS is designed to emulate scenarios with different SNR values addressing different difficulty levels for the LiDAR system. Most traffic scenarios can be reduced to abstract scenarios with defined t_{TOF} and specific SNR symbolizing the optical power of a scenario due to target distance and target reflectance. With the LTS demonstrator, several histograms with different SNR values are conducted with LiDAR system *Owl* with number of measurement $n_{\text{meas}} = 10000$ and an adjusted TOF $t_{\text{TOF}} = 15\,\text{ns}$, from which example histograms are shown in Figure 4.18. For each histogram, the SNR value is determined as described in the previous section. From the Maximum likelihood estimator, the adjusted background-generated event rates r_{B} are obtained, which are the three background levels 8 MHz, 20 MHz and 40 MHz. The laser-generated event rate r_{L} is still unknown, but the relative optical laser power changes between the histograms can be indicated because the applied ND filter transmission of each histogram is known. All determined SNR values from the measured histograms are shown in Figure 4.19 with the corresponding ND filter transmission representing the relative laser-generated event rate.

To verify the SNR behavior measured by the LTS demonstrator, the measured SNR course is compared with the theoretical SNR course according to (4.37). For this purpose, the measured SNR values are fitted to the theoretical prediction with

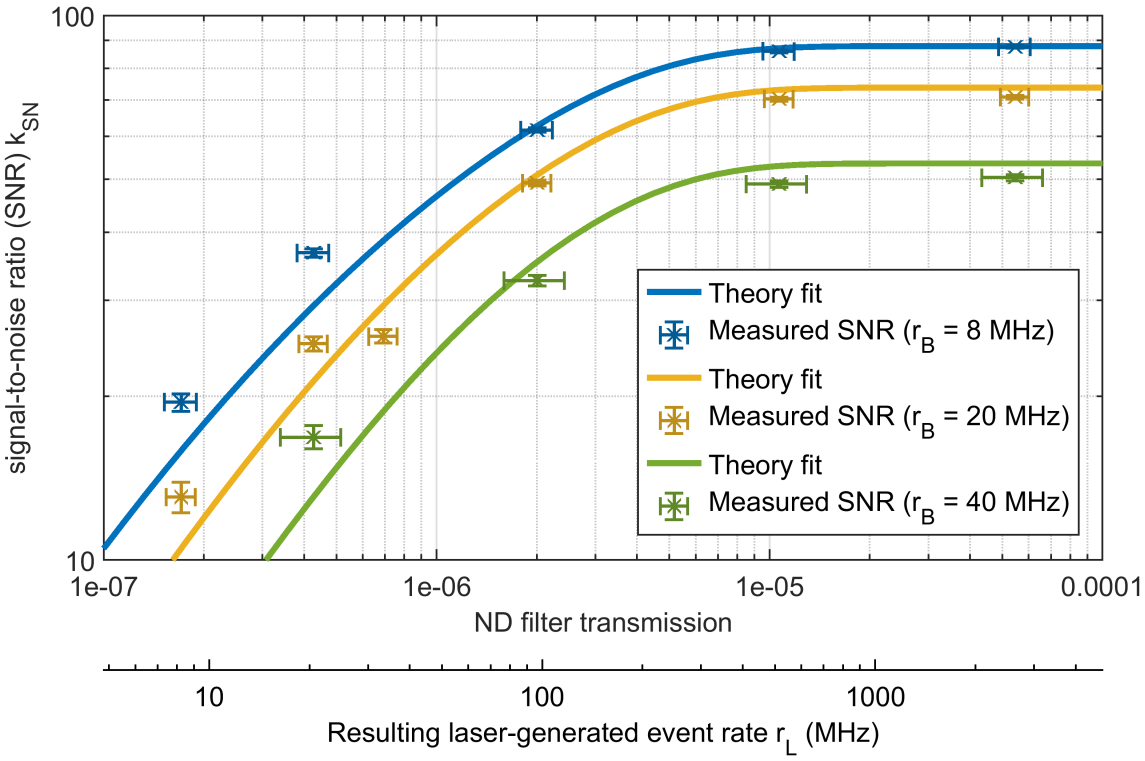

Figure 4.19: SNR values measured from different scenarios emulated by the LTS demonstrator and theory fits with inserted common laser-generated event rate $r_{L,0} = 4.8 \cdot 10^{13}$ Hz given without any ND filter (transmission $T = 100\,\%$) averaged from the three fits

the only unknown parameter of the laser-generated event rate $r_{L,0}$ given without any ND filters, which is equivalent to a transmission of 100 %. Multiplying this event rate $r_{L,0}$ to an applied ND filter transmission, provides the respective laser-generated event rate r_L produced by these ND filters. The fit of the SNR equation can be successfully applied and as a result, the laser-generated event rate $r_{L,0}$ can be determined. For each of the three background levels, approximately the same laser-generated event rate without any ND filter $r_{L,0}$ is obtained with $(5.4 \pm 0.6) \cdot 10^{13}$ Hz, $(4.6 \pm 0.4) \cdot 10^{13}$ Hz and $(4.4 \pm 0.9) \cdot 10^{13}$ Hz. The mean value of these three fitting results $r_{L,0} = 4.8 \cdot 10^{13}$ Hz is inserted as a common parameter in all fitted curves, which are shown in Figure 4.19. To indicate the individual uncertainty of each fit, the relative fitting error of each resulting laser-generated event rate $r_{L,0}$ is shown. The applied ND filter transmissions seen in the first x-axis are transformed into the corresponding laser-generated event rates r_L in the second x-axis by multiplying the averaged laser-generated event rate $r_{L,0}$ to the ND filter transmissions. Especially

with regards to the susceptible exponential dependencies in (4.37) and the large range of measured laser-generated event rates r_{L}, it can be concluded that the theoretical SNR function agrees well with the courses of the measured SNRs for each background level.

Finally, it can be shown that the LTS is able to emulate scenarios with different SNR values, which represent traffic scenarios with different optical power resulting from the chosen target distance and target reflectance. The generated SNR values agree with the theory. The experimental SNR value determination is even suitable for the determination of the laser-generated event rate r_{L} so that this parameters is known for future LTS measurements. The achieved maximum event rates are 40 MHz for the background and in the order of 10^{13} Hz for the laser. For the optical power adjustment, ND filters are used so that only discrete optical powers can be set but over this large range. For an optimal LTS design, light sources with continuous optical power adjustment can be chosen. In the following, the LTS demonstrator can be used to emulate interference scenarios using different background levels and different ego as well as aggressor pulses with adjustable positions and heights of their signatures in LiDAR histograms.

Chapter 5

Recognition of Interference

When the conditions in chapter 3 are fulfilled and LiDAR interference occurs, the LiDAR system does not necessarily recognize the present interference. To evaluate the recognition potential, the influence of interference on the measured LiDAR histogram is evaluated in the following.

5.1 Impacts of LiDAR Interference on Histograms

In the presence of LiDAR interference, not only one pulse is seen in a histogram, but multiple pulses can occur depending on the number of interfering systems. For example, in Figure 5.1, the ego and the aggressor LiDAR system produce two pulses in a histogram measured by the ego system. Without further information, it is unknown whether the first or the second pulse in the histogram is the ego pulse. In the following, the histograms affected by interference are analytically described.

5.1.1 Event Rates Generated by Interfering Laser

In section 2.2, the event rates generated by the ego laser pulse and background light reflected from a target have been derived. In this section, the event rates generated by direct or indirect interference caused by an aggressor laser are investigated. For direct interference, there is no target reflection involved. Instead, the aggressor illuminates the LiDAR aperture directly. For both interference types, the size of the LiDAR aperture determines the amount of the obtained light. Less light is received from the Lambertian target reflection than from the aggressor illumination because the Lambertian target illuminates in the total hemisphere, whereas the aggressor

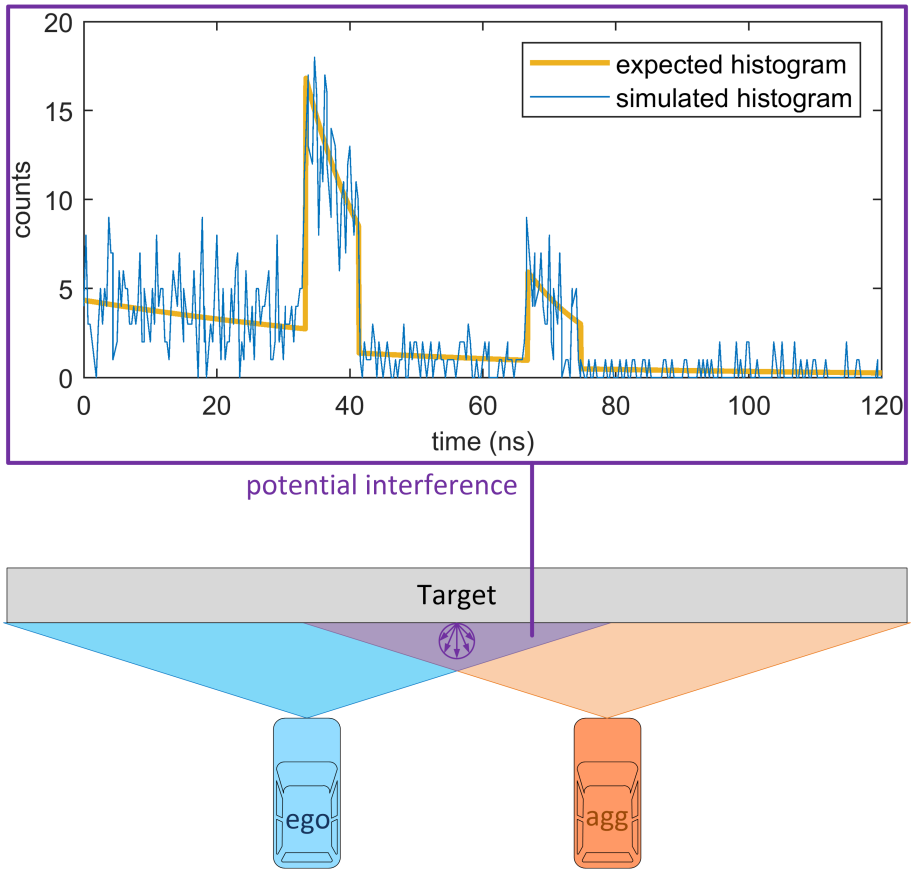

Figure 5.1: Potential interference between two LiDAR systems (ego system and aggressor system) can produce two laser pulses in the measured LiDAR histogram.

illuminates a smaller FOI corresponding to the aggressor FOV. Assuming that the aggressor illuminates a homogeneous rectangular area $A_{\text{target,agg}}$, the intensity factor becomes

$$a_{\text{direct}} = \frac{\pi \left(\frac{D}{2}\right)^2}{A_{\text{illum,agg}}} \approx 10^{-6}, \tag{5.1}$$

where $D = 10\,\text{mm}$ is the aperture diameter and $d = 10\,\text{m}$ is the distance between ego and aggressor. $A_{\text{illum,agg}}$ is the illuminated target area, which is calculated by (2.12) for an exemplary aggressor FOI of $\theta_{\text{L,H}} \times \theta_{\text{L,V}} = 60° \times 20°$. For indirect interference, the aggressor laser is reflected at a target equivalent to the ego laser. The corresponding intensity factor of indirect interference is the reflection factor η_{refl} in (2.14) resulting in

$$a_{\text{indirect}} = \eta_{\text{refl}} = \rho \left(\frac{D}{2d}\right)^2 \approx 10^{-7}, \tag{5.2}$$

where $\rho = 80\,\%$ is the target reflectance and d is the target distance instead of the distance between both systems. As a result, the illumination from direct interference is more intense than from indirect interference by a factor

$$\frac{a_{\text{direct}}}{a_{\text{indirect}}} = \frac{\pi}{4\rho \tan\left(\frac{\theta_{\text{L,H}}}{2}\right) \tan\left(\frac{\theta_{\text{L,V}}}{2}\right)} \approx 10, \tag{5.3}$$

where the aperture diameter D and distance d canceled out. In conclusion, direct interference causes a higher signal at the ego LiDAR system than indirect interference. However, direct interference affects only a few pixels as described in section 3.2 so that the more dangerous case of indirect interference is assumed in the following.

5.1.2 Statistical Modeling of Histogram Data with Interference

The statistical modeling of a histogram with multiple pulses is based on the PDF for a single pulse as described in section 2.3.1 given by

$$P(t) = \begin{cases} r_{\text{B}} \mathrm{e}^{-r_{\text{B}} t}, & 0 \leqslant t < t_{\text{TOF}} \\ (r_{\text{B}} + r_{\text{L}}) \mathrm{e}^{r_{\text{L}} t_{\text{TOF}}} \mathrm{e}^{-(r_{\text{B}} + r_{\text{L}}) t}, & t_{\text{TOF}} \leqslant t < t_{\text{TOF}} + t_{\text{p}} \\ r_{\text{B}} \mathrm{e}^{-r_{\text{L}} t_{\text{p}}} \mathrm{e}^{-r_{\text{B}} t}, & t_{\text{TOF}} + t_{\text{p}} \leqslant t \end{cases}. \tag{5.2}$$

For the PDF of n_{s} laser pulses in a histogram, each pulse is detected with a specific TOF although the detected TOF of an aggressor pulse is randomly produced and does not correspond to a real target. For simplicity, rectangular pulse forms are used again and all pulses are assumed to be non-overlapping so that the TOFs $t_{\text{TOF,s}},\ s = 1, \ldots, n_{\text{s}}$ are defined in ascending order with

$$t_{\text{TOF,1}} + t_{\text{p}} \leqslant t_{\text{TOF,2}}, \ldots, t_{\text{TOF,}n_{\text{s}}-1} + t_{\text{p}} \leqslant t_{\text{TOF}}. \tag{5.3}$$

It is still assumed that the interfering LiDAR systems are equal, resulting in equal pulse widths t_{p}. For indirect interference, the LiDAR systems must observe the same target with the same target reflectance. However, the target distances can be different so that every LiDAR system can detect a different laser-generated event rate $r_{\text{L},i},\ i = 1, \ldots, n_{\text{s}}$ from the same target. Due to the pile-up effect of the first-photon measurement principle, early arriving photons reduce the probability to detect later photons [114]. This problem is well-known from the behavior of background light,

which reduces a laser pulse in the histogram particularly if the pulse arrives late. In the same way, every pulse in the histogram reduces the detection probability of all pulses afterwards. The s-th pulse in a histogram is reduced by the previous background as already seen in (5.2) and also by all previous pulses $i = 1, \ldots, s-1$. The PDF $P(t|n_\mathrm{s})$ with all pulses has a complex form given by

$$
P(t|n_\mathrm{s}) = \begin{cases}
r_\mathrm{B} \mathrm{e}^{-r_\mathrm{B} t}, & 0 \leqslant t < t_{\mathrm{TOF},1} \\
(r_\mathrm{B} + r_{\mathrm{L},1}) \mathrm{e}^{r_{\mathrm{L},1} t_{\mathrm{TOF},1}} \mathrm{e}^{-(r_\mathrm{B} + r_{\mathrm{L},1}) t}, & t_{\mathrm{TOF},1} \leqslant t < t_{\mathrm{TOF},1} + t_\mathrm{p} \\
r_\mathrm{B} \mathrm{e}^{-r_{\mathrm{L},1} t_\mathrm{p}} \mathrm{e}^{-r_\mathrm{B} t}, & t_{\mathrm{TOF},1} + t_\mathrm{p} \leqslant t < t_{\mathrm{TOF},2} \\
\vdots & \vdots \\
(r_\mathrm{B} + r_{\mathrm{L},s}) \left(\prod_{i=1}^{s-1} \mathrm{e}^{-r_{\mathrm{L},i} t_\mathrm{p}} \right) \mathrm{e}^{r_{\mathrm{L},s} t_{\mathrm{TOF},s}} \mathrm{e}^{-(r_\mathrm{B} + r_{\mathrm{L},s}) t}, & t_{\mathrm{TOF},s} \leqslant t < t_{\mathrm{TOF},s+1} + t_\mathrm{p} \\
r_\mathrm{B} \left(\prod_{i=1}^{s} \mathrm{e}^{-r_{\mathrm{L},i} t_\mathrm{p}} \right) \mathrm{e}^{-r_\mathrm{B} t}, & t_{\mathrm{TOF},s} + t_\mathrm{p} \leqslant t < t_{\mathrm{TOF},s} \\
\vdots & \vdots \\
(r_\mathrm{B} + r_{\mathrm{L},n_\mathrm{s}}) \left(\prod_{i=1}^{n_\mathrm{s}-1} \mathrm{e}^{-r_{\mathrm{L},i} t_\mathrm{p}} \right) \mathrm{e}^{r_{\mathrm{L},n_\mathrm{s}} t_{\mathrm{TOF},n_\mathrm{s}}} \mathrm{e}^{-(r_\mathrm{B} + r_{\mathrm{L},n_\mathrm{s}}) t}, & t_{\mathrm{TOF},n_\mathrm{s}} \leqslant t < t_{\mathrm{TOF},n_\mathrm{s}} + t_\mathrm{p} \\
r_\mathrm{B} \left(\prod_{i=1}^{n_\mathrm{s}-1} \mathrm{e}^{-r_{\mathrm{L},i} t_\mathrm{p}} \right) \mathrm{e}^{-r_\mathrm{B} t}, & t_{\mathrm{TOF},n_\mathrm{s}} + t_\mathrm{p} \leqslant t < t_{\mathrm{TOF},n_\mathrm{s}}
\end{cases} \cdot \tag{5.4}
$$

The reduction of a pulse signature by the previous pulse signals is given by the products iterating over the laser-generated event rates of all previous pulses. These are the only places in the equation where the pulse width t_p appears, which is multiplied to the laser-generated event rates. This mathematical construction allows to easily generalize the PDF to different LiDAR system types if desired, by inserting individual pulse widths $t_{\mathrm{p},i},\ i = 1, \ldots, n_\mathrm{s}$ instead of the fixed pulse width t_p. Conversely, a few assumptions can produce a strongly simplified form of the PDF as shown in (5.5), where only two laser signals $n_\mathrm{s} = 2$ from two LiDAR systems are assumed in the histogram and the same target distances are applied leading to

identical laser-generated event rates for all laser signals.

$$P(t|n_\mathrm{s}=2) = \begin{cases} r_\mathrm{B}\mathrm{e}^{-r_\mathrm{B}t}, & 0 \leqslant t < t_\mathrm{TOF,1} \\ (r_\mathrm{B}+r_\mathrm{L})\mathrm{e}^{r_\mathrm{L}t_\mathrm{TOF,1}}\mathrm{e}^{-(r_\mathrm{B}+r_\mathrm{L})t}, & t_\mathrm{TOF,1} \leqslant t < t_\mathrm{TOF,1}+t_\mathrm{p} \\ r_\mathrm{B}\mathrm{e}^{-r_\mathrm{L}t_\mathrm{p}}\mathrm{e}^{-r_\mathrm{B}t}, & t_\mathrm{TOF,1}+t_\mathrm{p} \leqslant t < t_\mathrm{TOF,2} \\ (r_\mathrm{B}+r_\mathrm{L})\mathrm{e}^{-r_\mathrm{L}t_\mathrm{p}}\mathrm{e}^{r_\mathrm{L}t_\mathrm{TOF,2}}\mathrm{e}^{-(r_\mathrm{B}+r_\mathrm{L})t}, & t_\mathrm{TOF,2} \leqslant t < t_\mathrm{TOF,2}+t_\mathrm{p} \\ r_\mathrm{B}\mathrm{e}^{-r_\mathrm{L}t_\mathrm{p}}\mathrm{e}^{-r_\mathrm{B}t}, & t_\mathrm{TOF,2}+t_\mathrm{p} \leqslant t < t_\mathrm{TOF,2} \end{cases} \tag{5.5}$$

For the expected count distribution in the measured histogram, the PDF must be integrated over the bin widths t_bin and multiplied by the number of measurements per histogram n_meas, which can be approximated by the multiplication factor of $n_\mathrm{meas}t_\mathrm{bin}$. The simulation of a histogram works similar as explained in section 2.3.2. For each laser pulse, a laser photon arrival time is generated. To determine the detected first photon, the earliest photon of these arrival times and the generated background arrival time is selected. For multiple laser pulses, the expected histogram based on the PDF and the simulated histogram again match very well as seen in Figure 5.1.

5.1.3 Synchronicity of LiDAR Systems

Under the assumption that the ego and aggressor systems operate at the same or multiples of the same frequency, their laser signals accumulate in the ego histogram. For flash LiDAR, the operating frequency is equivalent to the laser PRF because after each laser pulse emission, every pixel performs a measurement. LiDAR systems can have a very high time precision, which is required to achieve a good distance resolution with regards to the high speed of light. Therefore, small deviations in the laser PRF of ego and aggressor system might influence the accumulation of their laser signals in the ego histogram. An example measurement with two separate LiDAR systems *Owl* placed opposite to each other is shown in Figure 5.2, where the ego laser is switched off and the aggressor laser signal in the ego histogram is smeared and distributed over a large range of bins. No bin contains more than a single photon detection and there are one to four empty bins between these single counts so that a pulse train is seen in the histogram, which seems to run out of the histogram. Although the ego and aggressor system have the same nominal laser PRFs of 10 kHz, their actual frequencies detected by the ego system seem to be

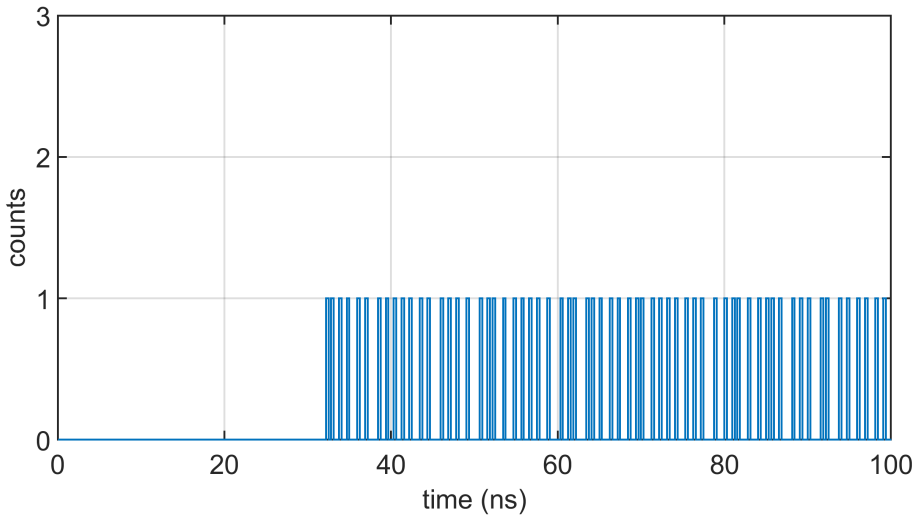

Figure 5.2: Histogram measured by LiDAR system *Owl* with switched-off ego laser observing the aggressor signal from another asynchronously running LiDAR system *Owl* with the same nominal laser PRF of 10 kHz

slightly different.

One reason for frequency deviations can be the manufacturer tolerance of LiDAR system components. The frequency of a LiDAR system is provided by an oscillator, which can for example pass it as clock to a field programmable gate array (FPGA). Depending on the quality of the oscillator, the manufacturer tolerance of the frequency can vary. There are oscillators with frequency stabilities ranging from 0.1 ppm to 500 ppm [115]. Especially Quartz oscillators have a high frequency stability. As example, the standard oscillator *ASEM1-100.000MHZ-LC-T* with 100 MHz is investigated [116]. The cycle-to-cycle jitter is only 60 ps at a frequency of 100 MHz, which is for example smaller than a bin width of LiDAR system *Owl* so that it can be neglected. The frequency stability is 100 ppm. If the LiDAR system requires a nominal laser frequency of $f_\mathrm{p} = 10\,\mathrm{kHz}$, the upscaled uncertainty would thus be $\Delta f_\mathrm{p} = 1\,\mathrm{Hz}$. This deviation of the nominal frequency f_p can be transferred from the frequency into the time domain as time uncertainty Δt given by

$$\Delta t = \frac{1}{f_\mathrm{p}} - \frac{1}{f_\mathrm{p} + \Delta f_\mathrm{p}} \approx \frac{\Delta f_\mathrm{p}}{f_\mathrm{p}^2}, \tag{5.6}$$

which can be approximated, because the deviation is small compared with the nominal frequency resulting in $\Delta f_\mathrm{p} \ll f_\mathrm{p}$. For the previous example values, the time uncertainty becomes $\Delta t = 10\,\mathrm{ns}$. Considering the bin width $t_\mathrm{bin} = 0.3125\,\mathrm{ns}$ of LiDAR system *Owl*, this uncertainty is equivalent to 32 bins so that this time dif-

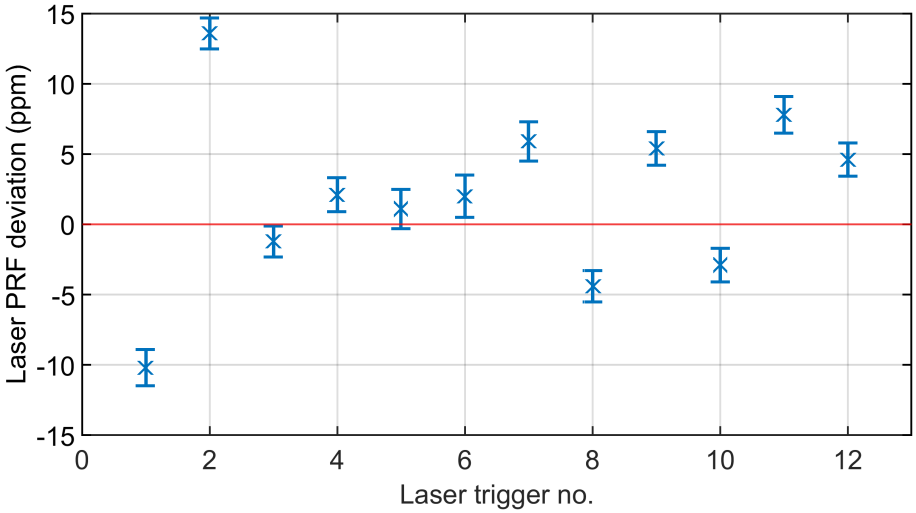

Figure 5.3: Measurement of actual laser PRF deviation for a nominal laser PRF of 10 kHz (at 0 ppm) given by 12 laser triggers of LiDAR system *Owl*

ference can be identified in the histogram. The oscillator of LiDAR system *Owl* provides a nominal frequency of 33 MHz, but the frequency stability is unknown so that it is determined by measurements [117]. Using an oscilloscope, the laser trigger frequency is measured at 12 identical laser triggers of identical LiDAR systems *Owl*, where a nominal laser frequency of 10 kHz is set. The resulting frequencies are shown in Figure 5.3. The measured average frequency is 10.000 02 kHz. The cycle-to-cycle jitter of each system is seen as an error bar representing the standard deviation of the measured laser PRF. This jitter is in the order of 100 ps, which is smaller than the bin width and hence can be neglected. Choosing for example the LiDAR systems with laser trigger no. 6 and 8, the frequency difference is about 6 ppm with regards to the nominal frequency of 10 kHz. This corresponds to a time deviation of 0.6 ns according to (5.6), which is in the order of two bins with bin width $t_{\text{bin}} = 0.3125$ ns of LiDAR system *Owl* and thus expected to be seen in the histogram.

Another reason for different ego and aggressor frequencies received at the ego system, can be a relative velocity of the aggressor system to the ego system. For example, for direct interference, two vehicles on opposite lanes approaching each other can be assumed. If both vehicles drive with the same velocity of 130 km/h, the distance between them is shortened between two consecutive measurements proportional to their relative velocity $v = 260$ km/h. This distance corresponds to a

time shift Δt according to (2.1) after each single measurement of

$$\Delta t = \frac{2 \cdot v}{c \cdot f_\mathrm{p}} = 0.05\,\mathrm{ns}, \tag{5.7}$$

where c is the speed of light and $f_\mathrm{p} = 10\,\mathrm{kHz}$ is the laser PRF. Compared to the laser PRF deviation of the LiDAR system with trigger no. 6 and 8 with about $\Delta t = 6\,\mathrm{ns}$, the time shift caused by the velocity of the LiDAR systems is small. However, assuming 1000 measurements per histogram, the total time shift due to the relative velocity becomes 50 ns corresponding to 160 bins, which is recognizable in the histogram. For indirect interference, the relative velocity between the ego or aggressor system and the reflecting target is relevant. As this distance can affect the ego and aggressor signal equally, the LiDAR system velocity generally provides no information to distinguish the ego and aggressor signal in the histogram. Only if further information is given like a radar system measurement of the relative velocity between ego system and target, the corresponding pulse in the histogram might be identified as the ego pulse. In the following, the received signals at the ego system generated by consecutive ego and aggressor pulses are discussed.

The arrival times of the ego pulses obtained by the ego system are unaffected by frequency uncertainties of the ego system because the system will trigger the laser emission and the measurement start by the same clock. Uncertainties in the absolute operating frequency would affect both timings equally so that they run synchronously with each other. In contrast to that, the aggressor system can have a slightly different laser PRF, but the aggressor laser pulses would still be measured by the ego system triggering the measurement start with its own frequency. If ego and aggressor system are assumed to have frequency deviations in the order of 6 ppm corresponding to two bins with bin width t_bin like the measured laser trigger no. 6 and 8, the obtained aggressor signals will move from measurement to measurement, whereas the ego signal remains and accumulates. This effect is shown in Figure 5.4. The combined signal represents all signals from 40 consecutive single measurements. The form of the combined aggressor signal has changed compared with the rectangular ego signal form due to the frequency deviation Δf corresponding to a time difference Δt of two consecutive emitted pulses. The original aggressor pulse width t_p is obtained by the ego system with a different combined aggressor signal width w_agg given by

$$w_\mathrm{agg} = t_\mathrm{p} + n_\mathrm{meas} \cdot \Delta t = 33\,\mathrm{ns}, \tag{5.8}$$

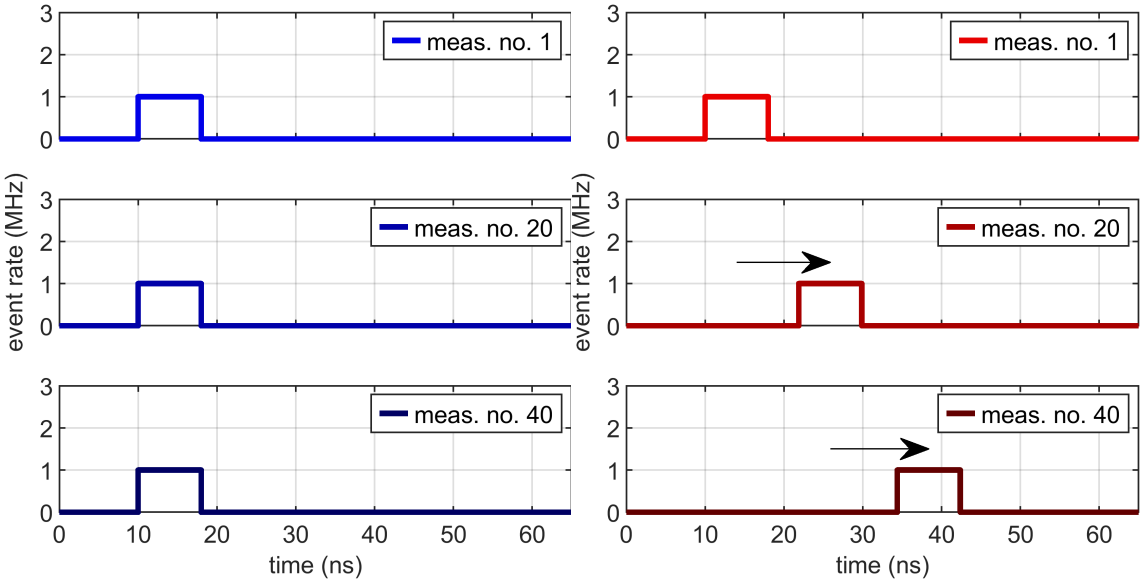

(a) Signal of single measurement: ego signal (b) Signal of single measurement: aggressor signal

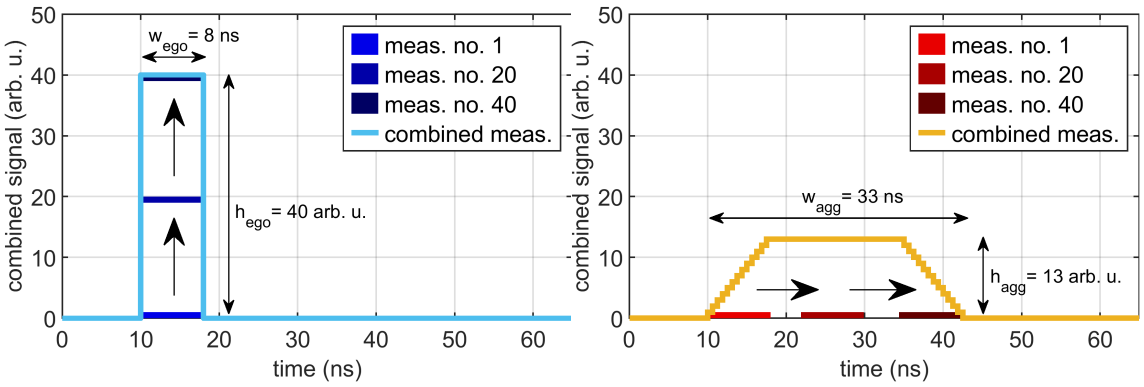

(c) Combined signal: ego signal (d) Combined signal: aggressor signal

Figure 5.4: Signal of consecutive ego and aggressor pulses obtained by the ego system, each with a laser-generated event rate of $r_\mathrm{L} = 1\,\mathrm{MHz}$. The combined aggressor signal of all measurements has a larger signature width than the combined ego signal that accumulates at the same position. The laser PRF of the aggressor system deviates by about 6 ppm from the ego PRF of 10 kHz corresponding to a temporal drift of two consecutive aggressor pulses corresponding to two bin widths with $\Delta t = 2 \cdot t_\mathrm{bin} = 0.625\,\mathrm{ns}$ after (5.6).

where the pulse width t_p represents the ego pulse width, n_meas is the number of measurement per histogram and t_bin is the bin width. For the example in Figure 5.4, the combined ego signal in the histogram still has a signal width of 8 ns, whereas the aggressor signal is smeared to a width of 33 ns seen in the histogram after only 40 measurements. The signal height of the combined aggressor signal h_agg becomes

$$h_\mathrm{agg} = \frac{h_\mathrm{ego}}{n_\mathrm{meas}} \cdot \frac{t_\mathrm{p}}{\Delta t} = 13\,\mathrm{arb.u.}, \tag{5.9}$$

which is also seen in the Figure 5.4. The height of the combined ego signal is 40 arb.u., whereas the aggressor signal height becomes only 13 arb.u.. When the shown combined signals of ego and aggressor are received by a LiDAR system with first-photon measurement principle, the photons are detected under the influence of the pile-up effect so that earlier photons are more likely to be detected than later photons. The arrival times of the single aggressor signals change between consecutive single measurements. Therefore, the pile-up effect is not seen by an emphasized beginning of the accumulated aggressor signal form but influences each single aggressor pulse detection with different arrival time individually. From each single aggressor pulse emission, the earliest photons are mainly detected but the arrival time of these early photons drifts continuously. As a result, the pile-up effect emphasizes the drifting beginnings of all different single measurements so that the detected photons are approximately uniformly distributed in the histogram. In Figure 5.4d, the illustrated combined aggressor signal seems to be rather trapezoidal than uniformly distributed due to the small number of measurements $n_\mathrm{meas} = 40$, but it would also look like a uniform distribution for more measurements per histogram. The uniform distribution is seen in the measurement presented in Figure 5.2. As there is maximally one aggressor photon per bin in this measured histogram, the aggressor signal might be treated as noise. However, it should be considered that the appearance of the aggressor photons in the histogram is different than the noise caused by background photons, which are not uniformly but exponentially distributed in the histogram due to the pile-up effect.

In the following, the worst case of approximately synchronous ego and aggressor system is assumed, where the ego and aggressor PRF produce a time deviation less than the pulse width t_p during the acquisition of all measurements for a histogram, which is assumed with $\Delta f < w_\mathrm{agg} - w_\mathrm{ego}$. According to (5.6) and (5.8), an unsmeared combined aggressor signal similar to the ego signal is received at the ego system for

a maximum frequency deviation Δf_{sync} of the aggressor system given by

$$\Delta f_{\mathrm{sync}} < f_{\mathrm{p}}^2 \cdot \frac{t_{\mathrm{p}}}{n_{\mathrm{meas}}}. \tag{5.10}$$

For example, for LiDAR system *Owl* with a nominal laser PRF of $f_{\mathrm{p}} = 10\,\mathrm{kHz}$, a pulse width of $t_{\mathrm{p}} = 8\,\mathrm{ns}$ and $n_{\mathrm{meas}} = 1000$ measurements per histogram, this maximum frequency deviation becomes $\Delta f_{\mathrm{sync}}/f_{\mathrm{p}} = 0.08\,\mathrm{ppm}$. This frequency deviation is much smaller than the frequency differences of most laser triggers of LiDAR systems *Owl* seen in Figure 5.3. However, such a small frequency difference might be temporarily given during the acquisition of one ego histogram. Afterwards, the ego and aggressor laser PRFs might run apart from each other again. If the actual frequency difference of two LiDAR systems is smaller than the derived frequency deviation Δf_{sync}, the combined aggressor signal will have the same maximum value as the combined ego signal but the shape of the combined aggressor signal will be slightly different with a larger signal width than the still rectangular shape of the expected ego signal. With regards to background light and fluctuations, such a combined aggressor signal can look similar to the ego pulse detected in the histogram so that both signals might be indistinguishable. In this case, the aggressor signal can be mistaken for the ego signal. For simplicity, the following calculations and simulations are performed with even fully identical ego and aggressor signal in the histogram.

5.2 Influence of Interference on Distance Determination

If interference between two synchronous LiDAR systems is assumed, it can appear in a LiDAR histogram as derived in (5.4). The detected pulses can look different than they would appear in a histogram unaffected by interference. These modifications can influence the processed histogram and resulting distance determination as described in section 2.3.3 as well as the considerations about the SNR from section 4.7.2. In the following, the data processing of histograms affected by interference is investigated. Furthermore, the SNR determination for these histograms is derived and the probabilities of photons to be found in the histogram during the pulse width of the ego or aggressor signal are presented.

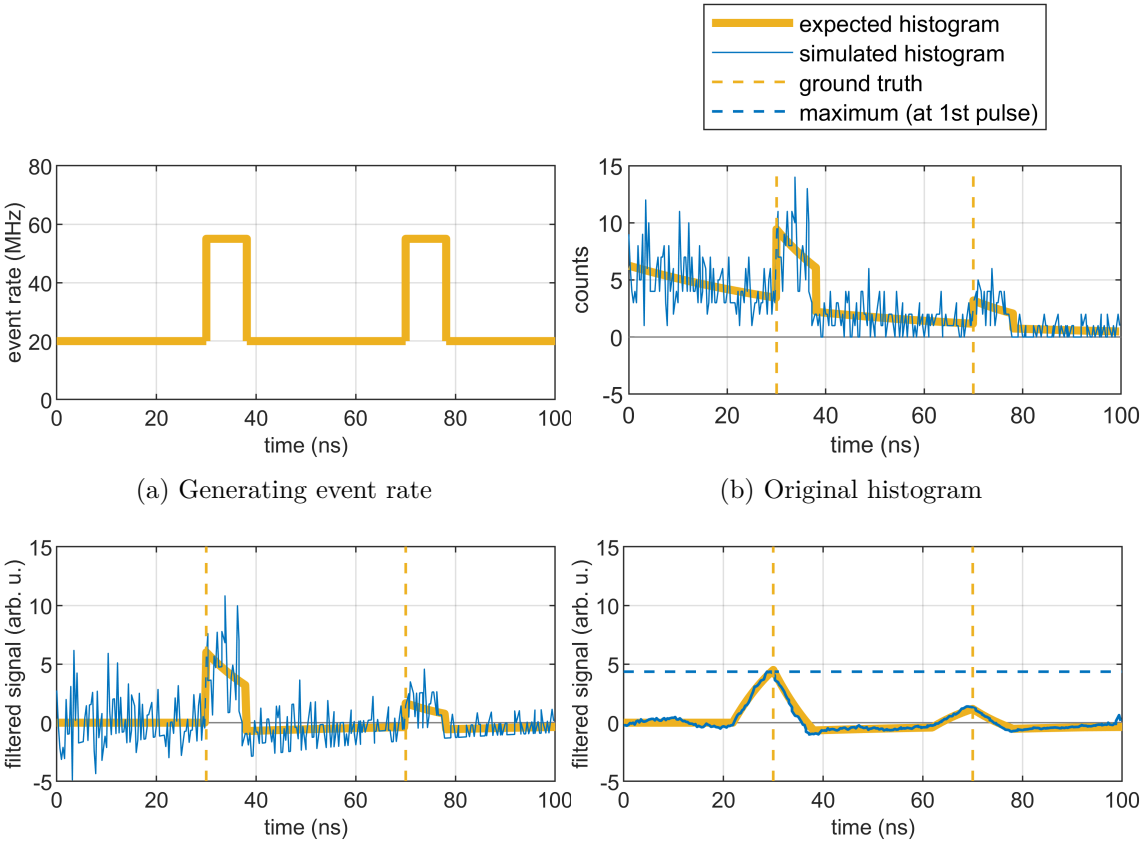

(a) Generating event rate

(b) Original histogram

(c) Background subtraction

(d) Mean filter and maximum detection

Figure 5.5: Data processing of a histogram with two pulses due to LiDAR interference

5.2.1 Histogram Data Processing

As interference influences the histogram data, the distance determination based on the data processing on such a histogram might also be influenced. The influence on the data processing described in section 2.3.3 is discussed now for two detected laser pulses as presented in Figure 5.5. The multiple laser pulses are assumed to be equal producing the same generating event rates at the LiDAR detector as drawn in Figure 5.5a. As seen by the PDF derived previously, these originally equal pulses are obtained with different heights in the LiDAR histogram, which is illustrated in Figure 5.5b. Furthermore, each pulse in the histogram decreases the entire PDF afterwards so that the second pulse beginning drops below the initial exponential background distribution. Before the measurement of the LiDAR histogram, the background-generated event rate r_B is determined, for example by a counting mode

measurement as described in section 2.3.3. Thus, the background subtraction reduces the second pulse additionally as shown in Figure 5.5c. After applying the mean filter, the first laser pulse in the histogram is probably the highest one so that this TOF is chosen to determine the target distance according to (2.1). As it is unknown whether the first or second pulse belongs to the measuring ego LiDAR system, the automatic choice of the first pulse can be dangerous and cause accidents in applications such as autonomous driving.

5.2.2 Signal-to-Noise Ratios and Probabilities of Photons

Although the presented data processing algorithm in the previous section failed, the available signal of every pulse in the histogram might be high enough for a detection. In the following, the SNR determination of section 4.7.2 is expanded on histograms with multiple pulses due to interference. For the evaluation of each pulse height in the histogram, the SNR can be derived bases on the PDF in (5.4) including multiple pulses. Equivalent to the SNR derivation for a single pulse in section 4.7.2, the SNR of the s-th pulse in the histogram is given by

$$k_{\mathrm{SN},s} = \frac{n_{\mathrm{L},s}}{\sqrt{\sigma_{\mathrm{B},s}^2 + \sigma_{\mathrm{L},s}^2}} = \frac{n_{\mathrm{L},s}}{\sqrt{n_{\mathrm{B},s} + n_{\mathrm{L},s}}}, \tag{5.11}$$

where the uncertainties of the laser and background signal $\sigma_{\mathrm{L},s}$ and $\sigma_{\mathrm{B},s}$ at the s-th pulse are given by the square roots of the number of laser and background photons $n_{\mathrm{L},s}$ and $n_{\mathrm{B},s}$ during the pulse width after the s-th TOF $t_{\mathrm{TOF},s}$. Again, the number of background photons $n_{\mathrm{B},s}$ affecting the s-th pulse is determined by the integral over the pulse width t_{p} but with the PDF $P(t|n_{\mathrm{s}})$ for multiple instead of single pulses and only the laser-generated event rate corresponding to the investigated s-th pulse is set to zero, which is explicitly given as $r_{\mathrm{L},s}$ in the more complex form in (5.4). In contrast to the SNR determination of a single pulse, the calculated number of background photons $n_{\mathrm{B},s}$ depends here not only on the background-generated event rate r_{B} but also on the laser-generated event rates $r_{\mathrm{L},i},\ i = 1, \ldots, s-1$ from the previous pulses resulting in

$$\begin{aligned} n_{\mathrm{B},s} &= n_{\mathrm{meas}} \int_{t_{\mathrm{TOF},s}}^{t_{\mathrm{TOF},s}+t_{\mathrm{p}}} P(t|n_{\mathrm{s}})|_{r_{\mathrm{L},s}=0}\,\mathrm{d}t \\ &= n_{\mathrm{meas}} \mathrm{e}^{-(s-1)r_{\mathrm{L}}t_{\mathrm{p}}} \left(1 - \mathrm{e}^{-r_{\mathrm{B}}t_{\mathrm{p}}}\right) \mathrm{e}^{-r_{\mathrm{B}}t_{\mathrm{TOF},s}}. \end{aligned} \tag{5.12}$$

where n_{meas} is the number of measurements per histogram, s is the number of the investigated pulse position and $t_{\mathrm{TOF},s}$ the corresponding TOF. The number of laser photons $n_{\mathrm{L},s}$ is determined by

$$\begin{aligned} n_{\mathrm{L},s} &= n_{\mathrm{meas}} \int_{t_{\mathrm{TOF},s}}^{t_{\mathrm{TOF},s}+t_{\mathrm{p}}} P(t|n_{\mathrm{s}})\mathrm{d}t - n_{\mathrm{B}} \\ &= n_{\mathrm{meas}} \mathrm{e}^{-(s-1)r_{\mathrm{L}}t_{\mathrm{p}}} \mathrm{e}^{-r_{\mathrm{B}}t_{\mathrm{TOF},s}} \left(\mathrm{e}^{-r_{\mathrm{B}}t_{\mathrm{p}}} - \mathrm{e}^{-(r_{\mathrm{B}}+r_{\mathrm{L},s})t_{\mathrm{p}}}\right). \end{aligned} \tag{5.13}$$

Inserting the derived number of laser and background photons in the SNR equation (5.11), the SNR for the s-th pulse of a histogram containing multiple pulses is given by

$$\begin{aligned} k_{\mathrm{SN},s} &= \sqrt{n_{\mathrm{meas}} \mathrm{e}^{-(s-1)r_{\mathrm{L}}t_{\mathrm{p}}} \mathrm{e}^{-r_{\mathrm{B}}t_{\mathrm{TOF},s}}} \cdot \frac{\mathrm{e}^{-r_{\mathrm{B}}t_{\mathrm{p}}} - \mathrm{e}^{-(r_{\mathrm{B}}+r_{\mathrm{L}})t_{\mathrm{p}}}}{\sqrt{1 - \mathrm{e}^{-(r_{\mathrm{B}}+r_{\mathrm{L}})t_{\mathrm{p}}}}} \\ &\approx \sqrt{n_{\mathrm{meas}} t_{\mathrm{p}} \mathrm{e}^{-(s-1)r_{\mathrm{L}}t_{\mathrm{p}}} \mathrm{e}^{-r_{\mathrm{B}}t_{\mathrm{TOF},s}}} \frac{r_{\mathrm{L}}}{\sqrt{r_{\mathrm{B}} + r_{\mathrm{L}}}}, \end{aligned} \tag{5.14}$$

where low background event rates as well as low laser event rates allow for the approximations $r_{\mathrm{B}} \ll {}^{1}\!/_{t_{\mathrm{p}}}$ and $(r_{\mathrm{B}} + r_{\mathrm{L}}) \ll {}^{1}\!/_{t_{\mathrm{p}}}$ to achieve the simpler approximated form of the SNR equation[1]. The approximated SNR equation allows for a faster calculation but for more exact results, the exact form without approximation is used in the following. With the derived SNR equation, the potential for the pulse detection of each laser pulse in the histogram can be estimated.

Each pulse influences the detection probability of the following pulses. To make the dependencies between all pulses and the background light more visible, it is useful to determine the probability of an arriving photon to be during the pulse width of a specific pulse or anywhere between the pulses. This probability with respect to the s-th pulse is given by the ratio of all photons within this pulse $n_{\mathrm{signal},s}$ and the total number of photons in the histogram n_{hist}. For comparison between the pulses, it is not distinguished if the photons at a pulse are generated by the laser pulse itself of by the background because the different background levels at the pulses increase their maximum heights as well. Thus, the probability of a photon p_{s}

[1] For a pulse width of $t_{\mathrm{p}} = 8\,\mathrm{ns}$, the approximated SNR equation can be applied for event rates up to $r_{\mathrm{L},1} = r_{\mathrm{L},2} = r_{\mathrm{B}} = 5\,\mathrm{MHz}$, where the resulting SNR deviates by 8 % from the SNR of the unapproximated equation.

to be detected during the s-th pulse is given by

$$p_\mathrm{s} = \frac{n_{\mathrm{signal},s}}{n_\mathrm{hist}} = \frac{n_\mathrm{meas} \int\limits_{t_{\mathrm{TOF},s}}^{t_{\mathrm{TOF},s}+t_\mathrm{p}} P(t|n_\mathrm{s})\,\mathrm{d}t}{n_\mathrm{meas} \int\limits_{0}^{t_\mathrm{hist}} P(t|n_\mathrm{s})\,\mathrm{d}t} = \frac{\mathrm{e}^{-(s-1)r_\mathrm{L}t_\mathrm{p}}\left(1-\mathrm{e}^{-(r_\mathrm{B}+r_\mathrm{L})t_\mathrm{p}}\right)\mathrm{e}^{-r_\mathrm{B}t_\mathrm{TOF}}}{1-\mathrm{e}^{-n_\mathrm{s}r_\mathrm{L}t_\mathrm{p}}\mathrm{e}^{-r_\mathrm{B}t_\mathrm{hist}}}, \tag{5.15}$$

where the number of photons in the histogram is not equal to the number of measurements per histogram n_meas due to measurements, in which no photon have been detected, so that its expectation value must also be calculated by the integration over the total histogram length t_hist. In Figure 5.6, the first pulse of the orange histogram shows a probability of 33 %, whereas the second pulse has only a probability of 2 % for a photon to lie within. For the blue histogram, the probabilities of first and second pulse are 15 % and also 2 %. For both example histograms, the rest of the histogram apart from the pulses represents the largest percentage of arriving photons. The other parts of this Figure are explained in the next section.

5.3 Unrecognizable LiDAR Interference

From the PDF in (5.4), it is seen that each pulse height is reduced by the previous background and previous pulses arriving at the LiDAR system. Assuming two pulses, the SNR of the second pulse can be so low that it is hardly detectable anymore, which is shown in Figure 5.6. The later the second pulse arrives, the smaller becomes its SNR. The TOF of the second pulse might result in an SNR too low for detection. The corresponding minimum TOF will be denoted as extinction TOF t_ext or with regards to the real target as extinction distance d_ext. As worst case, it is assumed that the first pulse is from the aggressor system, whereas the second pulse belongs to the ego system and thus represents a real target distance. Although the aggressor pulse can also be reflected by a real target, the aggressor pulse arrives at an arbitrary time at the ego system due to time differences between both systems. In the following, the conditions for an unrecognizable ego pulse are discussed.

The required minimum SNR value for the detection of the ego pulse depends on the data processing algorithm. As discussed in section 5.2.1, the ego pulse at the second position might only be slightly lower than the aggressor pulse, but the data

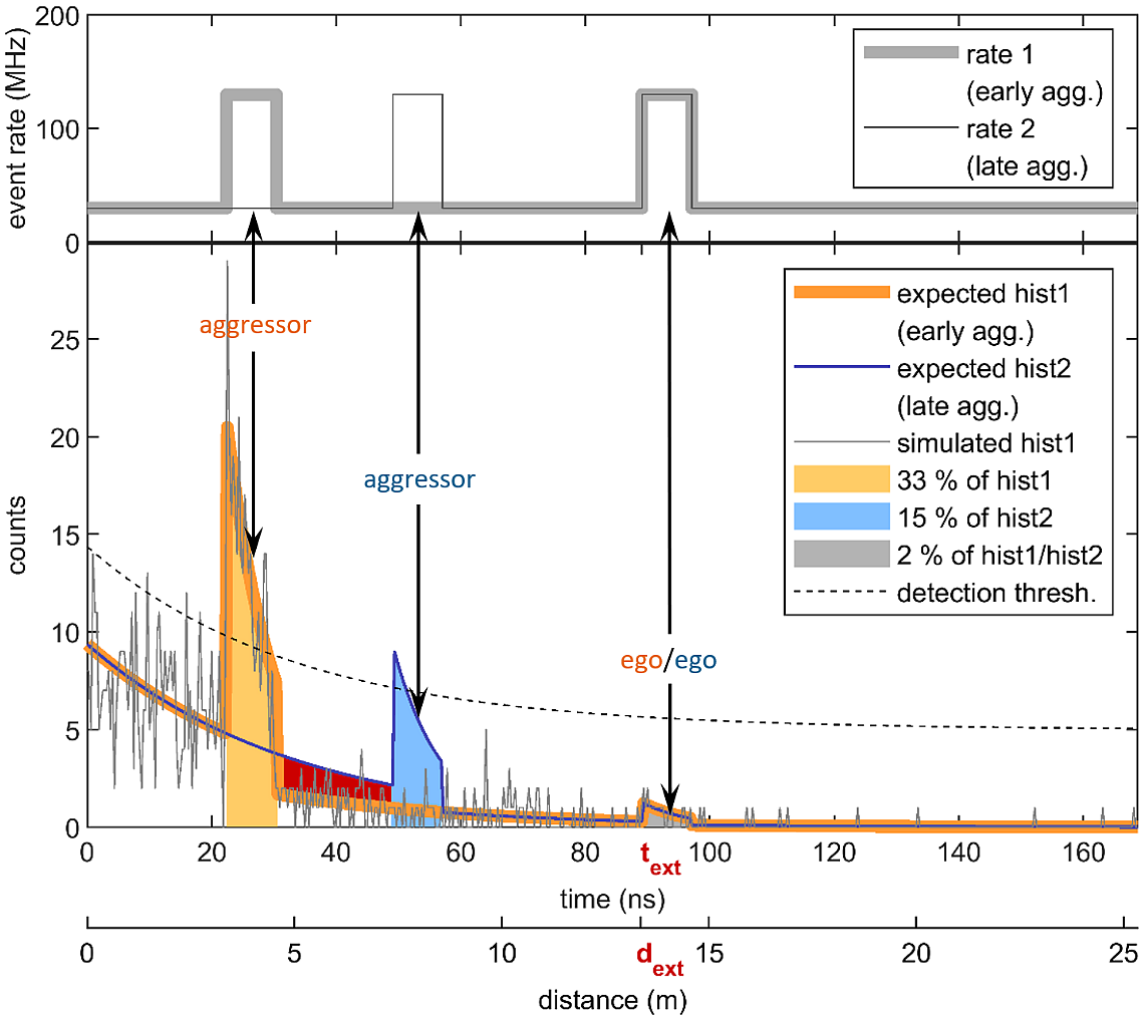

Figure 5.6: Two example histograms with different TOFs of their first laser signals resulting in the same extinction distance of the second laser signal but temporarily differing at the background level, which is marked as red area [118]

processing algorithm might still only choose the highest pulse and ignore all other pulses in the histogram. Instead of the maximum value detection, other data processing algorithms define a threshold, where every signal above the threshold counts as signal [119]. Such a threshold can be applied after the described exponential background subtraction and mean filter in section 5.2.1. This constant threshold as final algorithm step corresponds to an exponential threshold as drawn in Figure 5.6. The ego pulse in the Figure is so low that it is not detected anymore by this algorithm. It is also seen that the threshold might not be optimal for the detection of multiple pulses because the background fluctuations decrease with the lower number

of counts in the later histogram and after each pulse, the exponential background curve is reduced. As a result, the threshold becomes unnecessarily high at the end of the histogram so that less pulses might be detected there although the SNR might be generally sufficient for a pulse detection. However, each data processing algorithm requires a minimum SNR of a laser pulse to be able to detect this pulse in the histogram. Assuming an algorithm that requires a minimum of SNR $k_{\mathrm{SN,min}}$ for a successful target distance determination, the extinction TOF t_{ext} can be calculated from the SNR equation (5.14) by

$$t_{\mathrm{ext}} = \frac{1}{r_{\mathrm{B}}} \cdot \ln\left(\frac{n_{\mathrm{meas}}}{k_{\mathrm{SN,min}}^2} \mathrm{e}^{-r_{\mathrm{L}} t_{\mathrm{p}}} \frac{\left(\mathrm{e}^{-r_{\mathrm{B}} t_{\mathrm{p}}} - \mathrm{e}^{-(r_{\mathrm{B}}+r_{\mathrm{L}}) t_{\mathrm{p}}}\right)^2}{1 - \mathrm{e}^{-(r_{\mathrm{B}}+r_{\mathrm{L}}) t_{\mathrm{p}}}} \right), \tag{5.16}$$

which corresponds to the extinction distance d_{ext} via (2.1). The extinction distance indicates the distance, from which the ego pulse might become invisible in the histogram and only the aggressor pulse is seen. Therefore, a LiDAR is designed best if the extinction distance is high enough so that the interference can be always recognized because both the aggressor and ego pulse are seen for a real target distance below the extinction distance. Typical values of the extinction distance will be discussed in the next sections.

It is remarkable that the extinction distance does not depend on the TOF of the aggressor pulse but only on the laser-generated event rate r_{L} of this pulse, which is given as factor $\mathrm{e}^{-r_{\mathrm{L}} t_{\mathrm{p}}}$ in the equation above. In Figure 5.6, two different histograms are shown. The orange histogram has an aggressor signal with early TOF, whereas the blue histogram has a late aggressor TOF. The corresponding incident generating event rates are the same for both aggressor pulses as shown in the upper half of the Figure. Independent of the aggressor TOF, the ego pulse of both histograms appears at the same extinction distance in the histogram with the same pulse shape. The orange histogram has a higher aggressor pulse than the blue one but a temporarily lower background level after the orange pulse, which is marked as red area. This early aggressor pulse strongly reduces the background afterwards. The blue aggressor pulse appears later and lower in the histogram. It reduces the background level moderately as well so that it decreases exactly on the height of the orange background level at the same position in the histogram. Although the intensities of aggressor pulse and background level are different, the total integral of the PDF has the same value for both histograms. This is also seen at the generating event rates arriving before the ego pulse, which are the same value integrated and

hence reduce the ego pulse in the same way. The histograms in Figure 5.6 finally confirm that the extinction distance is independent of the aggressor TOF, assuming that the aggressor pulse arrives at any time before the ego pulse. The minimum value that can be obtained for the extinction TOF is the aggressor pulse width because both pulses are assumed to be non-overlapping so that the ego pulse is arriving the earliest, assumed to occur directly after the aggressor pulse with pulse width t_p. The pulse width of LiDAR system *Owl* is equivalent to 1.2 m according to (2.1).

To evaluate the extinction distance, the parameters of LiDAR system *Owl* are used. Assuming a target at a distance of 10 m with the highest possible reflectance of 100 %, the laser-generated event rate can be calculated as described in section 2.2 to $r_\mathrm{L} = 100\,\mathrm{MHz}$. Furthermore, a moderate background-generated event rate of $r_\mathrm{B} = 30\,\mathrm{MHz}$ is chosen [120]. For each histogram, $n_\mathrm{meas} = 1000$ measurement are performed and an algorithm requiring a minimum SNR $k_\mathrm{SN,min} = 3$ is assumed [121]. These standard parameters are used in the following considerations if not declared otherwise. In the following, the properties of the extinction distance indicating an unrecognizable ego pulse are analyzed. Optimal conditions are identified to avoid unrecognizable interference.

5.3.1 Number of Measurements

The pulse heights in the histogram not only depend on the PDF in (5.4) but also on the number of measurements in a histogram, which is shown in Figure 5.7. For $k_\mathrm{SN,min} = 3$, the extinction distances begin at about 0 m for approximately 100 measurement per histogram up to almost 70 m for 10000 measurements. To be more precise, the minimum extinction distance is 1.2 m due to the aggressor pulse width as described above. The number of measurements $n_\mathrm{meas,min}$ for this minimum extinction distance can be calculated from (5.16) as

$$n_\mathrm{meas,min} = k_\mathrm{SN,min}^2 \frac{\mathrm{e}^{(r_\mathrm{B}+r_\mathrm{L})t_\mathrm{p}} - 1}{\left(\mathrm{e}^{-r_\mathrm{B}r_\mathrm{p}} - \mathrm{e}^{-(r_\mathrm{B}+r_\mathrm{L})t_\mathrm{p}}\right)^2}. \tag{5.17}$$

The resulting values are illustrated as filled circles in Figure 5.7. For an even lower number of measurements, the extinction distance would mathematically become negative. In this parameter range, the aggressor pulse also becomes unrecognizable in the histogram so that no pulse can be detected at all. Besides the number of

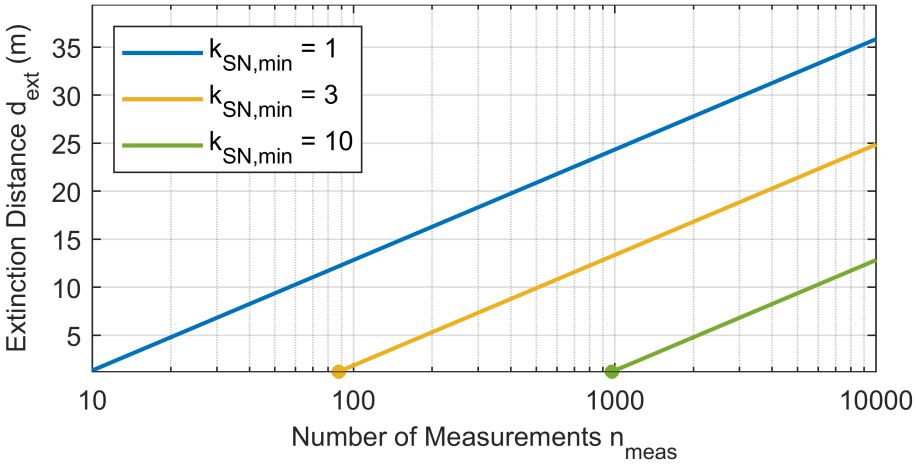

Figure 5.7: Extinction distance d_{ext} depending of the number of measurements per histogram n_{meas} for different SNRs. The minimum number of measurements $n_{\text{meas,min}}$ for a just detectable ego signal behind the aggressor signal is marked as filled circle each [118]

measurements, the extinction distance depends on the data processing algorithm and its required minimum SNR. From theory, the SNR must be $k_{\text{SN}} \geqslant 1$. As examples, minimum SNR values of 1, 3 and 10 are chosen, which are illustrated in Figure 5.7. As the extinction equation (5.16) provides a square-dependency on the SNR, the three approximately logarithmically chosen SNR values each result in an extinction distance increase of about 13 m. The highest extinction distance and hence best interference recognition is achieved for the lowest minimum SNR and the highest number of measurements in a histogram.

5.3.2 Background- and Laser-Generated Event Rate

As mentioned before, the reduction of the ego pulse depends on the background- and laser-generated event rate due to the first-photon measurement principle. The laser-generated event rate contributes to the aggressor pulse reducing the ego pulse but also influences the ego pulse increasing the pulse height. In Figure 5.8, the resulting extinction distances are shown. There is a maximum extinction distance, which balances the heights of aggressor and ego pulse by the laser-generated event rate, which can only numerically determined by solving

$$2\mathrm{e}^{-(2r_{\text{B}}+r_{\text{L,ideal}})t_{\text{p}}} + \mathrm{e}^{(r_{\text{L,ideal}}-r_{\text{B}})t_{\text{p}}} = 3\mathrm{e}^{-r_{\text{B}}t_{\text{p}}}. \tag{5.18}$$

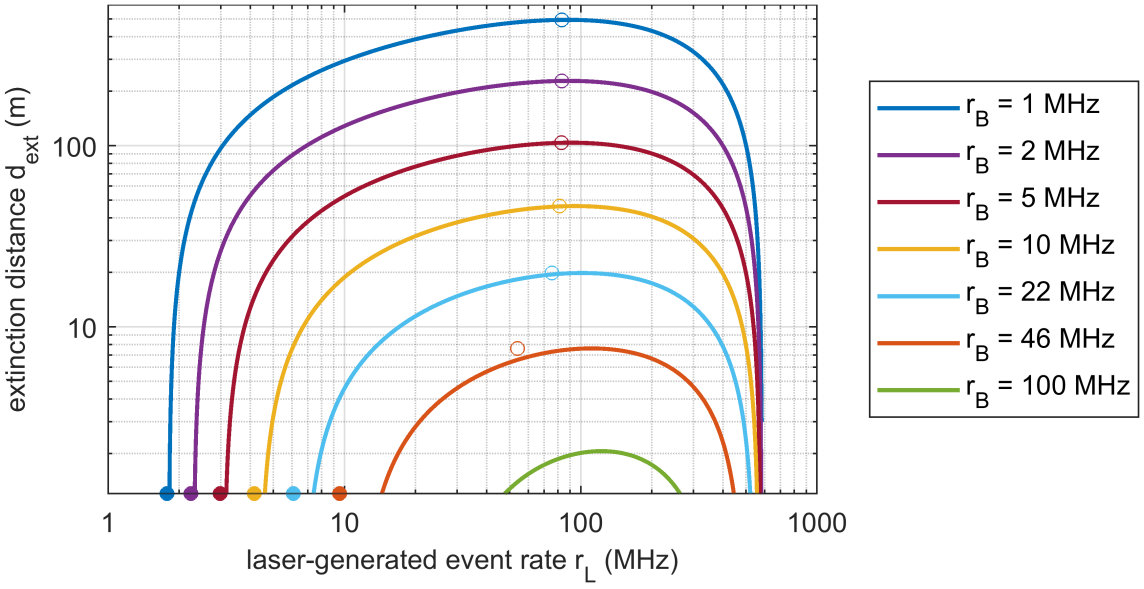

Figure 5.8: Extinction distance d_{ext} depending on the laser-generated event rate r_{L} and background-generated event rate r_{B}. The minimum laser-generated event rates are marked with filled circles and the ideal laser-generated event rates are marked as empty circles. [118]

Using the approximations $r_{\text{B}} \ll 1/t_{\text{p}}$ and $(r_{\text{B}} + r_{\text{L}}) \ll 1/t_{\text{p}}$ in the SNR equation (5.14), this ideal laser-generated event rate $r_{\text{L,ideal}}$ can be approximated by an analytical expression given by

$$r_{\text{L,ideal}} \approx \frac{1}{3t_{\text{p}}} - r_{\text{B}} + \sqrt{\left(\frac{1}{3t_{\text{p}}} - r_{\text{B}}\right)^2 - 2r_{\text{B}}^2} \approx \frac{2}{3t_{\text{p}}} = 83\,\text{MHz}, \tag{5.19}$$

where an additional stronger approximation $r_{\text{B}} \ll 1/3t_{\text{p}}$ can be applied to achieve the simple second expression resulting in $r_{\text{L,ideal}} = 83\,\text{MHz}$ for a pulse width of $t_{\text{p}} = 8\,\text{ns}$. In Figure 5.8, the maximum position calculated by the first term is marked with empty circles and all circles are almost at the same position of 83 MHz independent of the background level as predicted by the second term. This strongly approximated term does not depend on the background-generated event rate r_{B} anymore but only on the laser pulse width t_{p}, which means that the influence of the background is negligible compared to the effects between aggressor and ego pulse. For the second highest background-generated event rate of 46 MHz, the ideal laser-generated event rate differs from the others and for the highest background level, this approximated maximum position is not valid anymore and hence not drawn in the Figure. However, for a moderate background-generated event rate of $r_{\text{B}} = 10\,\text{MHz}$,

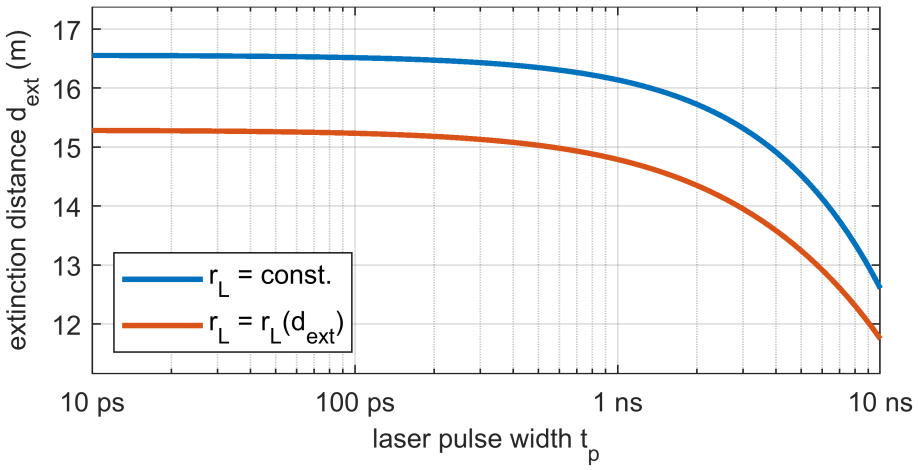

Figure 5.9: Extinction distance d_{ext} depending on the laser pulse width t_{p} for a constant laser-generated event rate $r_{\mathrm{L}} = \text{const.}$ or for a specific LiDAR system, e.g. considering eye safety by $r_{\mathrm{L}} t_{\mathrm{p}} = \text{const.}$ [118]

the maximum extinction distance is 46 m, which might be lower than real target distances. Besides the ideal laser-generated event rates, the minimum values $r_{\mathrm{L,min}}$ are drawn as filled circles given by

$$r_{\mathrm{L,min}} \approx \frac{k_{\mathrm{SN,min}}^2}{2 n_{\mathrm{meas}} t_{\mathrm{p}}} \mathrm{e}^{r_{\mathrm{B}} t_{\mathrm{ext}}} + \frac{1}{t_{\mathrm{p}}} \sqrt{\left(r_{\mathrm{B}} t_{\mathrm{p}} + \frac{k_{\mathrm{SN,min}}^2}{2 n_{\mathrm{meas}}} \mathrm{e}^{r_{\mathrm{B}} t_{\mathrm{ext}}} \right)^2 - r_{\mathrm{B}}^2 t_{\mathrm{p}}^2}, \tag{5.20}$$

where the approximations $r_{\mathrm{B}} \ll 1/t_{\mathrm{p}}$ and $(r_{\mathrm{B}} + r_{\mathrm{L}}) \ll 1/t_{\mathrm{p}}$ are applied again but already differs from the actual minimum values starting from a background-generated event rate of 10 MHz. Besides the laser intensities, the background affects the extinction distance. As seen in the Figure, there is a maximum background level of 100 MHz drawn because 1 GHz already produces unrecognizable interference for all possible laser-generated event rates. With the laser- and background-generated event rate, the potential of unrecognizable LiDAR interference in a specific environment can be estimated. The best environment conditions to avoid unrecognizable interference are given for the derived ideal laser-generated event rate, which can be achieved by an optimal LiDAR system parameter choice.

5.3.3 LiDAR Interference for a Specific LiDAR System

In the previous investigations, abstract laser-generated event rates have been used. For a specific LiDAR design, the laser-generated event rate is defined by the chosen

LiDAR parameters like optical laser power. Because of the eye safety limit discussed in section 2.1.3, the product of optical power and the laser pulse width must be constant with $r_\mathrm{L} t_\mathrm{p} = \text{const}$. Without the eye safety limit, a constant laser-generated event rate $r_\mathrm{L} = \text{const.}$ can be assumed and the dependency of the extinction distance on the pulse width can numerically be determined by

$$\frac{2r_\mathrm{L}}{\mathrm{e}^{r_\mathrm{L} t_\mathrm{p}} - 1} + \frac{r_\mathrm{B} + r_\mathrm{L}}{1 - \mathrm{e}^{(r_\mathrm{B}+r_\mathrm{L})t_\mathrm{p}}} = 2 \cdot r_\mathrm{B} + n_\mathrm{s} r_\mathrm{L}, \tag{5.21}$$

which is shown in Figure 5.9. Considering eye safety, the laser-generated event rate depends on the respective target distance because all other parameters of the LiDAR system are fixed. If the extinction distance is calculated for a specific LiDAR system, this proportion of the extinction distance as maximum recognizable target distance to the laser-generated event rate must be included. The dependency of the laser-generated event rate r_L on the extinction distance d_ext is expressed in the optical power equation (2.17) by

$$r_\mathrm{L}(d_\mathrm{ext}) = \frac{x_d}{d_\mathrm{ext}^2} = \frac{x_t}{t_\mathrm{ext}^2}, \tag{5.22}$$

where x_t is given by

$$x_t = \frac{4x_d}{c^2} = \Phi_\mathrm{L} \cdot \eta_\mathrm{illum} \cdot \rho \left(\frac{D}{2}\right)^2 \cdot T \cdot \eta_\mathrm{PDE} \cdot \frac{1}{E_\mathrm{ph}}. \tag{5.23}$$

This laser-generated event rate with dependency on the specific LiDAR parameters and variable target distance can be inserted in the SNR equation (5.14) to determine the extinction distance again. Due to the exponential functions, the SNR equation can only numerically be solved for the extinction distance or rather extinction TOF t_ext by

$$\frac{n_\mathrm{meas}}{k_\mathrm{SN,min}^2} = \mathrm{e}^{\frac{x_t}{t_\mathrm{ext}^2} t_\mathrm{p}} \mathrm{e}^{r_\mathrm{B} t_\mathrm{ext}^2} \frac{1 - \mathrm{e}^{-(r_\mathrm{B} + \frac{x_t}{t_\mathrm{ext}^2})t_\mathrm{p}}}{\left(\mathrm{e}^{-r_\mathrm{B} t_\mathrm{p}} - \mathrm{e}^{-(r_\mathrm{B} + \frac{x_t}{t_\mathrm{ext}^2})t_\mathrm{p}}\right)^2}. \tag{5.24}$$

As a result, the extinction distance is reduced because the attenuation of the laser-generated event rate by the target distance is considered here. In Figure 5.9, the extinction distances of a constant laser-generated event rate and of a specific LiDAR system differ by about 1 m because the underlying laser-generated event rates seems to be in the same order. However, for a specific LiDAR system, the corresponding laser-generated event rates considering the eye safety are more precise. Shorter

pulse widths lead to higher extinction distances but the effect becomes small for pulse widths lower than 1 ns.

The previous results show that unrecognized interference might occur often. Target distances of about 15 m can already lead to an unrecognized ego pulse in the histogram. The probability for unrecognizable interference can be reduced by an optimal choice of the LiDAR system parameters. However, if interference is recognized, the question remains which pulse in the histogram is the ego pulse, which is investigated in the next chapter.

Chapter 6

Interference Suppression

There are different possibilities to solve LiDAR interference problems. To avoid the spatial or temporal condition of interference as described in chapter 3, uncontrolled environments can be brought under control by additional communication systems. For example, autonomous driving can be made controllable by a vehicle-to-x communication. The communication partner x can be a satellite, traffic light, another independent global system or even another vehicle itself. If multiple vehicles communicate with each other, they can coordinate which LiDAR system will measure next. In this case, all LiDAR systems can measure alternately at different times without disturbing each other. Today, these communication systems are not yet widely applied so that autonomous driving still represents an application with uncontrolled environment. Therefore, an interference suppression method suitable for LiDAR applications with uncontrolled environments is presented in this chapter.

In a LiDAR histogram affected by interference, multiple pulses might be obtained as shown in the previous chapter. To identify the ego pulse in the histogram, the aggressor signals can be suppressed during the histogram acquisition. For the suppression of interference between LiDAR systems, there are some suppression methods for various LiDAR methods in the literature, which are evaluated with regards to dTOF LiDAR using SPADs for the acquisition of TCSPC histograms. From that, an interference suppression method is developed, which is based on the recognition of all pulses in a histogram and randomly modulates the pulse emission times of the next LiDAR measurement.

6.1 Related Work for Different LiDAR Methods

Interference suppression algorithms have been discussed for different LiDAR methods like dTOF, iTOF and FMCW, which have been explained in section 2.1.1. For each method, different photodetectors can be used as presented in section 2.1.2. For example, analogue detectors like APDs can be used, which are able to measure the temporal intensity profiles of the pulses, or digital detectors like SPADs, which can hardly measure pulse forms due to the pile-up effect but are more sensitive. Besides the LiDAR systems itself, the controllability of the environment is crucial for the choice of a suitable method. Controlled environments are often given for industrial applications, where positions and forms of surrounding objects can be known or a communication system between the LiDAR system exists, whereas uncontrolled environments like traffic in autonomous driving include many moving objects with unknown position or future behavior. The field of communication provides different solutions for interference suppression, which might be transferred to LiDAR [68].

According to the LiDAR interference conditions in section 3.1.2, the spectral overlap of LiDAR systems can be avoided if they use different laser wavelengths, which is called wavelength-division multiple access (WDMA) in the field of communication. LiDAR systems with silicon detectors often operate in the near-infrared range from 700 nm to 1000 nm [28], whereas 1550 nm is a common wavelength for InGaAs detectors, which are sensitive for these longer wavelengths as well [22, 29]. Besides the potential laser sources, the detector sensitivity varies with the detected wavelengths. Therefore, WDMA is rather useful for controlled environments with only a few systems but not for uncontrolled environments, where the laser wavelengths of the other LiDAR systems are not known. Similar to the wavelength, LiDAR methods like iTOF or FMCW can be separated by their frequencies, which is called frequency-division multiple access (FDMA). For iTOF LiDAR, different modulation frequencies can be applied, and for FMCW LiDAR, the frequency range can be chosen to be non-overlapping. Again, the number of different frequencies for all involved LiDAR systems is limited so that FMCW is also rather suitable for a few controlled systems. Especially for controlled environments, the LiDAR systems can also be separated spatially, which is the second interference condition in section 3.1.2. This so-called space-division multiple access (SDMA) can be achieved by separated FOVs of the systems as discussed in section 3.2. The third interference

condition is temporal overlap, which is also the last further possibility to completely avoid LiDAR interference. This is called time-division multiple access (TDMA) in the field of communication. For a controlled environment, the measurement times of the different systems can be performed alternating so that only one LiDAR system measures at once. The maximum number of alternating LiDAR system depends on the laser PRF and the measurement time corresponding to the maximum target distance as derived in section 3.3. For uncontrolled environments, the field of communication provides only code-division multiple access (CDMA), which concerns the emitted laser light. Considering the laser pulses of dTOF LiDAR, the pulse form can be modulated [122]. Alternatively, quasi-continuous pulse patterns can be used, which means coded pulse trains [123, 124]. The pulse forms can be detected by analogue photodetectors, but LiDAR systems with SPADs are not well suited because the first-photon measurement principle causes the pile-effect in the measured histogram so that the laser pulse shapes are distorted in the histogram. For SPADs with multi-event detection, CDMA can be used with dual-pulse emission considering the dead time [9]. The investigated LiDAR interference in this work particularly focuses on dTOF LiDAR systems in an uncontrolled environment using SPADs, where first-photon detections are accumulated in a histogram. For this case, only pulse-position modulation (PPM) or similar methods are applicable, where the laser pulse emission times are encoded [125–131]. [2, 68]

6.2 Multi-Pulse Recognition Algorithm

Before the suppression method proposed in this work, the number of pulses in the histogram and their positions must be determined. There are many LiDAR algorithms, which might only be suitable for a single pulse as discussed in section 5.2.1. A histogram with multiple pulses shows a complex count distribution, where the pulses and the background level at different positions in the histogram can have different heights due to the pile-up effect although the corresponding rates have originally been equal. To the best of my knowledge, no suitable algorithm for the recognition of multiple pulses in a histogram suffering from pile-up effects exists in the literature so that a multi-pulse recognition method is developed in the following. The working principle is presented by the example of a simulated histogram in Figure 6.1. The incident event rate consisting of the background-generated event

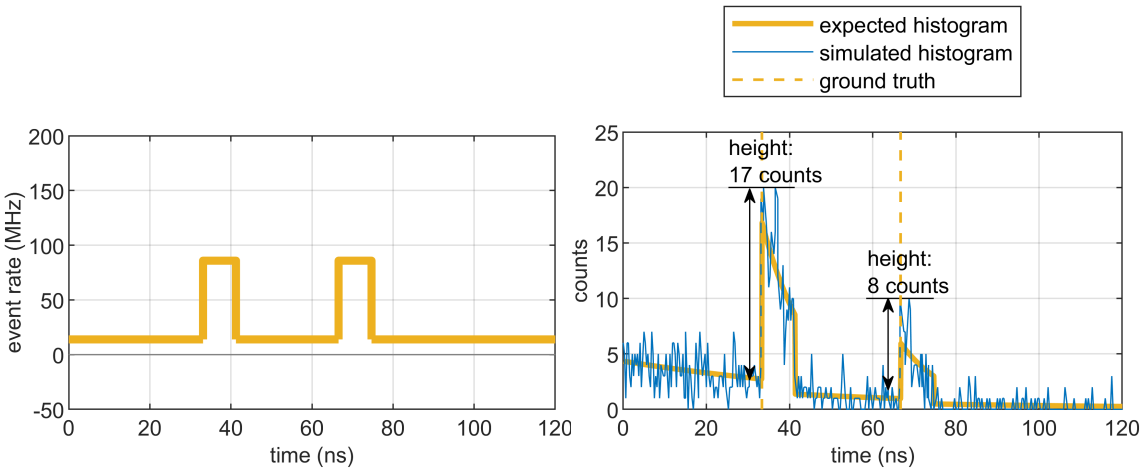

(a) Generating event rate

(b) Original histogram

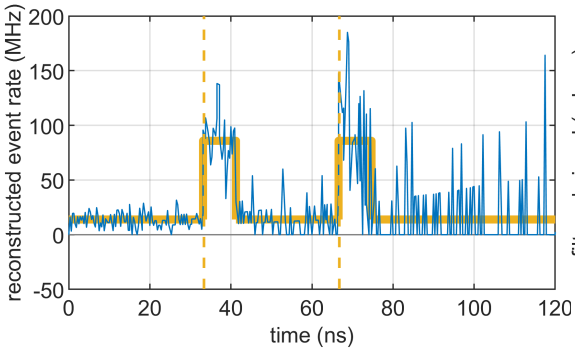

(c) Pile-up correction

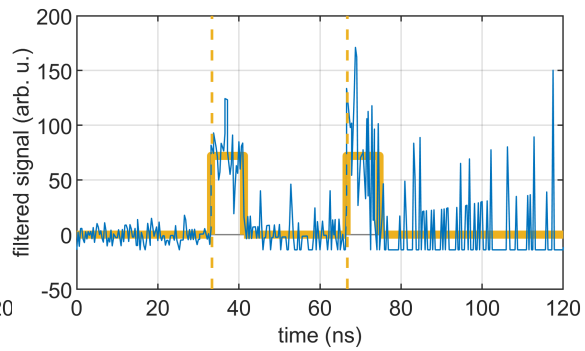

(d) Background subtraction

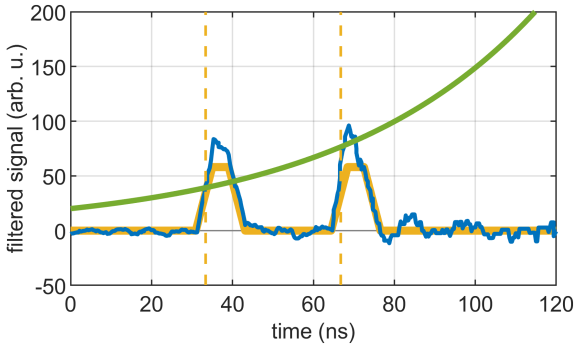

(e) Mean filter and exp. threshold

Figure 6.1: Multi-pulse recognition method applied on a simulation with two pulses, where a pulse is identified for a minimum of 3 connected bins above the threshold if no other pulse has been identified before within one pulse width at this histogram position

rate of about 10 MHz and laser-generated event rate of about 70 MHz is shown in Figure 6.1a, which results in the histogram with two pulses in Figure 6.1b. The proposed algorithm consists of the following steps:

1. pile-up correction
2. background subtraction
3. smoothing by moving average filter
4. threshold to cut off fluctuations
5. condition for pulse identification: pulse width $\geqslant 3$ bins

The **first step** of the algorithm is a pile-up correction, which is performed to recover the incident event rates at the LiDAR detector so that the pulse heights become again in right proportion to each other and the constant background level can be seen [5]. For the i-th bin containing n_i counts, the belonging event rate is calculated by

$$r_i = \frac{1}{t_{\mathrm{bin}}} \cdot \ln\left(\frac{n_{\mathrm{meas}} - \sum_{k=1}^{i-1} n_k}{n_{\mathrm{meas}} - n_i - \sum_{k=1}^{i-1} n_k}\right), \tag{6.1}$$

where n_{meas} is the number of performed measurements per histogram and the bin width t_{bin} normalizes the event rate on the unit s^{-1} [6]. It should be noticed that the total number of detected photons in the histogram can be lower than this number of performed measurements n_{meas} due to misdetections. In Figure 6.1c, the pile-up correction has been applied so that the event rates of Figure 6.1a are approximately reobtained, which were 80 MHz at the pulse heights, where the background- and laser-generated event rate are combined. Especially at the histogram beginning before the pulses, it is seen that the background is constant again.

The **second step** of the multi-pulse recognition algorithm is equivalent to the histogram data processing considering a single pulse as introduced in section 2.3.3. As explained in this section, the background-generated event rate r_{B} must be determined before the histogram measurement, e.g. by the described counting mode. Equivalent to the exponential background subtraction there, the multi-pulse recognition algorithm subtracts the constant background-generated event rate $r_{\mathrm{B}} = 10\,\mathrm{MHz}$. The resulting histogram is illustrated in Figure 6.1d. Due to background fluctua-

tions, the filtered histogram entries can become negative after this algorithm step.

As the **third step**, the same forward-looking mean filter from section 2.3.3 is applied to smooth the fluctuations especially behind the pulses, where the pile-up effect emphasizes these large fluctuations. As late single background photons might represent strongly suppressed pulses, the pile-up correction overemphasizes them to regain the original event rate. If these single counts are not produced by a strongly suppressed pulse but caused by fluctuations, they often have empty neighboring bins. Therefore, the applied mean filter especially smoothes the fluctuations at the end of the histogram, which is demonstrated in Figure 6.1e. The pulses in the filtered histogram are well visible now.

In the **fourth step**, the remaining background fluctuations especially at the end of the histogram are excluded by a suitable threshold considering the expected background behavior. The threshold must be chosen high enough so that even for a histogram without any laser photons, no background fluctuations are falsely detected as a laser signal. According to the ISO standard *Road vehicles — Functional safety*, such a single-point fault must be avoided in $\geqslant 99\,\%$ of all cases [80]. Therefore, a 3σ level of the expected background uncertainty is chosen. The LiDAR detector observes the background uncertainty as fluctuations within each bin, which are given by the square root of the counts per bin due to the Poisson statistics [52]. The background-generated event rate r_B is obtained in the PDF in (5.5) for the time $t = 0$, which approximately corresponds to the count value in the first bin of the histogram resulting in an expected background uncertainty σ_{n_B} of

$$\sigma_{n_\mathrm{B}} = \sqrt{n_\mathrm{meas} \cdot t_\mathrm{bin} \cdot r_\mathrm{B}}, \tag{6.2}$$

where n_meas is the number of measurements per histogram and t_bin is the bin width. Transforming this uncertainty given in counts back to an event rate, the background uncertainty σ_{r_B} is determined by

$$\sigma_{r_\mathrm{B}} = \frac{\sigma_{n_\mathrm{B}}}{n_\mathrm{meas} \cdot t_\mathrm{bin}}. \tag{6.3}$$

The pile-up correction of the first algorithm step weighted the exponential background distribution approximately by its inverse, which recovered the constant background level but also influenced the background uncertainties in the same way as seen in Figure 6.1d. Using the expected inverse exponential background distribution of a histogram without laser from the PDF in (5.5), the 3σ level of the determined

background uncertainty σ_{r_B} can be inserted so that the exponential threshold $f(i)$ for the i-th bin results in

$$f(i) = 3\sigma_{r_\mathrm{B}} \cdot \exp\left(3\sigma_{r_\mathrm{B}} \cdot t_\mathrm{bin} \cdot i\right). \tag{6.4}$$

The threshold is drawn in Figure 6.1e, where it seems to be higher than necessary. However, the requirement of such a high threshold and its performance are discussed later in more detail.

As the last **fifth step**, the laser pulse beginnings are defined at a minimum of three connected bins above the threshold to prevent the detection of high background fluctuations in single bins as also shown later. To exclude possible fluctuations around the chosen threshold caused by a single pulse, not more than one pulse must be identified in the histogram within one pulse width of the originally emitted laser. The pulses are assumed not to overlap because it is difficult to distinguish a single pulse with fluctuating pulse form from two partially overlapping pulses. However, two overlapping pulses represent a similar target distance apart from an uncertainty maximally given by the pulse width in the worst case, which is 1.2 m for an emitted pulse with 8 ns according to (2.1).

After the detection of all pulses in the histogram, the pulse beginnings are determined. In the original histogram at these pulse positions, each pulse height can be estimated as maximum within one pulse width starting from the pulse beginning. For the simulated example histogram in Figure 6.1, the expected histogram distribution at the second pulse is below the threshold but including the fluctuations of the simulation, both pulses are successfully recognized. For the recognized pulses of this simulated histogram, the difference between the pulse heights without the background below these pulses is approximately a factor of 2.1 as drawn in Figure 6.1b.

The multi-pulse detection algorithm is tested for simulated histograms with two pulses at TOFs equivalent to 5 m and 10 m target distance, which are produced by all combinations of background- and laser-generated event rates each within 10^5 Hz and 10^{10} Hz. The resulting number of detected laser pulses in the histograms is averaged over ten simulations and shown in Figure 6.2. The dark blue color indicates scenarios, where no pulse has been observed at all, bright blue is equivalent to the detection of one pulse, the green color indicates histograms, where two pulses have been recognized correctly as they have been simulated, and yellow represents three

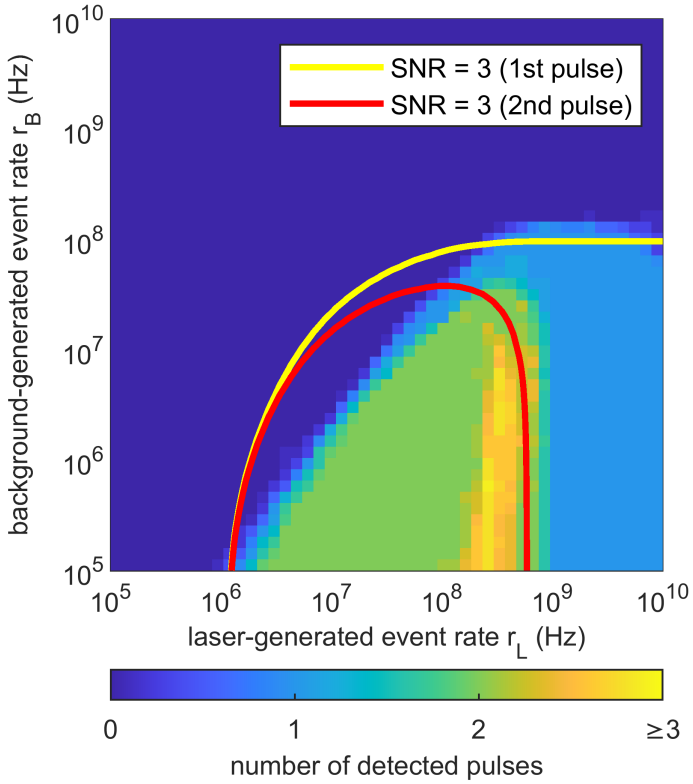

Figure 6.2: Average number of detected pulses for 10 simulations. The multi-pulse recognition algorithm can approximately be applied for SNR values of $k_{\mathrm{SN}} \geqslant 3$.

or more detected pulses. To evaluate the potential for each pulse recognition, the theoretical contour line of SNR = 3 according to (5.14) is drawn. The first pulse has an SNR increasing with the laser-generated event rate r_{L}, whereas the SNR of the second pulse drops again for very high laser-generated event rates r_{L} due to the reduction by the first pulse as explained in section 5.3.2. Below the contour lines, the SNR value becomes even larger. Outside of the contour lines, the SNR becomes very small so that a pulse detection can hardly be performed.

For most scenarios with these small SNR values, the multi-pulse detection algorithm recognizes no pulse. If no pulse is detected, the LiDAR system can indicate the failed detection by a warning or improve the next LiDAR measurement by coincidence detection or time gating as described in section 2.1.1. Much more dangerous would be an indication of one pulse although there is only background in the histogram because this pulse would be detected at an arbitrary position in the histogram resulting in an arbitrary target distance, which is probably wrong. For the proposed multi-pulse detection algorithm, this number of potentially dangerous

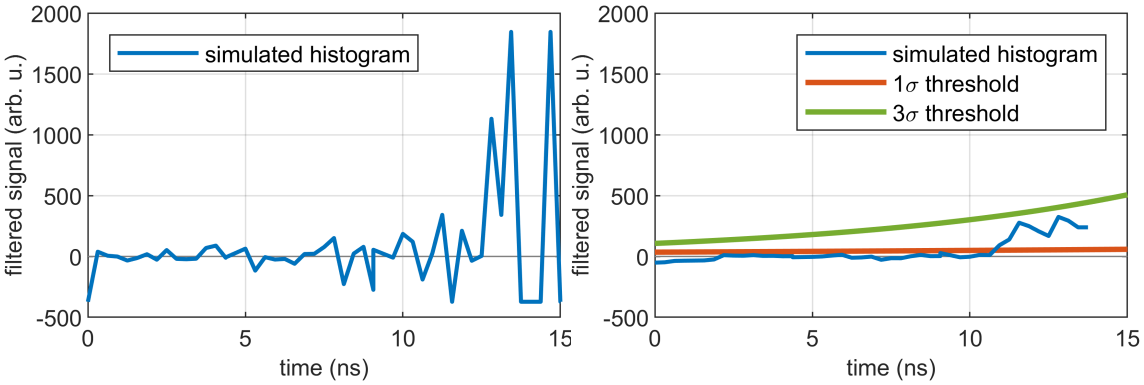

(a) Pure background histogram with pile-up correction and background subtraction

(b) Pure background histogram with mean filter and threshold of 1σ and 3σ

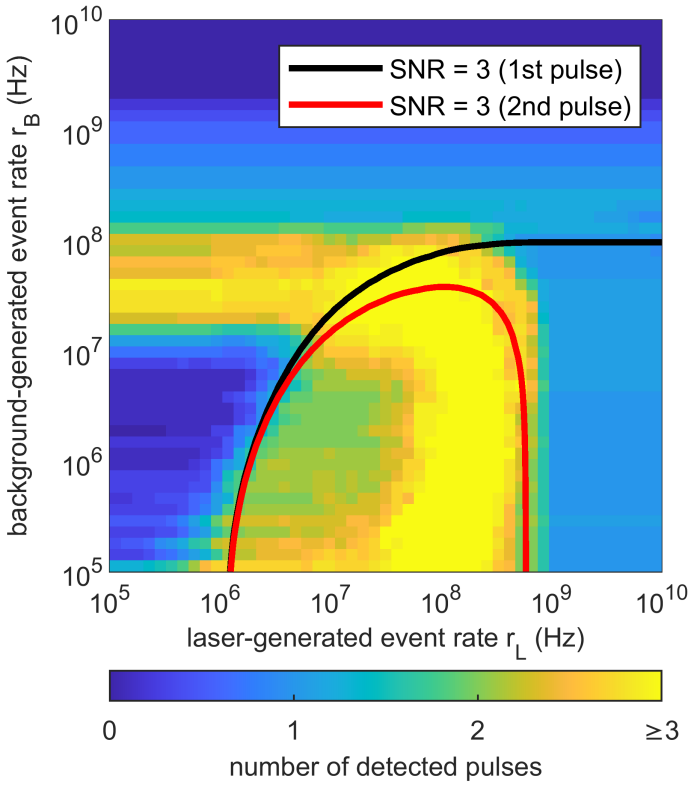

(c) Result for 1σ threshold

Figure 6.3: In contrast to the 3σ threshold used in Figure 6.2, the 1σ threshold produces many false detections especially for pure background histograms without any laser pulse, where background fluctuations are detected as laser signal.

false detections is very small because a threshold corresponding to a 3σ background uncertainty has been chosen. This large threshold also leads to histograms below the contour line of the second pulse, where no pulse has been detected although the SNR is comparatively high. Additionally, the threshold seems to be high compared to the background level in Figure 6.1, but in this particular histogram, the background is reduced due to the two pulses in the histogram. For a histogram with pure background light without any detected laser photon, the threshold must hold as well. The background in histograms without any laser photons increases exponentially after the first two filter steps of applied pile-up correction and background subtraction as seen in Figure 6.3a. After the third algorithm step of smoothing by the moving average filter, the fourth step is the application of the threshold to cut off background fluctuations. In Figure 6.3b, the 3σ threshold covers all fluctuations, whereas the 1σ threshold is exceeded by the background. If the background exceeds the threshold with a minimum of three connected bins, it can falsely be assumed as laser signal according to the fifth algorithm step. For a 1σ threshold, many false detections are seen for histograms with SNR < 3 in the upper left corner of Figure 6.3c, where the small SNR value indicates only a few or no laser photons at all in the histogram. As false detections caused by background can have dangerous consequences, the threshold must be thus chosen at a high level of the 3σ background uncertainty as safety precaution fulfilling common functional safety standards [80].

Below the SNR contour lines, the two pulses are recognized well for most histograms so that this multi-pulse recognition algorithm is approximately applicable for an SNR value of $k_{\mathrm{SN}} \geqslant 3$. More precisely, the limit of successfully recognized interference is given for laser-generated event rates r_{L} that are about a factor ten higher than the background-generated event rates r_{B}. There are some histograms, where three or more pulses are recognized, but the exact number of detected pulses is irrelevant there because the presence of interference has been successfully recognized for a minimum of two detected pulses. For the event rates with high SNR of the first pulse but low SNR of the second pulse, only one pulse is detected as expected by these SNR values. This detected pulse can be the ego pulse of the ego LiDAR system representing the real target distance or the aggressor pulse of the aggressor system at an arbitrary position in the histogram due to the arbitrary time offset between the measurements of both systems. Here, the interference remains unrecognized as analyzed in section 5.3. However, the high laser-generated event rates

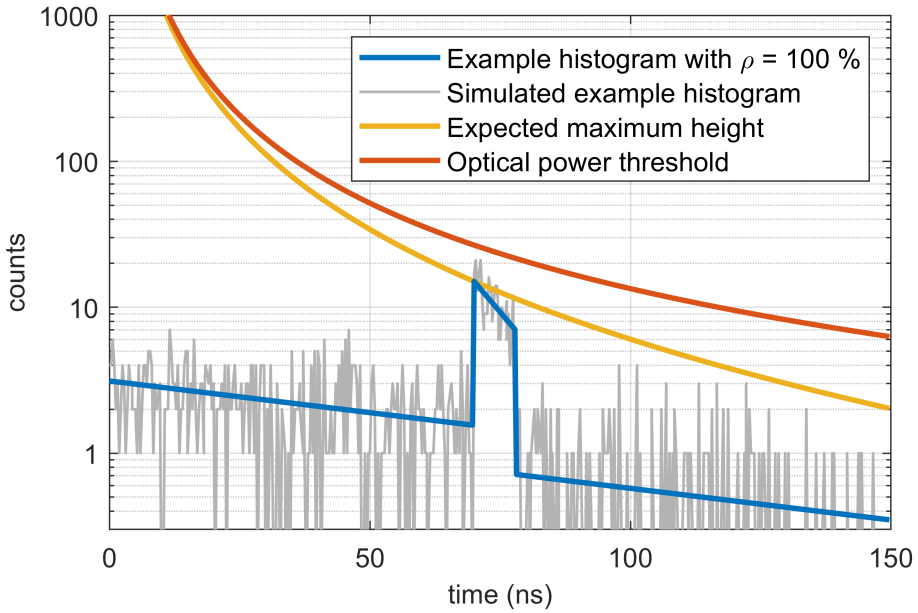

Figure 6.4: Indicator of LiDAR interference in a histogram with 1000 measurements and background level $r_B = 10\,\text{MHz}$ by an optical power threshold above the expected fluctuating pulse height of a bright Lambertian target with 100 % reflectance at the respective target distance

are an indicator that interference can potentially be present but unrecognizable. In the following, an indicator is developed and a recognition method is presented for unrecognizable interference, where only one laser pulse is detected at first.

6.3 Indicator of Interference by Optical Power Threshold

For very high laser-generated event rates, the LiDAR detector saturates quickly after the first detected pulse so that it remains unknown if there could have been a further pulse afterwards. If there are multiple arriving pulses but only one pulse is detected in the histogram, this is unrecognized interference as discussed in section 5.3. Otherwise, a bright target can lead to the same saturation effect without any interference signals. There is one indicator to distinguish unrecognized interference and an interference-free target reflection. Especially for direct interference, higher laser-generated event rates can be given than those of a target reflection, which has been shown in section 2.2. Therefore, a maximum optical power thresh-

old can be defined based on the LiDAR system parameters, which indicates the maximum realistic pulse height in the histogram produced by an interference-free target reflection. As many targets are Lambertian reflectors, the threshold is determined for the brightest possible Lambertian target with 100 % reflectance. The corresponding maximum laser-generated event rate $r_{\mathrm{L,max}}(t_{\mathrm{TOF}})$ can be calculated for each TOF t_{TOF} by (2.17). With the known background-generated event rate r_{B}, the expected maximum pulse height $h(t_{\mathrm{TOF}})$ for any TOF t_{TOF} in the histogram can be determined from the expected histogram distribution in (2.26) resulting in

$$h(t_{\mathrm{TOF}}) = n_{\mathrm{meas}} t_{\mathrm{bin}} (r_{\mathrm{B}} + r_{\mathrm{L,max}}(t_{\mathrm{TOF}})) \mathrm{e}^{-r_{\mathrm{B}} t_{\mathrm{TOF}}}, \tag{6.5}$$

where n_{meas} is the number of measurements per histogram and t_{bin} is the bin width. The fluctuations in the histogram are considered equivalently to the threshold described in the previous section by the addition of a 3σ level uncertainty considering background as well as laser photon detections. The final optical power threshold is illustrated in Figure 6.4 for a number of measurements $n_{\mathrm{meas}} = 1000$ per histogram and a background-generated event rate of $r_{\mathrm{B}} = 10\,\mathrm{MHz}$. An example histogram of LiDAR system *Owl* with the same background-generated event rate and a TOF of $t_{\mathrm{TOF}} = 70\,\mathrm{ns}$ corresponding to a target distance of about 10 m is drawn. For this histogram, the maximum laser-generated event rate results in about $r_{\mathrm{L,max}} = 90\,\mathrm{MHz}$. It should be noticed that the histogram is shown on a logarithmic scale. If a pulse signature in the histogram exceeds this optical power threshold, this is an indicator for the presence of interference so that the LiDAR system can react accordingly. As this threshold was calculated for a Lambertian target, it might be exceeded by reflections from retroreflectors or mirrors because the reflected light is not distributed in the total hemisphere as it happens for the Lambertian reflection. Many targets are Lambertian reflectors, but retroreflectors are also regularly present, for example in the form of traffic signs. For retroreflections, the optical threshold can be determined additionally, which can be used as a second optical power threshold providing an even stronger indicator of potential interference if it is exceeded. Besides the optical power, an additional indicator can be given explicitly for direct interference. As already described in section 3.2, only a few pixels of the ego LiDAR system are affected by a direct interferer so that a spatial correlation with the neighboring pixels can be useful. For small pixel FOVs, it is unlikely that only one pixel observes a very bright target. Therefore, such a condition can be an additional indicator of direct interference. When interference is indicated e.g. by a high pulse exceeding the

Lambertian threshold or even the retroreflection threshold in the histogram, time gating as described in section can be used at the next LiDAR measurement to start the measurement time after the known arrival time of the first pulse position so that later pulse arrivals can be observed. If further pulses are detected, the recognition of the LiDAR interference has been successful and the pulse heights can be determined as before. The knowledge of all pulse positions and their heights can be used to identify the ego pulse after the interference suppression.

6.4 Suppression Method

After the recognition of all potentially interfering pulses, a new LiDAR measurement with interference suppression can be conducted, which is shown in Figure 6.5. The suppression method is based on PPM, where the laser pulse emission time is modulated so that the detected TOF varies in the same way. The acquired histogram can be correlated with the known emission time pattern so that the pulse is identified at the time with the highest correlation. Alternatively, the measurement start can be modulated equally to the pulse emission time so that the pulse accumulates in the histogram as before, whereas all aggressor pulses will be distributed in the histogram following the time pattern, which is applied in this work. The pulse is modulated in steps of the pulse width so that the aggressor pulse does not accumulate in the ego histogram for two different delays. This effect can be seen as intended asynchronicity similar to the impacts of asynchronous ego and aggressor laser PRF as discussed in section 5.1.3.

The emitted pulses can only be delayed but not prematurely emitted due to the eye safety restrictions described in section 2.1.3. The delayed laser emission times reduce the frame rate of the LiDAR system. For example, applications like autonomous driving require a frame rate of 25 fps, which corresponds to the capability of human perception given by 40 ms [108]. If the laser pulse emission is shifted over the total histogram length, the maximum delay is approximately the histogram length, which is 1.28 µs for LiDAR system *Owl*. For this delay, the frame rate is reduced to 24.7 fps, which might be acceptable. For high-speed LiDAR, there are LiDAR systems with a PRF of 1 MHz and frame rates of 10 000 fps, which are ranging up to 25 m, which is equivalent to a histogram length of 170 ns [31]. In this case, the chosen maximum delay of the interference suppression would reduce the

frame rate to 86 % of the original one. Depending on the respective application, the frame rate reduction might be acceptable so that a continuous interference suppression might be applied without the need for a multi-pulse recognition. Then, the LiDAR system is not aware of present interference. Therefore, the suppression level must be chosen high enough so that even the strongest interference signal can be sufficiently suppressed, which must be determined with regards to the respectively applied distance determination algorithm.

For the proposed suppression method in this work, the available maximum number of delay steps is not required to recognize the ego pulse. Instead, a small number of delay steps is sufficient. In Figure 6.5, a simulated and a measured example histogram are shown in the left sub-figures 6.5a and 6.5c, on which the interference suppression is applied. Simulation and measurement parameters are roughly chosen in the same order to show the effects of interference suppression. The parameters are not chosen equal because this is not necessary to show the working principle and it is difficult to estimate the laser-generated event rate r_{L} from the measured histogram. The simulated histogram shows an aggressor pulse height of 17 counts and an ego pulse height of 8 counts above the expected background distribution, whereas the measured histogram has an aggressor and ego height of 20 counts and 6 counts. The aggressor signal does not have to be suppressed below the ego signal height but only strong enough to observe its reduction. The reduction of the aggressor signal height must be significantly high with regards to the possible fluctuations expected by the Poisson statistics [52]. For both histograms, the suppression level or rather the number of pulse emission time modulations is chosen to 5. Applying PPM with suppression level 5 provides the histograms in the right sub-figures 6.5b and 6.5d. Without fluctuations, the detected aggressor pulse of the simulated and measured histogram is theoretically reduced by a factor 5, which is seen in the expected histogram of Figure 6.5b. Considering the fluctuations, effective reduction factors of 4.0 and 4.1 are achieved for the aggressor pulse in the simulated and measured histogram, whereas the height of the ego pulse is approximately still the same. Due to fluctuations, the aggressor pulse height varies so that the applied nominal suppression factor is not observed but finally, the significant reduction of the aggressor pulse height is clearly visible. The distribution of the aggressor pulse to earlier times in the histogram is seen well in the simulated histogram but also in the measured histogram by the additional counts above the expected exponential

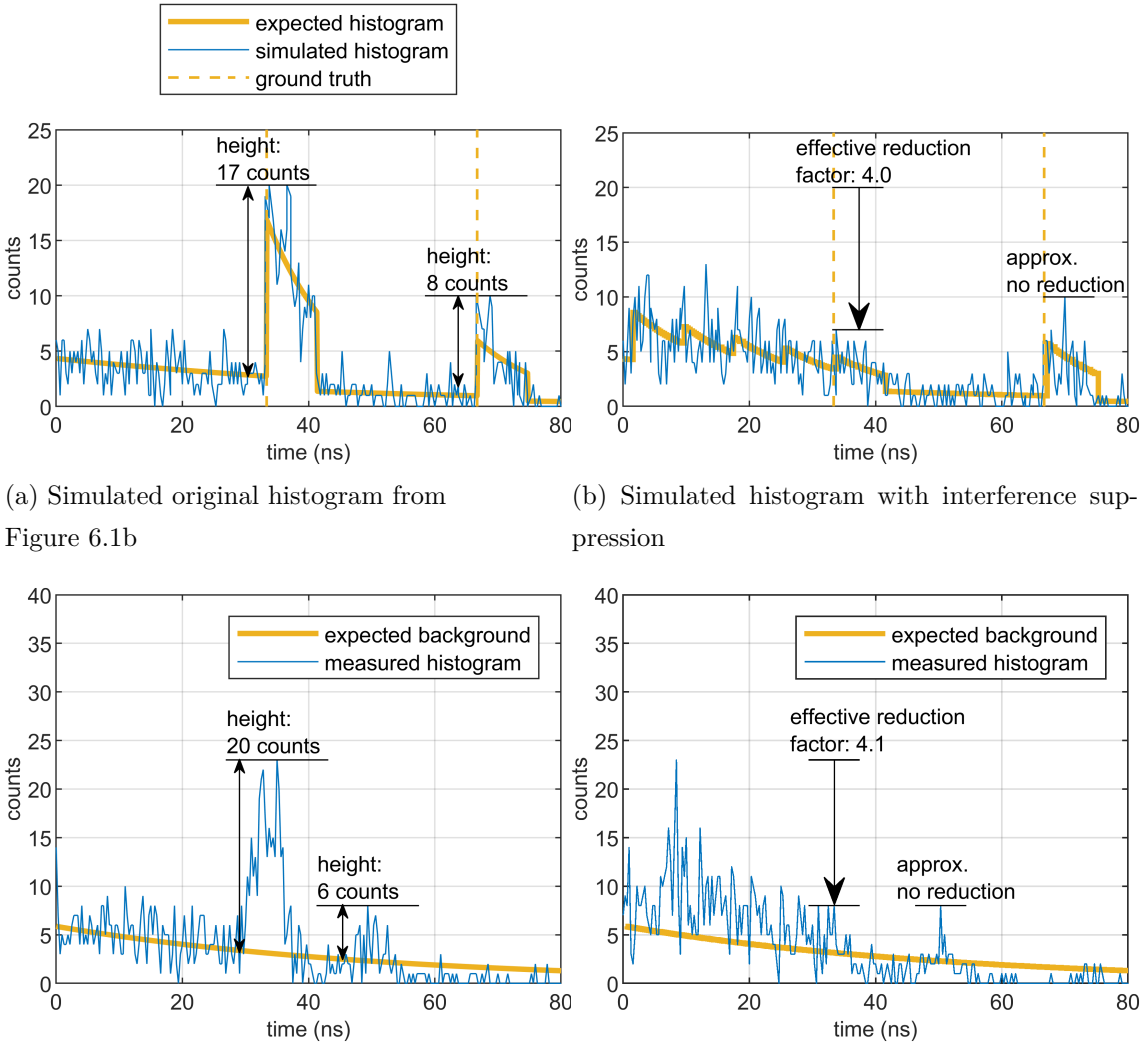

(a) Simulated original histogram from Figure 6.1b

(b) Simulated histogram with interference suppression

(c) Measured histogram with theoretically expected background distribution

(d) Measured histogram with interference suppression

Figure 6.5: Two pulses in a histogram, which are both recognized for simulation and measurement. After that, interference suppression with a nominal suppression factor of 5 is applied, which distributes the aggressor signal, whereas the ego pulse remains and can be identified.

background level. Without background light, the aggressor signal would be uniformly distributed. With background light, the aggressor signal height depends on the amount of background light arriving at the LiDAR system before the aggressor signal, which is less for an earlier arriving aggressor pulse than for a late aggressor signal. As described in section 5.3, the total number of expected background and aggressor photons before the ego pulse remains the same but the ratio between background and aggressor photons depends on the aggressor signal position in the histogram. Comparing the original histogram with the histogram after interference suppression, the pulses can be identified now as aggressor or ego pulse so that simply the ego TOF obtained by the previous multi-pulse recognition algorithm can be used to determine the target distance.

In this example, the ego system was the only LiDAR system using the suppression method, whereas the aggressor system has continued to emit regular pulses. If identical LiDAR systems from the same manufacturer apply the same suppression method, the result might look different. Decisive is whether it is possible that both systems will measure at the same time again. If PPM is used with a fixed pattern, the possibility exists that both systems use this pattern synchronously so that disturbing interference occurs again. This possibility can be easily excluded if the order of the chosen delay steps for the laser pulse emissions is randomly chosen. For example, a simple random number generator as described in appendix B can be applied, where the random numbers are directly extracted by the histogram data.

Finally, the proposed interference suppression method has successfully recognized and suppressed the interference by PPM with a minimal reduction of the frame rate. Using random numbers, the proposed method can be applied to multiple LiDAR systems. Such an interference suppression can improve the safety of LiDAR applications like autonomous driving.

Chapter 7

Conclusion and Outlook

The increased use of LiDAR systems can lead to environments with multiple systems causing interference between each other. The aim of this work was to evaluate the impacts of interference between SPAD-based dTOF LiDAR systems to provide solutions for the recognition and suppression of interference. By the example of two interfering systems denoted as ego and aggressor system, two types of LiDAR interference have been identified, which are direct and indirect interference. Direct interference affecting only one to four pixels of a LiDAR system is less problematic than indirect interference, which might influence all pixels. Independent of the interference type, six conditions for interference have been classified leading to four levels of severity: no interference, non-disturbing interference, disturbing but recognizable interference, and finally disturbing unrecognizable interference.

The first three conditions of spectral, spatial and temporal overlap determine whether interference occurs at all, regardless of whether it is disturbing or not. The first condition of spectral overlap concerning the laser wavelength and optical bandpass filter is already fulfilled for identical LiDAR systems from the same manufacturer. The second condition of spatial overlap has been analyzed using the example of two neighboring vehicles with one motorway lane distance to each other, which already illuminate the same targets beginning from a distance of 13 m for a FOV of 5°. The third condition of temporal overlap has been determined for three example applications with up to ten LiDAR systems at the same place resulting in a probability for a simultaneous measurement with any other system of 1.7 % to 49.9 %. Finally, the investigations of spatial and temporal overlap have shown that the occurrence probability of interference is non-negligible.

To analyze interference effects in LiDAR measurements for different scenarios, a test system has been developed, which can be placed in front of a LiDAR system. A demonstrator testing one LiDAR pixel has been realized, which can emulate the laser pulse reflection from the ego system under test for a virtual target width adjustable target distance in steps of 15 cm. Furthermore, an interfering laser pulse from an aggressor system and continuous background light can be produced. The demonstrator can provide discrete intensity levels of laser and background over a large range with laser-generated event rates of up to 10^{13} Hz and background-generated event rates reaching 40 MHz. The resulting measured SNR values agree with the theoretical predictions of the SNR. Therefore, the test system is suitable to test a LiDAR system by various interference scenarios.

The fourth and fifth interference condition determine whether the interference signal obtained in the measured LiDAR histogram is disturbing. For the investigated SPAD-based dTOF LiDAR, a model of the measured histograms with the signatures of multiple laser pulses has been derived. It was shown that the fourth interference condition of synchronicity is not fulfilled for small deviations of the operating frequencies of two LiDAR systems. For a deviation of 6 ppm from a nominal frequency of 10 kHz, it has been demonstrated that the observed ego signal remains accumulated in the ego histogram, whereas the aggressor signal is temporally smeared. When the deviation temporally becomes smaller than 0.08 ppm, ego and aggressor signal can both accumulate in the histogram so that the fourth interference condition is fulfilled. If enough aggressor photons are detected in the histogram, the fifth condition of a recognizable aggressor pulse is also fulfilled and the interference has been classified as disturbing.

Assuming a recognizable aggressor pulse, the sixth interference condition of a recognizable ego pulse has been investigated, which is also crucial for the general recognition of the present interference. Due to the first-photon measurement principle, two originally equal pulses are obtained with descending heights in the histogram. In the worst case, the ego pulse as second pulse in the histogram might be completely suppressed so that only the aggressor pulse might be detected and the present interference remains unrecognized. The corresponding target distance has been denoted as extinction distance. For histograms with 1000 measurements and a minimum SNR of 3, unrecognized interference already occurs for extinction distances of 13 m. Unrecognized interference can be optimally reduced if an ideal

laser-generated event rate is achieved, which approximately becomes 83 MHz for a pulse width of 8 ns. Especially in a controlled environment, the LiDAR system can be optimally designed to achieve this ideal laser-generated event rate from a target reflection. However, a moderate background-generated event rate of 10 MHz leads to an extinction distance of 46 m. For larger target distances, unrecognizable interference can still occur.

To distinguish the ego signal from the aggressor signal in the histogram, an interference suppression method for SPAD-based dTOF LiDAR systems has been presented. For the proposed suppression method, a multi-pulse recognition algorithm has been developed, which determines the positions and heights of all pulse signatures in the histogram. This algorithm has been successfully applied for histograms with an SNR value greater than or equal to 3, where the laser-generated event rate is approximately a factor ten higher than the background-generated event rate. To solve the problem of unrecognizable interference, an indicator of interference has been suggested in form of an optical power threshold, which indicates potential interference if it is exceeded. Using time-gating in the next LiDAR measurement, interference might become recognizable again. After the determination of all pulse signature positions in the histogram, a suitable suppression level has been used for PPM, where the emission times of the laser pulse are randomly modulated. Applying a nominal suppression factor of 5, an effective reduction of the aggressor pulse signature by 4.1 has been achieved, whereas the ego pulse has been remained approximately equal. Therefore, the ego pulse has be been identified and the corresponding target distance has been successfully determined.

Considering all presented conditions for LiDAR interference, the occurrence probability of interference is not negligible and the interference can disturb the distance measurement. This disturbing interference is particularly critical with regards to the strict safety standards of autonomous driving, requiring less than one failure per ten billion driving kilometers. To achieve such a LiDAR system performance, methods for the recognition and suppression of interference in the measured LiDAR histograms of SPAD-based dTOF LiDAR have been presented, which increase the reliability of LiDAR systems. Using the presented test system, the performance of LiDAR systems including their interference immunity can be tested so that the safety of applications like autonomous driving can be guaranteed.

As an outlook, the performed investigations of single LiDAR histograms can be

improved by the correlation of multiple histograms from neighboring pixels. Using all pixels, object tracking of the interfering LiDAR systems can be performed. Considering the respective application, the reliability of distance measurements might not only depend on a single LiDAR system but can be further increased by system level redundancies, which can be achieved by other LiDAR systems or a combination of different sensor types.

Appendices

In the following appendices, the PDF modeling a histogram with one laser pulse is derived and a random number generator based on the LiDAR measurements itself is described.

A PDF Derivation for Histogram with One Laser Pulse

In the following, the PDF of a histogram containing a single laser pulse is derived. This probability for the first-photon detection $P(t)$ at time t is given by the time-dependent rate $r(t)$ and under the condition that no photon has been detected before given by

$$P(t) = r(t) \cdot \left(1 - \int_0^\tau P(\tau)\mathrm{d}\tau\right). \tag{1}$$

From that, the derivative with respect to time t is determined by

$$\frac{\mathrm{d}}{\mathrm{d}t}\frac{P(t)}{r(t)} = \frac{\mathrm{d}}{\mathrm{d}t}\left(1 - \int_0^\tau P(\tau)\mathrm{d}\tau\right) \tag{2}$$

$$\Leftrightarrow \frac{\frac{\mathrm{d}P(t)}{\mathrm{d}t}r(t) - P(t)\frac{\mathrm{d}r(t)}{\mathrm{d}t}}{r^2(t)} = -P(t). \tag{3}$$

This differential equation can be cleverly integrated using the known derivative of a logarithmic function $\ln(f(t))$ with respect to t, which is given by

$$\frac{\mathrm{d}\ln(f(t))}{\mathrm{d}t} = \frac{\frac{\mathrm{d}f(t)}{\mathrm{d}t}}{f(t)}, \tag{4}$$

where the inner derivative of $f(t)$ is included. Applying this relation, the integral of the differential equation results in

$$\int_0^t \frac{\frac{\mathrm{d}P(t)}{\mathrm{d}t}}{P(t)}\mathrm{d}t = -\int_0^t r(t)\mathrm{d}t + \int_0^t \frac{\frac{\mathrm{d}r(t)}{\mathrm{d}t}}{r(t)}\mathrm{d}t \tag{5}$$

$$\ln(P(t)) - \cancel{\ln(P(0))} = -\int_0^t r(t)\mathrm{d}t + \ln(r(t)) - \cancel{\ln(r(0))}, \tag{6}$$

where two terms can be canceled due to the condition $P(0) = r(0)$ from the starting equation 1. This can be transformed into the first-photon PDF $P(t)$ for a general time-dependent rate $r(t)$ with

$$P(t) = r(t) \cdot \exp\left(-\int_0^t r(\tau)\mathrm{d}\tau\right). \tag{7}$$

For a histogram containing a single laser pulse at TOF t_{TOF} with pulse width t_{p}, the time-dependent event rate is given in (2.25) by

$$r(t) = r_{\mathrm{B}} + r_{\mathrm{L}}\left[\Theta(t - t_{\mathrm{TOF}}) - \Theta(t - (t_{\mathrm{TOF}} + t_{\mathrm{p}}))\right], \tag{8}$$

where r_{B} is the background-generated event rate and r_{L} is the laser-generated event rate of a rectangular pulse with a pulse width modeled by the Heaviside function $\Theta(t)$. To insert this rate in the PDF, the event rate $r(t)$ is integrated for the times t before, during and after the laser pulse in the histogram given by

$$\int_0^t r(\tau)\mathrm{d}\tau = r_{\mathrm{B}}\tau\Big|_0^t = r_{\mathrm{B}}t - 0 = r_{\mathrm{B}}t, \tag{9}$$

$$\int_{t_{\mathrm{TOF}}}^t r(\tau)\mathrm{d}\tau = (r_{\mathrm{B}} + r_{\mathrm{L}})\tau\Big|_{t_{\mathrm{TOF}}}^t = (r_{\mathrm{B}} + r_{\mathrm{L}})(t - t_{\mathrm{TOF}}), \tag{10}$$

$$\int_{t_{\mathrm{TOF}}+t_{\mathrm{p}}}^t r(\tau)\mathrm{d}\tau = r_{\mathrm{B}}\tau\Big|_{t_{\mathrm{TOF}}+t_{\mathrm{p}}}^t = r_{\mathrm{B}}(t - t_{\mathrm{TOF}} - t_{\mathrm{p}}). \tag{11}$$

From these time interval integrals, the PDF can be integrated from time $\tau = 0$ to an arbitrary time t, which is calculated for the second or third time period by

$$\begin{aligned} &\int_0^{t_{\mathrm{TOF}}} r(\tau)\mathrm{d}\tau + \int_{t_{\mathrm{TOF}}}^{t} r(\tau)\mathrm{d}\tau \\ &\quad = r_{\mathrm{B}} t_{\mathrm{TOF}}(r_{\mathrm{B}} + r_{\mathrm{L}})(t - t_{\mathrm{TOF}}) = r_{\mathrm{L}} t_{\mathrm{TOF}} + (r_{\mathrm{B}} + r_{\mathrm{L}})t \end{aligned} \tag{12}$$

$$\begin{aligned} &\int_0^{t_{\mathrm{TOF}}} r(\tau)\mathrm{d}\tau + \int_{t_{\mathrm{TOF}}}^{t_{\mathrm{TOF}}+t_{\mathrm{p}}} r(\tau)\mathrm{d}\tau + \int_{t_{\mathrm{TOF}}+t_{\mathrm{p}}}^{t} r(\tau)\mathrm{d}\tau \\ &\quad = r_{\mathrm{B}}\cancel{t_{\mathrm{TOF}}} + (\cancel{r_{\mathrm{B}}} + r_{\mathrm{L}})(\cancel{t_{\mathrm{TOF}}} + t_{\mathrm{p}} - \cancel{t_{\mathrm{TOF}}}) + r_{\mathrm{B}}(t - \cancel{t_{\mathrm{TOF}}} - \cancel{t_{\mathrm{p}}}) \\ &\quad = r_{\mathrm{L}} t_{\mathrm{p}} + r_{\mathrm{B}} t \end{aligned} \tag{13}$$

Using these results, the time-dependent rate $r(t)$ from 8 can be inserted in the PDF in (7) to obtain the final PDF

$$P(t) = \begin{cases} r_{\mathrm{B}} \mathrm{e}^{-r_{\mathrm{B}} t}, & 0 \leqslant t < t_{\mathrm{TOF}} \\ (r_{\mathrm{B}} + r_{\mathrm{L}}) \mathrm{e}^{r_{\mathrm{L}} t_{\mathrm{TOF}}} \mathrm{e}^{-(r_{\mathrm{B}} + r_{\mathrm{L}})t}, & t_{\mathrm{TOF}} \leqslant t < t_{\mathrm{TOF}} + t_{\mathrm{p}} \\ r_{\mathrm{B}} \mathrm{e}^{-r_{\mathrm{L}} t_{\mathrm{p}}} \mathrm{e}^{-r_{\mathrm{B}} t}, & t_{\mathrm{TOF}} + t_{\mathrm{p}} \leqslant t \end{cases}. \tag{14}$$

B Random Number Generator Based on LiDAR Measurements

For the use of the presented interference suppression method by multiple LiDAR systems, random numbers are suggested for the delay of the emitted pulses. In the following, a simple random number generator is described, which extracts the random numbers of the LiDAR measurements. The random numbers can be obtained during the accumulation of photon measurements in the TCSPC histograms. From two photon arrival times t_n and t_{n+1} for $n = 1, 3, 5, \ldots$, a random number x can be generated by

$$x = \begin{cases} 1, & t_n < t_{n+1}, \\ 0, & t_n > t_{n+1}, \\ /, & \text{else} \end{cases} \tag{15}$$

where a false detection or equal arrival times $t_n = t_{n+1}$ are rejected. A false detection is given if the background and laser light is so low that no photon at all is detected.

In contrast to that, equal arrival times are probably given if the background or laser light is so high that most background photons are detected within the first bins of the histogram or most laser photons are measured at the first bins of the expected pulse distribution in the histogram. The successfully generated random numbers provide bits with value 1 or 0. This method for random number generation has been implemented in LiDAR system *Owl*. For true random numbers, it must be guaranteed that the generated random numbers are not biased by timing issues of the LiDAR hardware, which is not proved here.

During one LiDAR measurement, enough random numbers must be generated to perform interference suppression on the next LiDAR measurement. The required number of random numbers depends on the maximum delay of the emitted pulse. Assuming the maximum delay by the histogram length of 1.28 µs, there are 160 possible delay steps for a pulse with 8 ns pulse width. This corresponds to 1 Byte of random numbers providing $2^8 - 1 = 255$ different delays, which is well feasible. For a histogram with 1000 measurements, the same number of laser pulses must be emitted so that the same number of random numbers is required. Assuming a maximum yield of 100 %, only 16 pixels of the LiDAR system are required to achieve $16 \cdot 500 = 8000$ bits = 1000 Bytes. Using the $32 \times 24 = 768$ pixels of LiDAR system *Owl*, the probability for random number generation must be only 2 %.

To determine the yield of random numbers, the probabilities for false detections or equal arrival times can be derived. The random number generation is investigated for the more common case of a normal histogram containing a single laser pulse without interfering other pulses. The probability for the false detection of one or both arrival times is based on the probability p_{non} that no photon has been detected within the histogram length t_{hist} given by

$$p_{\mathrm{non}} = 1 - \int_0^{t_{\mathrm{hist}}} P(\tau)\mathrm{d}\tau = \mathrm{e}^{-r_{\mathrm{L}} t_{\mathrm{p}}} \mathrm{e}^{-r_{\mathrm{B}} t_{\mathrm{hist}}}, \tag{16}$$

where $P(t)$ is the PDF in (2.26) and t_{p} is the laser pulse width. r_{B} or r_{L} is the background- or laser-generated event rate at the LiDAR detector. With this, the probability p_{miss} for a failed random number generation due to one or two false detections is given by

$$p_{\mathrm{miss}} = 2 \cdot p_{\mathrm{non}} - p_{\mathrm{non}}^2. \tag{17}$$

The other failure reason of equal arrival times is given by the probability p_{equal} with

$$p_{\text{equal}} = \sum_{i=1}^{n_{\text{bin}}} p_{\text{i}}^2, \tag{18}$$

where n_{bin} is the number of bins in the histogram and p_{i} is the probability for equal arrival times in the i-th bin with bin width t_{bin} given by

$$p_{\text{i}} = \int_{t}^{t+t_{\text{bin}}} P(\tau)\mathrm{d}\tau. \tag{19}$$

Otherwise, the random number generation is successful, which can be expressed by the probability p_{valid} calculated by

$$p_{\text{valid}} = p_{\text{i}} \cdot (1 - p_{\text{non}} - p_{\text{i}}). \tag{20}$$

These three probabilities determine the yield of the random number generation and therefore fulfill

$$p_{\text{miss}} + p_{\text{equal}} + p_{\text{valid}} = 1. \tag{21}$$

The derived probabilities are compared to simulation and measurement data for a target distance of 1 m, which is shown in Figure B.1. For a varied background-generated event rate from 10^5 Hz to 10^{10} Hz, the simulated and measured probabilities confirm the theoretically predicted probability distribution very well as seen in Figure B.1a. The probabilities have also been calculated for laser-generated event rates from 10^5 Hz to 10^{10} Hz, which is presented in Figure B.1b. The yellow area indicates a maximum yield of 100 % for the random number generation. For low background and laser light in the top left corner, the dark blue color represents a low random number generation because there are only a few detected photons in the histogram. If the laser-generated event rate is too low, even the pulse cannot be detected anymore. The contour line of SNR equals 3 limits the area in the top right corner, where pulse detection is probably feasible, whereas the histograms outside of this area with SNR values less than 3 are probably not evaluable. For high background at the top of the Figure, the probability for random number generation is reduced as well because the high background is measured mainly in the first bins of the histogram due to the pile-up effect. The same is given for high laser-generated event rates but a low background level, where most photons are detected within a few bins at the laser TOF. For high background- as well as high laser-generated event rates, the histogram distribution can be balanced between bins containing background or

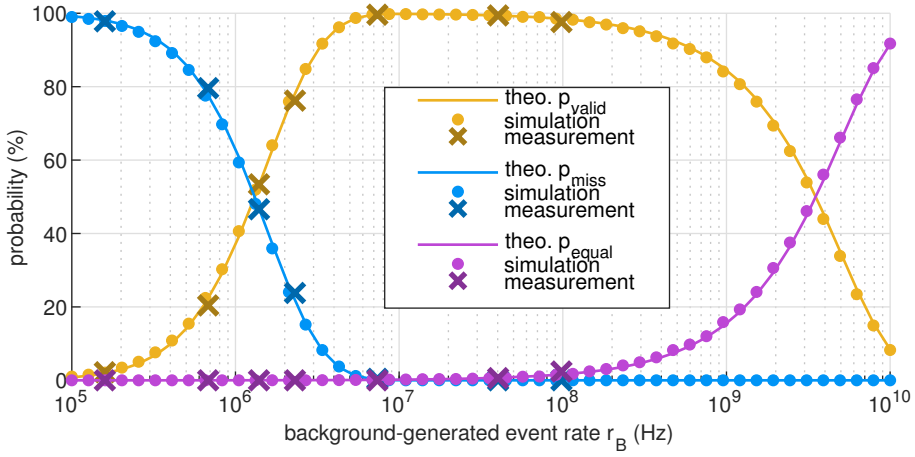

(a) Probability for successful random number generation by two valid time stamps and invalid time stamp pairs are caused by missing detections or equal time stamps.

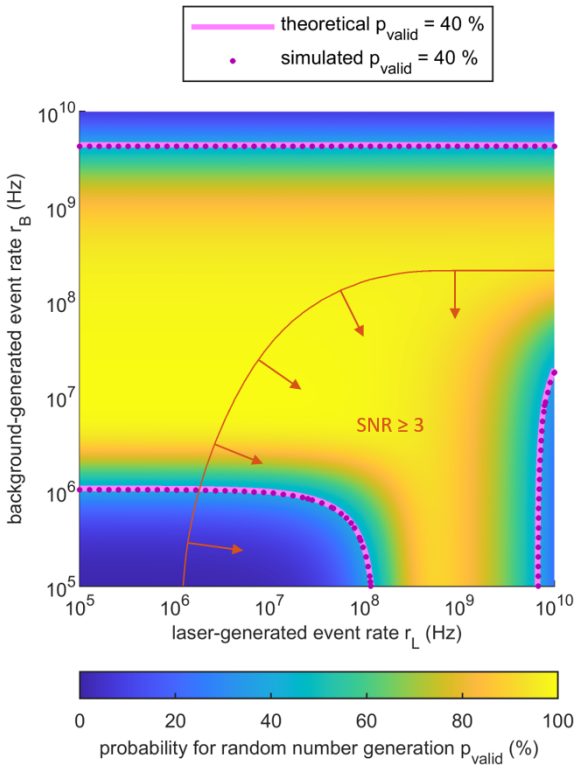

(b) Probability for all possible event rates of background (r_B) and laser (r_L). Simulation and measurement data are illustrated by the arbitrary chosen contour line of $p_\mathrm{valid} = 40\,\%$. Histograms with evaluable laser pulse position are shown for SNR $\geqslant 3$ below the orange contour line.

Figure B.1: Probability for random number generation by TCSPC histograms with one laser pulse. The theoretical derivation is confirmed by simulation and measurement data.

laser so that the probability for equal arrival times is lower than for histograms with pure background or laser. The same background- and laser-generated event rates have been simulated. An arbitrary contour line at $p_{\text{valid}} = 40\,\%$ has been chosen to compare theory and simulation. Both contour lines match very well as already seen before in Figure B.1a. For almost all of the histograms, the required probability for random number generation of $2\,\%$ required for interference suppression is achieved. Therefore, the suggested random number generation is suitable for the presented interference suppression method.

List of Figures

List of Tables

References

[1] B. Behroozpour, P. A. M. Sandborn, M. C. Wu, and B. E. Boser, "Lidar system architectures and circuits", *IEEE Communications Magazine*, vol. 55, no. 10, pp. 135–142, Oct. 2017. DOI: 10.1109/MCOM.2017.1700030.

[2] F. Villa, F. Severini, F. Madonini, and F. Zappa, "SPADs and SiPMs arrays for long-range high-speed light detection and ranging (LiDAR)", *Sensors*, vol. 21, no. 11, 3839, Jun. 2021. DOI: 10.3390/s21113839.

[3] P. Seitz and A. J. P. Theuwissen, *Single-Photon Imaging*. Berlin, Germany: Springer-Verlag Berlin Heidelberg, 2011. DOI: 10.1007/978-3-642-18443-7.

[4] M. Perenzoni, L. Pancheri, and D. Stoppa, "Compact SPAD-based pixel architectures for time-resolved image sensors", *Sensors*, vol. 16, no. 5, 745, May 2016. DOI: 10.3390/s16050745.

[5] P. B. Coates, "The correction for photon 'pile-up' in the measurement of radiative lifetimes", *Journal of Physics E: Scientific Instruments*, vol. 1, no. 8, pp. 878–879, 1968. DOI: 10.1088/0022-3735/1/8/437.

[6] A. Gupta, A. Ingle, A. Velten, and M. Gupta, "Photon-flooded single-photon 3D cameras", in *IEEE Conference on Computer Vision and Pattern Recognition*, 2019, pp. 6763–6772. DOI: 10.1109/CVPR.2019.00693.

[7] K. Pasquinelli, R. Lussana, S. Tisa, F. Villa, and F. Zappa, "Single-photon detectors modeling and selection criteria for high-background LiDAR", *IEEE Sensors Journal*, vol. 20, no. 13, pp. 7021–7032, Jul. 2020. DOI: 10.1109/JSEN.2020.2977775.

[8] T. Al Abbas, N. A. W. Dutton, O. Almer, N. Finlayson, F. M. Della Rocca, and R. Henderson, "A CMOS SPAD sensor with a multi-event folded flash time-to-digital converter for ultra-fast optical transient capture", *IEEE Sen-*

sors Journal, vol. 18, no. 8, pp. 3163–3173, Apr. 2018. DOI: 10.1109/JSEN.2018.2803087.

[9] H. Seo, H. Yoon, D. Kim, J. Kim, S.-J. Kim, J.-H. Chun, and J. Choi, "Direct TOF scanning LiDAR sensor with two-step multievent histogramming TDC and embedded interference filter", *IEEE Journal of Solid-State Circuits*, vol. 56, no. 4, pp. 1022–1035, Apr. 2021. DOI: 10.1109/JSSC.2020.3048074.

[10] J. F. Haase, A. Buchner, S. Grollius, J. Ruskowski, and H. Vogt, "Measurement concept to reduce environmental impact in direct time-of-flight LiDAR sensors", in *Quantum Sensing and Nano Electronics and Photonics XVII*, Jan. 2020, pp. 60–68. DOI: 10.1117/12.2546021.

[11] S. Bellisai, L. Ferretti, F. Villa, A. Ruggeri, S. Tisa, A. Tosi, and F. Zappa, "Low-power 20-meter 3D ranging SPAD camera based on continuous-wave indirect time-of-flight", in *Advanced Photon Counting Techniques VI*, May 2012, 83750E. DOI: 10.1117/12.920407.

[12] J. Illade-Quinteiro, V. M. Brea, P. López, D. Cabello, and G. Doménech-Asensi, "Distance measurement error in time-of-flight sensors due to shot noise", *Sensors*, vol. 15, no. 3, pp. 4624–4642, Feb. 2015. DOI: 10.3390/s150304624.

[13] S. Bellisai, D. Bronzi, F. A. Villa, S. Tisa, A. Tosi, and F. Zappa, "Single-photon pulsed-light indirect time-of-flight 3D ranging", *Optics express*, vol. 21, no. 4, pp. 5086–5098, Feb. 2013. DOI: 10.1364/OE.21.005086.

[14] S. Royo and M. Ballesta-Garcia, "An overview of lidar imaging systems for autonomous vehicles", *Applied Sciences*, vol. 9, no. 19, 4093, Sep. 2019. DOI: 10.3390/app9194093.

[15] D. Pierrottet, F. Amzajerdian, L. Petway, B. Barnes, G. Lockard, and M. Rubio, "Linear FMCW laser radar for precision range and vector velocity measurements", *MRS Proceedings*, vol. 1076, 10760406, Aug. 2008. DOI: 10.1557/PROC-1076-K04-06.

[16] A. Dieckmann and M.-C. Amann, "Frequency-modulated continuous-wave (FMCW) lidar with tunable twin-guide laser diode", in *Industrial Applications of Laser Radar*, Sep. 1994, pp. 134–142. DOI: 10.1117/12.188149.

[17] T. Kim, "Realization of integrated coherent lidar", Ph.D. dissertation, University of California, Berkeley, California, United States, 2019. [Online]. Available: https://escholarship.org/content/qt1d67v62p/qt1d67v62p_noSplash_63db99594c05eb04b901ecff982d110d.pdf (visited on 08/29/2022).

[18] R. Agishev, B. Gross, F. Moshary, A. Gilerson, and S. Ahmed, "Simple approach to predict APD/PMT lidar detector performance under sky background using dimensionless parametrization", *Optics and Lasers in Engineering*, vol. 44, no. 8, pp. 779–796, Aug. 2006. DOI: 10.1016/j.optlaseng.2005.07.010.

[19] A. Einstein, "Über einem die Erzeugung und Verwandlung des Lichtes betreffenden heuristischen Gesichtspunkt", *Annalen der Physik*, vol. 4, no. 17, pp. 132–148, Mar. 1905. [Online]. Available: http://sedici.unlp.edu.ar/handle/10915/2784.

[20] B. E. A. Saleh and M. C. Teich, *Fundamentals of Photonics*. Hoboken, New Jersey, United States: John Wiley & Sons, 2013.

[21] F. Villa, E. Conca, V. Sesta, N. Lusardi, F. Garzetti, A. Geraci, and F. Zappa, "SPADs and TDCs for photon-counting, timing and gated-imaging at 30 ps resolution and 60% efficiency", in *2018 IEEE Nuclear Science Symposium and Medical Imaging Conference (NSS/MIC)*, Nov. 2019, pp. 1–5. DOI: 10.1109/NSSMIC.2018.8824272.

[22] C. Bradley, S. Mukherjee, A. Reinhardt, P. F. McManamon, A. Lee, and V. Dhulla, "3D imaging with 128x128 eye safe InGaAs p-i-n lidar camera", in *Laser Radar Technology and Applications XXIV*, May 2019, 1100510. DOI: 10.1117/12.2521981.

[23] M. Entwistle, M. A. Itzler, J. Chen, M. Owens, K. Patel, X. Jiang, K. Slomkowski, and S. Rangwala, "Geiger-mode APD camera system for single-photon 3D LADAR imaging", in *Advanced Photon Counting Techniques VI*, May 2012, 83750D. DOI: 10.1117/12.921004.

[24] *Safety of laser products*, IEC 60825-1, International Electrotechnical Commission (IEC), 2014.

[25] A. Süss, V. Rochus, M. Rosmeulen, and X. Rottenberg, "Benchmarking time-of-flight based depth measurement techniques", in *Smart Photonic and Optoelectronic Integrated Circuits XVIII*, Mar. 2016, 975118. DOI: 10.1117/12.2212478.

[26] M. Beer, J. F. Haase, J. Ruskowski, and R. Kokozinski, "Background light rejection in SPAD-based lidar sensors by adaptive photon coincidence detection", *Sensors*, vol. 18, no. 12, 4338, Dec. 2018. DOI: 10.3390/s18124338.

[27] A. Eisele, R. Henderson, B. Schmidtke, T. Funk, L. Grant, J. Richardson, and W. Freude, "185 MHz count rate, 139 dB dynamic range single-photon avalanche diode with active quenching circuit in 130 nm CMOS technology", in *International Image Sensor Workshop (IISW)*, Jun. 2011, R43.

[28] O. Skorka and D. Joseph, "CMOS digital pixel sensors: Technology and applications", in *Nanosensors, Biosensors, and Info-Tech Sensors and Systems*, Apr. 2014, 90600G. DOI: 10.1117/12.2044808.

[29] Y. Li and J. Ibanez-Guzman, "Lidar for autonomous driving: The principles, challenges, and trends for automotive lidar and perception systems", *IEEE Signal Processing Magazine*, vol. 37, no. 4, pp. 50–61, Jul. 2020. DOI: 10.1109/MSP.2020.2973615.

[30] J. Haase, M. Beer, O. Schrey, J. Ruskowski, W. Brockherde, and H. Vogt, "Measurement concept for direct time-of-flight sensors at high ambient light", in *Quantum Sensing and Nano Electronics and Photonics XVI*, Feb. 2019, pp. 102–108. DOI: 10.1117/12.2509779.

[31] J. Nissinen and J. Kostamovaara, "A high repetition rate CMOS driver for high-energy sub-ns laser pulse generation in SPAD-based time-of-flight range finding", *IEEE Sensors Journal*, vol. 16, no. 6, pp. 1628–1633, Mar. 2016. DOI: 10.1109/JSEN.2015.2503774.

[32] C. Zhang, S. Lindner, I. M. Antolovic, J. Mata Pavia, M. Wolf, and E. Charbon, "A 30-frames/s, 252x144 SPAD flash lidar with 1728 dual-clock 48.8-ps TDCs, and pixel-wise integrated histogramming", *IEEE Journal of Solid-State Circuits*, vol. 54, no. 4, pp. 1137–1151, Apr. 2019. DOI: 10.1109/JSSC.2018.2883720.

[33] S. W. Hutchings, N. Johnston, I. Gyongy, T. Al Abbas, N. A. W. Dutton, M. Tyler, S. Chan, J. Leach, and R. K. Henderson, "A reconfigurable 3-D-stacked SPAD imager with in-pixel histogramming for flash lidar or high-speed time-of-flight imaging", *IEEE Journal of Solid-State Circuits*, vol. 54, no. 11, pp. 2947–2956, Nov. 2019. DOI: 10.1109/JSSC.2019.2939083.

[34] D. Wang, C. Watkins, and H. Xie, "MEMS mirrors for LiDAR: A review", *Micromachines*, vol. 11, no. 5, 456, Apr. 2020. DOI: 10.3390/mi11050456.

[35] G. B. Popko, T. K. Gaylord, and C. R. Valenta, "Geometric approximation model of inter-lidar interference", *Optical Engineering*, vol. 59, no. 03, 033104, Mar. 2020. DOI: 10.1117/1.OE.59.3.033104.

[36] R. D. Richmond and S. C. Cain, *Direct-Detection LADAR Systems*. Bellingham, Washington, United States: SPIE (International Society for Optical Engineering), 2010. DOI: 10.1117/3.836466.

[37] J. Haase, "Algorithmen und Signalverarbeitung für LiDAR", Ph.D. dissertation, University of Duisburg-Essen, Duisburg, Germany, Feb. 2021. [Online]. Available: https://duepublico2.uni-due.de/receive/duepublico_mods_00074921.

[38] J. F. Haase, S. Grollius, S. Grosse, A. Buchner, and M. Ligges, "A 32x24 pixel SPAD detector system for LiDAR and quantum imaging", in *Photonic Instrumentation Engineering VIII*, Mar. 2021, 116930M. DOI: 10.1117/12.2578775.

[39] *Pulsed laser diode module, LS-series*, Laser Components. [Online]. Available: https://www.lasercomponents.com/fileadmin/user_upload/home/Datasheets/lc-electronics/ls-series.pdf (visited on 08/29/2022).

[40] S. Grollius, M. Ligges, J. Ruskowski, and A. Grabmaier, "Concept of an automotive LiDAR target simulator for direct time-of-flight LiDAR", *IEEE Transactions on Intelligent Vehicles*, Nov. 2021. DOI: 10.1109/TIV.2021.3128808.

[41] R. Lange, "3D time-of-flight distance measurement with custom solid-state image sensors in CMOS/CCD-technology", Ph.D. dissertation, University of Siegen, Siegen, Germany, 2000. [Online]. Available: https://dspace.ub.uni-siegen.de/bitstream/ubsi/178/1/lange.pdf.

[42] E. F. Zalewski, "Radiometry and photometry", in *Handbook of optics*, 2010.

[43] A. Tontini, L. Gasparini, and M. Perenzoni, "Numerical model of SPAD-based direct time-of-flight flash LIDAR CMOS image sensors", *Sensors*, vol. 20, no. 18, 5203, Aug. 2020. DOI: 10.3390/s20185203.

[44] M. Iqbal, *An Introduction To Solar Radiation*. New York, United States: Elsevier (Science Publishing Co.), 1983.

[45] *Standard solar constant and zero air mass solar spectral irradiance tables*, ASTM E490-22, ASTM International, 2022. DOI: 10.1520/E0490-22.

[46] *Tables for reference solar spectral irradiances: Direct normal and hemispherical on 37 tilted surface*, ASTM G173-03, ASTM International, 2020. DOI: 10.1520/G0173-03R20.

[47] *Solar energy — reference solar spectral irradiance at the ground at different receiving conditions*, ISO 9845-1, International Organization for Standardization (ISO), 2022. [Online]. Available: https://www.iso.org/cms/%20render/live/en/sites/isoorg/contents/data/standard/07/99/79989.html (visited on 08/29/2022).

[48] C. A. Gueymard, D. Myers, and K. Emery, "Proposed reference irradiance spectra for solar energy systems testing", *Solar Energy*, vol. 73, no. 6, pp. 443–467, Dec. 2002. DOI: 10.1016/S0038-092X(03)00005-7.

[49] *Spectral luminous efficiency function for photopic vision*, Commission Internationale de l'Eclairage (CIE), 1990.

[50] A. Buchner, B. Hosticka, O. Schrey, J. F. Haase, J. Ruskowski, and A. Grabmaier, "Acquisition of multiple events in direct time-of-flight LiDAR using single-photon avalanche diodes", in *IEEE Sensors*, Oct. 2020, pp. 1–4. DOI: 10.1109/SENSORS47125.2020.9278854.

[51] M. Beer, O. M. Schrey, B. J. Hosticka, and R. Kokozinski, "Coincidence in SPAD-based time-of-flight sensors", in *13th Conference on Ph.D. Research in Microelectronics and Electronics (PRIME)*, Jun. 2017, pp. 381–384. DOI: 10.1109/PRIME.2017.7974187.

[52] S. Pellegrini, G. S. Buller, J. M. Smith, A. M. Wallace, and S. Cova, "Laser-based distance measurement using picosecond resolution time-correlated single-photon counting", *Measurement Science and Technology*, vol. 11, no. 6, pp. 712–716, Mar. 2000. DOI: 10.1088/0957-0233/11/6/314.

[53] Y. Cheng and G. Y. Wang, "Mobile robot navigation based on lidar", in *Proceedings of the 30th Chinese Control and Decision Conference (2018 CCDC)*, Jun. 2018, pp. 1243–1246. DOI: 10.1109/CCDC.2018.8407319.

[54] F. Azevedo, A. Dias, J. Almeida, A. Oliveira, A. Ferreira, T. Santos, A. Martins, and E. Silva, "LiDAR-based real-time detection and modeling of power lines for unmanned aerial vehicles", *Sensors*, vol. 19, no. 8, 1812, Apr. 2019. DOI: 10.3390/s19081812.

[55] M. Hoyhtya, J. Huusko, M. Kiviranta, K. Solberg, and J. Rokka, "Connectivity for autonomous ships: Architecture, use cases, and research challenges", in *"ICT convergence technologies leading the fourth industrial revolution"*, Dec. 2017, pp. 345–350. DOI: 10.1109/ICTC.2017.8191000.

[56] J. J. Degnan, "Present and future space applications of photon-counting lidars", in *Laser Radar Technology and Applications XIV*, May 2009, 73230E. DOI: 10.1117/12.817860.

[57] H. Hargitai, K. Willner, and M. Buchroithner, "Methods in planetary topographic mapping: A review", in *Planetary cartography and GIS*, 2019, pp. 147–174. DOI: 10.1007/978-3-319-62849-3_6.

[58] S. J. Pittman, B. Costa, and L. M. Wedding, "LiDAR applications", in *Coral reef remote sensing*, 2013, pp. 145–174. DOI: 10.1007/978-90-481-9292-2_6.

[59] D. H. Evans, R. J. Fletcher, C. Pottier, J.-B. Chevance, D. Soutif, B. S. Tan, S. Im, D. Ea, T. Tin, S. Kim, C. Cromarty, S. de Greef, K. Hanus, P. Bâty, R. Kuszinger, I. Shimoda, and G. Boornazian, "Uncovering archaeological landscapes at angkor using lidar", *Proceedings of the National Academy of Sciences of the United States of America*, vol. 110, no. 31, pp. 12 595–12 600, Jul. 2013. DOI: 10.1073/pnas.1306539110.

[60] H. Yu, X. Lu, X. Ge, and G. Cheng, "Digital terrain model extraction from airborne LiDAR data in complex mining area", in *2010 18th International Conference on Geoinformatics*, Jun. 2010, pp. 1–6. DOI: 10.1109/GEOINFORMATICS.2010.5567781.

[61] R. Tomás, A. Abellán, M. Cano, A. Riquelme, A. J. Tenza-Abril, F. Baeza-Brotons, J. M. Saval, and M. Jaboyedoff, "A multidisciplinary approach for the investigation of a rock spreading on an urban slope", *Landslides*, vol. 15, no. 2, pp. 199–217, 2017. DOI: 10.1007/s10346-017-0865-0.

[62] C. Weitkamp, *Lidar: Range-Resolved Optical Remote Sensing of the Atmosphere*. 2005, vol. 102.

[63] M. Hämmerle and B. Höfle, "Effects of reduced terrestrial LiDAR point density on high-resolution grain crop surface models in precision agriculture", *Sensors*, vol. 14, no. 12, pp. 24 212–24 230, Dec. 2014. DOI: 10.3390/s141224212.

[64] M. A. Wulder, C. W. Bater, N. C. Coops, T. Hilker, and J. C. White, "The role of LiDAR in sustainable forest management", *The Forestry Chronicle*, vol. 84, no. 6, pp. 807–826, Dec. 2008. DOI: 10.5558/tfc84807-6.

[65] W. D. Simonson, H. D. Allen, and D. A. Coomes, "Applications of airborne lidar for the assessment of animal species diversity", *Methods in Ecology and Evolution*, vol. 5, no. 8, pp. 719–729, Jun. 2014. DOI: 10.1111/2041-210X.12219.

[66] J. McCormack, J. Prine, B. Trowbridge, A. C. Rodriguez, and R. Integlia, "2D LIDAR as a distributed interaction tool for virtual and augmented reality video games", in *2015 IEEE Games Entertainment Media Conference (GEM)*, Oct. 2015, pp. 1–5. DOI: 10.1109/GEM.2015.7377221.

[67] A. Gelbart, B. C. Redman, R. S. Light, C. A. Schwartzlow, and A. J. Griffis, "Flash lidar based on multiple-slit streak tube imaging lidar", in *Laser Radar Technology and Applications VII*, Jul. 2002, pp. 9–18. DOI: 10.1117/12.476407.

[68] B. Büttgen and P. Seitz, "Robust optical time-of-flight range imaging based on smart pixel structures", *IEEE Transactions on Circuits and Systems I:*

Regular Papers, vol. 55, no. 6, pp. 1512–1525, Jul. 2008. DOI: 10.1109/TCSI.2008.916679.

[69] *Guidelines for the Design of Motorways: RAA*, Edition 2008, translation 2011, ser. FGSV R1 - Regelwerke. Cologne, Germany: FGSV-Verlag, 2008, vol. 202. [Online]. Available: https://www.fgsv-verlag.de/raa-guidelines-for-the-design-of-motorways-edition-2008-translation-2011-englische-ubersetzung (visited on 08/29/2022).

[70] *Bundeseinheitlicher Tatbestandskatalog: Straßenverkehrsordnungswidrigkeiten*, 14th ed. 2021. [Online]. Available: https://www.kba.de/DE/Themen/ZentraleRegister/FAER/BT_KAT_OWI/btkat_node.html (visited on 08/29/2022).

[71] J. R. S. Brownson, "Laws of light", in *Solar energy conversion systems*, 2014, pp. 41–66. DOI: 10.1016/B978-0-12-397021-3.00003-X.

[72] *RoboCup dutch open 2012*. [Online]. Available: https://www.flickr.com/photos/robocup2013/9015099760 (visited on 08/29/2022).

[73] *Eschersheimer Landstrasse and Alleenring in Frankfurt am Main*. [Online]. Available: https://de.wikipedia.org/wiki/Datei:Kreuzung-alleenring-eschersheimer-ffm001.jpg (visited on 08/29/2022).

[74] *The busy M1 motorway*. [Online]. Available: https://commons.wikimedia.org/wiki/File:The_busy_M1_motorway._-_geograph.org.uk_-_387438.jpg (visited on 08/29/2022).

[75] M. Yokozuka, K. Koide, S. Oishi, and A. Banno, "LiTAMIN2: Ultra light LiDAR-based SLAM using geometric approximation applied with KL-divergence", in *2021 IEEE International Conference on Robotics and Automation*, Jun. 2021, pp. 11 619–11 625. DOI: 10.1109/ICRA48506.2021.9560947.

[76] *Directives for the Design of Urban Roads: RASt 06*, Edition 2006, translation 2012. Cologne, Germany: FGSV-Verlag, 2012, vol. 200. [Online]. Available: https://www.fgsv-verlag.de/rast-e (visited on 08/29/2022).

[77] ADAC, *Autobreite in der Baustelle*, Sep. 13, 2021. [Online]. Available: https://www.adac.de/verkehr/verkehrssicherheit/unterwegs/autobreiten-in-der-baustelle/ (visited on 08/29/2022).

[78] M. ten Hompel, H. Bayhan, J. Behling, L. Benkenstein, J. Emmerich, G. Follert, M. Grzenia, C. Hammermeister, H. Hasse, D. Hoening, C. Hoppe, S. Kerner, P. Klokowski, B. Korth, G. Kuhlmann, J. Leveling, D. Lünsch, R. Mendel, F. Menebröker, A. Nettsträter, J. Pieperbeck, C. Prasse, S. Roeder, M. Roidl, M. Rotgeri, D. Sparer, S. Walter, and O. Wolf, "Technical report: Loadrunner®, a new platform approach on collaborative logistics services", Tech. Rep., 2020. DOI: 10.2195/lj_NotRev_tenhompel_en_202010_01.

[79] M. E. Warren, "Automotive LIDAR technology", in *2019 Symposium on VLSI Circuits digest of technical papers*, Jun. 2019, pp. C254–C255. DOI: 10.23919/VLSIC.2019.8777993.

[80] *Road vehicles — Functional safety*, ISO 26262, International Organization for Standardization (ISO), 2018.

[81] J. K. Doylend and S. Gupta, "An overview of silicon photonics for LIDAR", in *Silicon Photonics XV*, Feb. 2020, 112850J. DOI: 10.1117/12.2544962.

[82] N. Kalra and S. Paddock, *Driving to safety: How many miles of driving would it take to demonstrate autonomous vehicle reliability?*, 2016. DOI: 10.7249/RR1478.

[83] Frost & Sullivan, *Autonomous car and electric vehicle growth opportunities in the test and measurement market, forecast to 2025*, 2020.

[84] Yole Développement, *LiDAR for automotive and industrial applications 2020*, 2020.

[85] dSPACE. "AURELION lidar model", [Online]. Available: https://www.dspace.com/en/ltd/home/products/sw/experimentandvisualization/aurelion_sensor-realistic_sim/aurelion_lidar.cfm (visited on 08/29/2022).

[86] IPG Automotive GmbH. "CarMaker". (2021), [Online]. Available: https://ipg-automotive.com/de/produkte-services/simulation-software/carmaker/ (visited on 08/29/2022).

[87] DIOPTIC GmbH. "LIDAR - light detection and ranging", [Online]. Available: https://www.dioptic.de/lidar/ (visited on 08/29/2022).

[88] Labsphere. "Permaflect targets: Rigid, lidar, commercial", [Online]. Available: https://www.labsphere.com/labsphere-products-solutions/materials-coatings-2/targets-standards/permaflect-ii-targets/ (visited on 08/29/2022).

[89] "Aldenhoven testing center", [Online]. Available: https://www.aldenhoven-testing-center.de/de/ (visited on 08/29/2022).

[90] I. Stroh. "Drei Sensortechnologien: Lidar und die Levels". (2020), [Online]. Available: https://www.elektroniknet.de/automotive/assistenzsysteme/lidar-und-die-levels.172737.html (visited on 08/29/2022).

[91] Pixabay. [Online]. Available: https://pixabay.com/.

[92] Freepik. [Online]. Available: https://www.freepik.com.

[93] R. H. Rasshofer, M. Spies, and H. Spies, "Testsystem für Lidarsensoren", DE102007057372. [Online]. Available: https://patents.google.com/patent/DE102007057372A1 (visited on 08/29/2022).

[94] J. Werschnik, T. Preuti, and H. Häseler, "Testeinheit und Verfahren zum Prüfen einer LIDAR-Einheit für ein Fahrzeug", DE102019106129. [Online]. Available: https://www.freepatentsonline.com/DE102019106129.html (visited on 08/29/2022).

[95] DIOPTIC. "Reichweitenprüfung von Lidarsensoren", [Online]. Available: https://www.dioptic.de/2020/03/06/pruefung-von-lidarsensoren-augensicherheit-und-reichweite/ (visited on 08/29/2022).

[96] ADAS iiT. "LiDAR target simulator". (2020), [Online]. Available: https://www.adas-iit.com/sensor-simulation/sensor-fusion-test/lidar-target-simulator/ (visited on 08/29/2022).

[97] "HORIBA develops world's first LIDAR test system". (2020), [Online]. Available: https://www.horiba.com/deu/company/news/detail/news/8/2020/horiba-develops-worlds-first-lidar-test-system/ (visited on 08/29/2022).

[98] J. L. Smith, "Concepts using optical MEMS array for ladar scene projection", in *Technologies for Synthetic Environments: Hardware-in-the-Loop Testing VIII*, Sep. 2003, pp. 276–287. DOI: 10.1117/12.499175.

[99] Y. Gao, L. Zhou, X. Wang, H. Yan, K. Hao, S. Yang, and Z. Li, "A programmable all-optical delay array for light detection and ranging scene generation", *IEEE Access*, vol. 7, pp. 93 489–93 500, Jul. 2019. DOI: 10.1109/ACCESS.2019.2928018.

[100] Technische Universität Ilmenau, *Ausgewählte Forschungs- und Förderprojekte der TU Ilmenau*, 2021. [Online]. Available: https://www.tu-ilmenau.de/forschung/forschungsaktivitaeten/forschungsprojekte (visited on 08/29/2022).

[101] T. Dallmann, J.-K. Mende, and S. Wald, "ATRIUM: A radar target simulator for complex traffic scenarios", in *2018 IEEE MTT-S International Conference on Microwaves for Intelligent Mobility (ICMIM)*, Apr. 2018, pp. 1–4. DOI: 10.1109/ICMIM.2018.8443515.

[102] M. Engelhardt, F. Pfeiffer, and E. M. Biebl, "A high bandwidth radar target simulator for automotive radar sensors", in *Proc. of the 13th European Radar Conference*, Oct. 2016, pp. 245–248. [Online]. Available: https://ieeexplore.ieee.org/document/7811693 (visited on 08/29/2022).

[103] M. Beer, "SPAD-basierte Sensoren für die laufzeitbasierte Distanzmessung bei hoher Hintergrundlichtintensität", Ph.D. dissertation, University of Duisburg-Essen, Duisburg, Germany, Nov. 2018. [Online]. Available: https://duepublico2.uni-due.de/servlets/MCRFileNodeServlet/duepublico_derivate_00046797/Diss_Beer.pdf.

[104] P. Padmanabhan, C. Zhang, and E. Charbon, "Modeling and analysis of a direct time-of-flight sensor architecture for LiDAR applications", *Sensors*, vol. 19, no. 24, 5464, Dec. 2019. DOI: 10.3390/s19245464.

[105] F. Träger, *Springer handbook of lasers and optics*. Berlin, Germany: Springer-Verlag Berlin Heidelberg, 2012.

[106] "Acktar blackened laser beam traps and blocks", [Online]. Available: https://www.edmundoptics.com/f/acktar-blackened-laser-beam-traps-and-blocks/39581 (visited on 08/29/2022).

[107] *ND filters: Mounted, AR coated for 650 - 1050 nm*. [Online]. Available: https://www.thorlabs.com/newgrouppage9.cfm?objectgroup_id=6274 (visited on 08/29/2022).

[108] I. Maksymova, C. Steger, and N. Druml, "Review of LiDAR sensor data acquisition and compression for automotive applications", in *Proceedings*, vol. 2, Dec. 2018, pp. 852–855. DOI: 10.3390/proceedings2130852.

[109] A. Egidi, "Review of main optical retroreflectors", Istituto Nazionale di Ricerca Metrologica, Tech. Rep. RT 31/2018, 2018. DOI: 10.13140/RG.2.2.12150.04166.

[110] *Ultra high speed photoreceiver with Si-PIN photodiode*, FEMTO. [Online]. Available: https://www.femto.de/images/pdf-dokumente/de-hsa-x-s-1g4-si.pdf (visited on 08/29/2022).

[111] *QL90O7SA/B/C*, Laser Components. [Online]. Available: https://www.lasercomponents.com/fileadmin/user_upload/home/Datasheets/diverse-laser-diodes/qsi/ql90o7s-a_b_c.pdf (visited on 08/29/2022).

[112] *Drive electronics for CW laser diodes*, Laser Components. [Online]. Available: https://www.lasercomponents.com/de-en/product/drive-electronics-for-cw-laser-diodes/ (visited on 08/29/2022).

[113] *50 MHz pulse generator, Model 8500*, Kontron. [Online]. Available: https://www.taborelec.com/GenericHendler/GetFile.ashx?D=0&DG=3797 (visited on 08/29/2022).

[114] A. K. Pediredla, A. C. Sankaranarayanan, M. Buttafava, A. Tosi, and A. Veeraraghavan, "Signal processing based pile-up compensation for gated single-photon avalanche diodes", *arXiv preprint*, Jun. 2018, arXiv:1806.07437.

[115] *Oscillators*, Mouser Europe. [Online]. Available: https://eu.mouser.com/c/passive-components/frequency-control-timing-devices/oscillators/ (visited on 08/29/2022).

[116] *MEMS clock oscillator*, Mouser. [Online]. Available: https://www.mouser.de/datasheet/2/3/ASEM-44258.pdf (visited on 08/29/2022).

[117] *Mars ZX3 SoC module*, enclustra. [Online]. Available: https://www.enclustra.com/assets/scripts/downloadmanuald.php?f=Mars_ZX3_User_Manual.pdf (visited on 08/29/2022).

[118] S. Grollius, A. Buchner, M. Ligges, and A. Grabmaier, "Probability of unrecognized LiDAR interference for TCSPC LiDAR", *IEEE Sensors Journal*, vol. 22, no. 13, pp. 12 976–12 986, Jun. 2022. DOI: 10.1109/JSEN.2022.3178179.

[119] C. Grönwall, O. Steinvall, F. Gustafsson, and T. Chevalier, "Influence of laser radar sensor parameters on range-measurement and shape-fitting uncertainties", *Optical Engineering*, vol. 46, no. 10, 106201, Oct. 2007. DOI: 10.1117/1.2789654.

[120] M. Perenzoni, D. Perenzoni, and D. Stoppa, "A 64 x 64-pixels digital silicon photomultiplier direct TOF sensor with 100-MPhotons/s/pixel background rejection and imaging/altimeter mode with 0.14% precision up to 6 km for spacecraft navigation and landing", *IEEE Journal of Solid-State Circuits*, vol. 52, no. 1, pp. 151–160, Jan. 2017. DOI: 10.1109/JSSC.2016.2623635.

[121] A. Buchner, S. Hadrath, R. Burkard, F. M. Kolb, J. Ruskowski, M. Ligges, and A. Grabmaier, "Analytical evaluation of signal-to-noise ratios for avalanche- and single-photon avalanche diodes", *Sensors*, vol. 21, no. 8, 2887, Apr. 2021. DOI: 10.3390/s21082887.

[122] I.-P. Hwang and C.-H. Lee, "Mutual interferences of a true-random LiDAR with other LiDAR signals", *IEEE Access*, vol. 8, pp. 124 123–124 133, Jun. 2020. DOI: 10.1109/ACCESS.2020.3004891.

[123] B. Büttgen, M.-A. El Mechat, F. Lustenberger, and P. Seitz, "Pseudonoise optical modulation for real-time 3-D imaging with minimum interference", *IEEE Transactions on Circuits and Systems I: Regular Papers*, vol. 54, no. 10, pp. 2109–2119, Oct. 2007. DOI: 10.1109/TCSI.2007.904598.

[124] T. Fersch, R. Weigel, and A. Koelpin, "A CDMA modulation technique for automotive time-of-flight LiDAR systems", *IEEE Sensors Journal*, vol. 17, no. 11, pp. 3507–3516, Jun. 2017. DOI: 10.1109/JSEN.2017.2688126.

[125] D. U. Fluckiger, B. F. Boland, and E. Marcus, "Optimal pseudorandom pulse position modulation ladar waveforms", *Applied Optics*, vol. 54, no. 9, pp. 2183–2186, Mar. 2015. DOI: 10.1364/AO.54.002183.

[126] G. Kim and Y. Park, "Suitable combination of direct intensity modulation and spreading sequence for LIDAR with pulse coding", *Sensors*, vol. 18, no. 12, 4201, Nov. 2018. DOI: 10.3390/s18124201.

[127] L. Carrara and A. Fiergolski, "An optical interference suppression scheme for TCSPC flash LiDAR imagers", *Applied Sciences*, vol. 9, no. 11, 2206, May 2019. DOI: 10.3390/app9112206.

[128] A. R. Ximenes, P. Padmanabhan, M.-J. Lee, Y. Yamashita, D.-N. Yaung, and E. Charbon, "A modular, direct time-of-flight depth sensor in 45/65-nm 3-D-stacked CMOS technology", *IEEE Journal of Solid-State Circuits*, vol. 54, no. 11, pp. 3203–3214, Nov. 2019. DOI: 10.1109/JSSC.2019.2938412.

[129] P. Du, F. Zhang, Z. Li, Q. Liu, M. Gong, and X. Fu, "Single-photon detection approach for autonomous vehicles sensing", *IEEE Transactions on Vehicular Technology*, vol. 69, no. 6, pp. 6067–6078, Jun. 2020. DOI: 10.1109/TVT.2020.2984772.

[130] T.-H. Sang, N.-K. Yang, Y.-C. Liu, and C.-M. Tsai, "A method for fast acquisition of photon counts for SPAD LiDAR", *IEEE Sensors Letters*, vol. 5, no. 3, pp. 1–4, Mar. 2021. DOI: 10.1109/LSENS.2021.3056449.

[131] Y. Yu, Z. Wang, K. Ma, C. Chen, X. Wang, B. Xue, X. Li, F. Zhang, X. Pan, Q. Zhuang, and H. Li, "Detection probability analysis of true random coding photon counting lidar", *Photonics*, vol. 8, no. 12, 545, Nov. 2021. DOI: 10.3390/photonics8120545.

DOI: 10.17185/duepublico/78749
URN: urn:nbn:de:hbz:465-20230803-140039-1